Ice-proximal sea-ice reconstruction in Powell Basin, Antarctica since the Last Interglacial

Wee Wei Khoo[1*], Juliane Müller[1,2,3], Oliver Esper[1], Wenshen Xiao[4], Christian Stepanek[1], Paul Gierz[1], Gerrit Lohmann[1,3,5], Walter Geibert[1], Jens Hefter[1] and Gesine Mollenhauer[1,2,3]

[1]Alfred Wegener Institute, Helmholtz Centre for Polar and Marine Research, Bremerhaven, Germany
[2]Department of Geoscience, University of Bremen, Bremen, Germany
[3]MARUM - Center for Marine Environmental Sciences, University of Bremen, Bremen, Germany
[4]State Key Laboratory of Marine Geology, Tongji University, Shanghai, China
[5]Department of Environmental Physics, University of Bremen, Bremen, Germany

Correspondence: Wee Wei Khoo (wee.wei.khoo@awi.de)

ABSTRACT. In Antarctica, the presence of sea ice not only plays a critical role in the climate system but also contributes to enhancing the stability of the floating ~~in front of~~ ice shelves~~.~~ ~~promotes their stability and prevents the risk of catastrophic collapse as witnessed in recent events along the Antarctic Peninsula.~~ Hence, ~~I~~investigating past ice-proximal sea-ice conditions, especially across glacial-interglacial cycles, can provide crucial information pertaining to sea-ice variability and deepen our understanding of ocean-ice-atmosphere dynamics and feedback~~s~~. In this study, we apply a multiproxy approach, in combination with numerical climate modeling, to explore glacial-interglacial environmental variability. We analyz~~e~~~~ing~~ the novel sea ice biomarker $IPSO_{25}$ (a di-unsaturated highly branched isoprenoid (HBI)), open-water biomarkers (tri-unsaturated HBIs; z-/e-trienes), and the diatom assemblage and primary productivity indicators in a marine sediment core retrieved from Powell Basin, NW Weddell Sea. These biomarkers have been established as reliable proxies for reconstructing near-coastal sea-ice conditions in the Southern Ocean, where the typical use of sea ice-related diatoms can be impacted by silica dissolution. We present the first continuous sea-ice records, in close proximity to the Antarctic continental margin, since the penultimate deglaciation. Our data shed new light on the (seasonal) variability of sea ice in the basin~~since the penultimate deglaciation, ca. 145 ka before present~~, and reveal a highly dynamic glacial-interglacial sea-ice setting characterized by significant shifts from perennial ice cover to seasonal sea-ice cover and open marine environment over the last 145 kyrs. Our results also unveil a stronger deglacial amplitude and warming during the Last Interglacial (MIS 5e) compared to the current one (Holocene). A short-term sea ice readvancement also occurred towards the end of each deglaciation. Finally, despite similar findings between the proxy and model data, notable differences persist between both interglacials – emphasizing the necessity for different Antarctic ice-sheet configurations to be employed and more robust paleoclimate data to enhance climate model performance close to the Antarctic continental margin.

1 Introduction

Sea ice plays a vital role within Earth's climate system, exerting significant influence on air-sea interactions, ocean circulation and ecosystem dynamics. Its presence alters the surface albedo of the ocean through the reflectance of incoming solar radiation, thereby minimizing ocean warming (Ebert et al., 1995). Likewise, sea ice affects the atmosphere-ocean interaction by inhibiting the exchange of heat, gas and water vapor between both media (Dieckmann and Hellmer, 2010). During sea-ice formation, brine rejection occurs and leads to the production of high-saline shelf water. This dense high-saline shelf water then sinks towards the deeper ocean. Consequently, this process results in redistribution of salinity within the water column and has a profound impact on the stratification and ventilation of the ocean (Vaughan et al., 2013). For example, in a few locations in the Southern Ocean (SO), such as the Weddell Sea, the high-saline shelf water – depending on its route and mixing process – becomes the precursor of Antarctic Bottom Water (AABW), which is a major driver of the global thermohaline circulation and an important water mass that ventilates the deep ocean basins (Naveira Garabato et al., 2002; Rintoul, 2018; Seabrooke et al., 1971). Furthermore, when sea ice melts, the freshened surface water mixes with the upwelled deep water, contributing to the mode and intermediate waters in the Atlantic, Indian and Pacific sectors of the SO (Abernathey et al., 2016; Pellichero et al., 2018). ~~Additionally, the presence of s~~Sea ice also serves as a crucial buttressing force at the ice front, effectively preventing or delaying the occurrence of potential calving events (Robel, 2017). This phenomenon was evident at locations such as the Mertz Glacier Tongue (Massom et al., 2015) and the Totten Ice Shelf (Greene et al., 2018) in East Antarctica. Furthermore, the presence of a sea-ice buffer in front of the ice terminus acts to diminish~~attenuates~~ ocean swells as they propagate~~travel~~ towards land. For instance, Massom et al. (2018) observed a substantial increase (orders of magnitude) in wave energy experienced at the fronts of the Larsen ice shelves and the Wilkins Ice Shelf when the sea-ice buffer was removed~~the ice shelves, thus enhancing the stability of said ice shelves and impeding calving events (Greene et al., 2018; Massom et al., 2018; Robel, 2017)~~. In this regard, any changes to the sea-ice cover can potentially alter ice-ocean-atmosphere dynamics and ocean circulation patterns, making~~.~~ ~~A~~ analyses of sea-ice variability over glacial-interglacial cycles, covering periods of less and more pronounced sea-ice cover, crucial ~~can also provide valuable information pertaining to identifying potential tipping points in the ice-ocean-atmosphere system~~.

Presently, numerous methods are used to reconstruct past sea-ice conditions, including biogenic proxies (e.g., biomarkers, diatoms, dinoflagellate cysts, foraminifera and ostracods) and sedimentological proxies (e.g., ice-rafted debris) in marine sediments, as well as chemical compounds archived in ice cores ~~geochemical and sedimentary records such as sea-salt (ssNa+) traces in ice cores and ice-rafted debris in marine sediments~~ (e.g., methanesulfonic acid and sea-salt (ssNa+); de Vernal et al., 2013 and references therein). Determination of methanesulfonic acid or ssNa+ concentrations in Antarctic ice cores permits well-dated and temporally high-resolution regional sea-ice reconstructions but is often affected by other sea ice independent factors such as atmospheric transport (Abram et al., 2013). In particular, direct proxies, originating from sea-ice dwelling microorganisms, which are preserved in marine sediments are often preferred as they increase the reliability of sea-ice estimation (Leventer, 1998). Despite this, our understanding of past sea ice changes in the SO remains limited.

The Cycles of Sea-Ice Dynamics in the Earth System working group (C-SIDE; Chadwick et al., 2019; Rhodes et al., 2019) consolidated a list of published Antarctic marine sea-ice records, as outlined in the review paper by Crosta et al. (2022). The compilation documents 20 studies on sea-ice variability during the Holocene (0-12 ka before present (BP)), 150 records detailing changes at the Last Glacial Maximum (LGM; ca. 21 ka BP or Marine Isotope Stage (MIS) 2), and a mere 14 sea-ice records dating back to around 130 ka BP. Notably, just two records extend beyond MIS 6 (ca. 191 ka BP; see also Fig. 3 in Crosta et al., 2022). Their work underscores the pronounced dearth~~Further highlighted is the lack~~ of (paleo) sea-ice reconstructions, particularly in regions south of 60°S, notably in the Atlantic sector, and~~especially~~ during the Last Interglacial (LIG) and beyond. ~~For additional information, please refer to Crosta et al. (2022).~~ This scarcity of records, in particular proximal to the continental margin, is attributable to difficulties in recovering marine sediment cores in the polar regions that at present are still subject to heavy year-round ice cover, and a lack of continuous sedimentary records due to erosion and disturbance at the sea floor during past glaciations. Moreover, limited preservation potential of silica frustules in SO regions outside of the opal belt~~, in particular proximal to the continental margin,~~ further hampers sea-ice reconstructions using diatom assemblages (Ryves et al., 2009; Vernet et al., 2019). As such, important feedback mechanisms related to the sea ice-ice shelf system~~, that are particularly well observed~~ during warmer-than-present periods and throughout climate transitions, remain poorly understood. Ultimately, this lack of knowledge —on how Antarctic ice sheets/shelves respond(ed) to oceanic forcing —may disadvantage ~~our understanding of~~ climate models' ability to faithfully reproduce dynamics in the ocean-sea ice-ice system, and limit our confidence in future projections of the Antarctic Ice Sheet's contribution towards global sea level rise (Deconto and Pollard, 2016; Naughten et al., 2018). ~~For instance, Holloway et al. (2016; 2017) investigated simulated Antarctic winter sea ice (WSI) distribution that best agrees with the peak $\delta^{18}O$ value recorded in multiple East Antarctic ice cores at 128 ka BP. They determined that to match the peak isotopic value, a significant reduction in WSI, equivalent to approximately half the size of pre-industrial sea-ice cover, would have occurred at 128 ka BP in the SO. Furthermore, calculations from their study also revealed differences in WSI retreat across the SO sectors. The Atlantic sector experienced the most substantial decline, relative to pre-industrial, with a reduction of 67% sea-ice extent, while the Indian and Pacific sectors decreased by 59% and 43%, respectively.~~ Despite similar LIG-WSI retreats in marine records, inconsistency with regard to the position of the sea-ice edge, in particular in the Atlantic sector, remains evident when the proposed spatial structure of the $\delta^{18}O$-agreed WSI extent is compared to published marine records (Holloway et al., 2017). Holloway et al. (2017) and Crosta et al. (2022) opined that this discrepancy may result from the marine records (Bianchi and Gersonde, 2002; Chadwick et al., 2020; 2022) being located too far north to adequately validate the $\delta^{18}O$-agreed WSI extent. Thus, they emphasized the need for additional marine records closer to the continental margin to adequately constrain the spatial pattern of the LIG sea-ice extent.

In recent years, the use of a novel sea-~~-~~ice biomarker has been found increasingly applicable as a suitable proxy for Antarctic sea-ice reconstructions (Belt et al., 2016; Smik et al., 2016). This sea-~~-~~ice biomarker, a di-unsaturated C_{25} highly branched isoprenoid (HBI) alkene, introduced as an Antarctic sea-ice proxy by Massé et al. (2011), was later termed ~~-~~Ice Proxy for the Southern Ocean with 25 carbon

atoms ($IPSO_{25}$), drawing parallel to the Arctic IP_{25} (Belt et al., 2016). $IPSO_{25}$ is a lipid molecule produced by the sympagic diatom *Berkeleya adeliensis*, which lives in the sea-ice matrix and is generally abundant during late spring and early summer (Belt et al., 2016; Riaux-Gobin and Poulin, 2004), hence, making the biomarker a good indicator for spring/summer sea ice. Furthermore, the biomarker is well-preserved in the sediment and widely identified in areas near to the Antarctic continent (for more details, see Belt, 2018; Belt et al., 2016). Nevertheless, there remains a risk of under-/overestimating the presence of sea ice when relying solely on the $IPSO_{25}$ proxy. Thus, Vorrath et al. (2019) proposed combining open-water phytoplankton markers like dinosterol or a HBI-triene with the $IPSO_{25}$ proxy, to calculate the phytoplankton-$IPSO_{25}$ index ($PIPSO_{25}$). This enhances the quantitative application of the $IPSO_{25}$ proxy. For example, in cases where the $IPSO_{25}$ concentration is minimal or absent, this may imply either an open ocean condition (substantiated by a high phytoplankton signal) or the presence of a perennial ice cover (evident by a low/absent phytoplankton signal). As such, the use of the $PIPSO_{25}$ proxy~~,~~ proves to be a more reliable approach to distinguish contrasting sea-ice settings (Belt and Müller, 2013; Lamping et al., 2020). To substantiate this application, Lamping et al. (2021) compared $PIPSO_{25}$-derived sea-ice estimates close to the Antarctic continental margin against satellite sea-ice observations and modeled sea-ice patterns, revealing strong correlation between the proxy, ~~observation~~satellite and modeled data. Until now, the majority of HBI-based sea-ice reconstructions has focused on Holocene and deglacial/LGM time scales (e.g., Barbara et al., 2013; 2016; Denis et al., 2010; Etourneau et al., 2013; Lamping et al., 2020; Sadatzki et al., 2023; Vorrath et al., 2020, 2023) and one reconstruction dates back to the last ca. 60 ka BP (Collins et al., 2013). Yet, this tool has not been applied towards studying sea-ice variability in the Antarctic during warm climates beyond the current interglacial.

Here, we aim~~fill this gap by pursuing a multiproxy approach~~ to investigate the glacial-interglacial environmental variability in the Powell Basin, NW Weddell Sea through a multiproxy approach, and provide the first continuous ice-proximal Antarctic sea-ice record covering the last ca. 145 kyrs. We present biomarker-based reconstructions of sea ice, subsurface ocean temperature, total organic carbon (TOC) and biogenic silica ($bSiO_2$) content, as well as diatom-based sea-ice concentration and summer sea surface temperature (SSST). This information is complemented by reconstructions of sea ice, primary productivity and SSST records from a neighboring core in the South Scotia Sea as well as numerically~~-~~ modeled sea ice, sea surface and subsurface temperatures to track latitudinal shifts in the environmental development in the Atlantic sector of the SO.

2 Study area

The Powell Basin (Fig. 1a) is a semi-isolated basin situated in the northwestern part of the Weddell Sea. It has an area of approximately $5x10^4$ km^2 and an average water depth of 3,300 km (Coren et al., 1997; Viseras and Maldonado, 1999). The basin, enclosed by the Antarctic Peninsula to the west, the South Scotia Sea to the north, the South Orkney Microcontinent to the east, and the ~~Jane Basin and the~~ Weddell Sea to the South, is at present subject to the clockwise-circulating regime of the Weddell Gyre~~ (Fig. 1)~~. As described in Orsi et al. (1993) and Vernet et al. (2019), the gyre involves four main

water masses, namely Antarctic Surface Water, Warm Deep Water (WDW), Weddell Sea Deep Water (WSDW) and Weddell Sea Bottom Water (WSBW; Fig. 1b). The Antarctic Surface Water generally consists of shelf waters formed over the continental shelfves, such as winter water, high salinity shelf water from brine rejection due to sea-ice formation, and ice-shelf water from glacial melt. The shelf waters travel along the Weddell Sea continental shelf via the Antarctic Coastal Current while denser shelf water cascades down and along the continental slope as the Antarctic Slope Current (Deacon, 1937; Fahrbach et al., 1992; Jacobs, 1991; Thompson et al., 2018). The WDW originates from the warm, saline and low-oxygen Antarctic Circumpolar Current that is advected and subsequently integrated into the gyre's circulation at its eastern front (Orsi et al., 1993; 1995). Along the southern boundary of the Weddell Gyre, the WDW upwells close to the Antarctic margin and mixes with the Antarctic Surface Water. The admixture cools and becomes denser, giving rise to the formation of WSDW and WSBW water masses at deeper water depths (Carmack and Foster, 1975; Dorschel, 2019; Huhn et al., 2008). In the Powell Basin, part of the WSDW flows out into the Scotia Sea through channels on the western slope of the basin (namely Philip, Bruce and Discovery Passages; Morozov et al., 2020). The remaining WSDW and a part of WSBW navigate around the southern and eastern South Orkney Plateau, progressing northward via the Orkney Passage as AABW, while the residual WSBW recirculates within the Weddell Gyre (Fedotova and Stepanova, 2021; Gordon et al., 2001; Orsi et al., 1999).

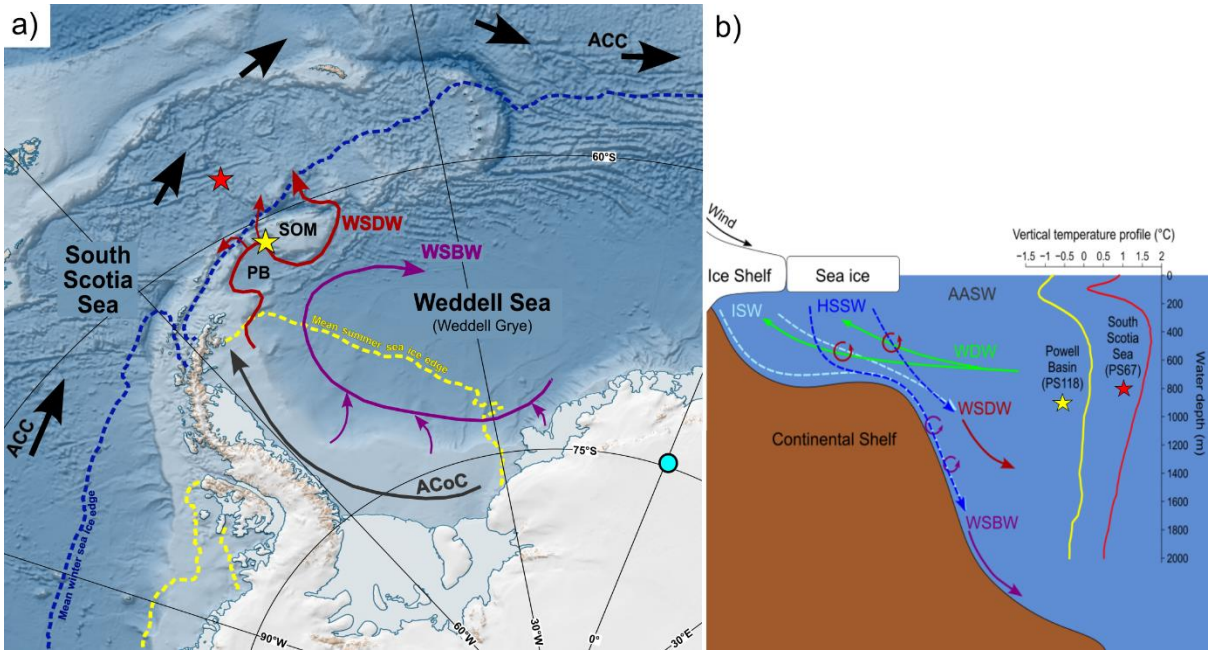

Figure 1. a) Map of the study area showing the locations of marine sediment cores PS118_63-1 (yellow star), PS67/219-1 (red star) and EDML ice core (light blue circle) discussed in this paper. Mean winter and summer sea-ice extent (1981-2010; Fetterer et al., 2017) are illustrated by blue and yellow dotted lines, respectively. Map was adapted from the Norwegian Polar Institute's Qantarctica package using QGIS 3.28 (Matsuoka et al., 2018). b) Diagram of the Weddell gGyre water masses with vertical temperature profiles collected near to our core sites in Powell Basin (-61.125ºS, -47.675ºW) and South Scotia Sea (-57.125ºS, -42.375ºW; World Ocean Atlas 18; Locarnini et al., 2018). Pathways of ocean currents (ACC: Antarctic Circumpolar Current – black; ACoC: Antarctic Coastal Current – grey) and water masses (ISW: Ice Shelf Water – light blue; HSSW: High Saline Shelf Water – blue; WDW: Warm Deep Water – green; WSDW: Weddell Sea Deep Water – red and WSBW: Weddell Sea Bottom Water – dark magenta) are represented by the colored arrows. AASW: Antarctic Surface Water, PB: Powell Basin, SOM: South Orkney Microcontinent.

3 Materials and methods

3.1 Sediment core and age model

Gravity core PS118_63-1 was recovered from the Powell Basin during the RV *Polarstern* cruise PS118 to the Weddell Sea in 2019 (Fig. 1a; Table 1; Dorschel, 2019). Physical properties, such as magnetic susceptibility (MS) and wet-bulk density, were provided by Frank Niessen (shipboard data; Dorschel, 2019). The age model of core PS118_63-1 is based on ^{14}C radiocarbon dates, the identification of the biostratigraphic marker *Rouxia leventerae*, as well as tuning against records from the EDML ice core ($\delta^{18}O$ and ssNa+) and nearby marine sediment core U1537 (MS, XRF-Fe and opal; Weber et al., 2022). Refer also to Fig. 2 and Supplementary Table S2 for the tie points. Our age model is further substantiated by age constraints of the uranium series disequilibrium, in particular the constant-rate-of-supply model for ^{230}Th-excess (Geibert et al., 2019). Further details on the establishment of the age model and methods are provided in ~~the~~ Supplement S1 and S2.

Table 1. Locations and details of investigated and discussed cores.

Station	Latitude	Longitude	Water depth / Elevation (m)	Recovery (m)	Data source
Marine sediment cores					
PS118_63-1	61° 07.421'S	47° 44.028'W	2626.5	6.88	this study
PS67/219-1	57° 13.22'S	42° 28.02'W	3619	20.71	this study; Xiao et al, 2016a; Xiao et al, 2016b
Ice core					
EDML	75°S	0°	2891		EPICA Community Members, 2006; Fischer et al, 2007

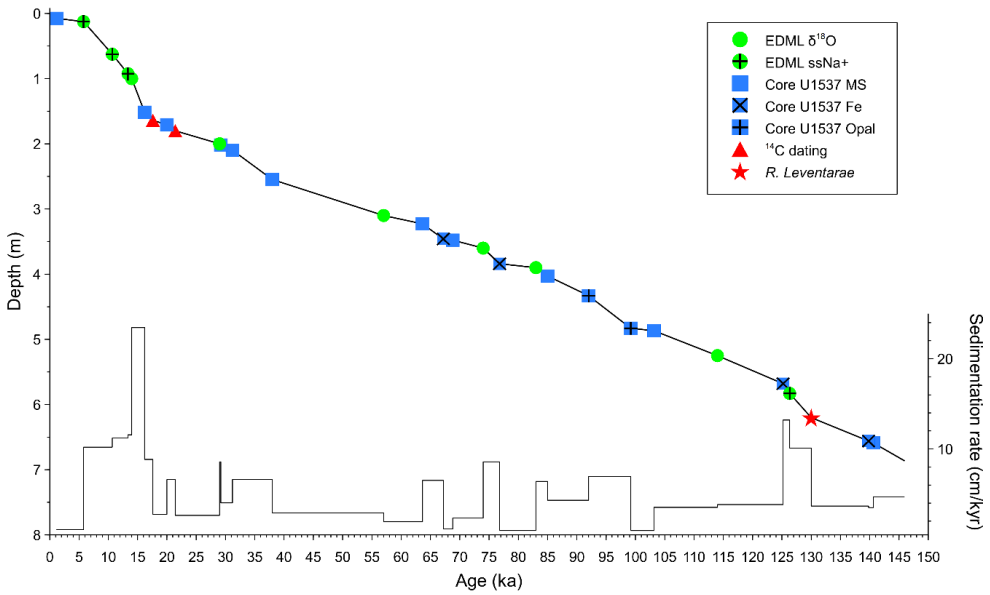

Figure 2.Tie points used for the age-depth model of PS118_63-1 and sedimentation rates. ~~In general,~~ EDML ice core data is indicated by green circles, marine core U1537 data is marked by navy blue square, and

available AMS ^{14}C dates and the biostratigraphic marker (*R. leventerae*) from core PS118_63-1 are depicted by red triangles (^{14}C dates) and a red star (*R. leventerae*).

3.2 Bulk and organic geochemical analyses

A total of 108 sediment samples, each with an approximate thickness of 1 cm, were collected from core PS118_63-1. These samples were then freeze-dried and homogenized using an agate mortar and pestle. All samples were stored in glass vials at -20 °C to prevent degradation. To analyze total organic carbon (TOC), about 0.1 g of sediment was treated with 500 µL of hydrochloric acid to remove any inorganic carbon, including ~~total inorganic carbon and~~ carbonates. After the treatment, the TOC content was measured using a carbon-sulfur analyzer (ELTRA CS800). Routine analyses of standard sediments were conducted before and during each measurement yielding an error of ±0.02%. Biogenic opal was determined using the automated continuous wet-chemical leaching method prescribed in~~following~~ Müller and Schneider (1993) with an error of ±2 wt.%.

For biomarker analyses, around 5-8 g of sediment ~~was~~were extracted and purified in accordance with well-established protocols (Belt et al., 2012; Lamping et al., 2021). Prior to extraction, internal standards, 7-hexylnonadecane (7-HND) and C_{46}-GDGT, were added for subsequent quantification of HBIs and glycerol dialkyl glycerol tetraether (GDGT) lipids. The biomarkers were extracted via ultrasonication (3 x 15 min) using DCM:MeOH (3 x 10 mL; 2:1 *v*/*v*) as solvent. Thereafter, the extracts were fractionated via open-column chromatography, with SiO_2 as the stationary phase, with the HBI-containing fractions eluted with 5 mL *n*-hexane and the GDGT fractions with 5 mL DCM:MeOH (1:1 *v*/*v*).

Compound analyses of HBIs were performed using an Agilent 7890B Gas Chromatograph (GC; fitted with a 30 m DB 1MS column; 0.25 mm diameter and 0.250 µm film thickness) coupled to an Agilent 5977B Mass Selective Detector (MSD; with 70 eV constant ionization potential, ion source temperature of 230°C). The GC oven temperature was first set to 60°C (3 min), then to 150°C (heating rate of 15°C/min), and finally to 320°C (heating rate of 10°C/min), at which it was held for 15 min for the analysis. Helium was used as the carrier gas. Specific compound identification was based on their retention times and mass spectra characteristics (Belt, 2018; Belt et al., 2000).

Quantification of each biomarker was based on setting the manually integrated GC-MS peak area relative to corresponding internal standards and instrumental-compound response factors. The concentrations were subsequently corrected to the extracted sediment weight. For HBI quantification, the molecular ions *m/z* 348 ($IPSO_{25}$) and m/z 346 (z-/e-trienes) were used in relation to its internal standard 7-HND (*m/z* 266). Finally, all biomarker mass concentrations were normalized to the TOC content of each sample. For calculating $PIPSO_{25}$, we adopted the equation as described in Vorrath et al. (2019):

$$PIPSO_{25} = IPSO_{25} / (IPSO_{25} + (\text{phytoplankton marker} \times c)), \quad (1)$$

where *c* is the ratio between the mean concentrations of $IPSO_{25}$ and phytoplankton marker and balances any significant offsets between both biomarker concentrations (Müller et al., 2011).

The GDGT fraction was dried (N_2) and redissolved in 120 µL hexane-isopropanol alcohol (99:1 *v*/*v*), followed by filtration through a polytetrafluoroethylene (PTFE) filter with 0.45 µm pore size

membrane. GDGT measurement was performed using an Agilent 1200 series high-performance liquid chromatograph coupled to an Agilent 6120 atmospheric pressure chemical ionization mass spectrometer. Identification of isoprenoid GDGTs (isoGDGTs) and branched GDGTs (brGDGTs) was based on retention times and mass-to-charge ratios (isoGDGTs: *m/z* 1302, 1300, 1298, 1296 and 1292; brGDGTs: *m/z* 1050, 1036 and 1022). The late eluting hydroxylated-GDGTs (OH-GDGTs) with molecular ions *m/z* 1318, 1316 and 1314 were also determined during the scan of related isoGDGTs, namely *m/z* 1300, 1298 and 1296, respectively (Liu et al., 2012a; 2012b). The relative abundances were subsequently quantified relative to internal standard C_{46} (*m/z* 744), instrumental response factors and the amount of sediment extracted. Mass content of all GDGTs were normalized to the TOC content of each sample.

The ~~calculation of the~~ isoGDGT-based index, TEX_{86}^{L} ~~-~~ (Eq 2) was calculated following Kim et al. (2010) while~~and~~ the conversion to subsurface ocean temperature (OT; 0 - 200 m water depth; Eq 3) was conducted~~ere calculated~~ in accordance to ~~Kim et al. (2010) and~~ Hagemann et al. (2023):

$$TEX_{86}^{L} = \mathrm{Log}_{10}\frac{[isoGDGT-2]}{[isoGDGT-1]+[isoGDGT-2]+[isoGDGT-3]} \quad (2)$$

$$OT\ (°C) = 14.38 \times TEX_{86}^{L} + 8.93 \quad (3)$$

; with a calibration error of ±0.6°C

The OH-GDGT-based index, RI-OH' (Eq 4) and the OT estimation (Eq 5) were determined following Lü et al. (2015). ~~:~~ In their study, they determined that the RI-OH' is significantly correlated with temperature compared to other indices such as TEX_{86} and RI-OH, producing a lower and less scattered residual sea surface temperature (SST) of ±6ºC.

$$RI\text{-}OH' = \frac{[OH-GDGT-1]+2\ x\ [OH-GDGT-2]}{[OH-GDGT-0]+[OH-GDGT-1]+[OH-GDGT-2]} \quad (4)$$

$$RI\text{-}OH' = 0.0382 \times OT\ (°C) + 0.1 \quad (5)$$

(R^2 = 0.75, n = 107, p <0.01)

The index of relative contribution of terrestrial organic matter against that of marine input (branched-isoprenoid tetraether, BIT; Eq 6) was calculated based on Hopmans et al. (2004):

$$BIT = \frac{[brGDGT-I]+[brGDGT-II]+[brGDGT-III]}{[Crenarchaeol]+[brGDGT-I]+[brGDGT-II]+[brGDGT-III]} \quad (6)$$

Lastly, we utilize the ring index (RI; Eqs 7 - 9; Zhang et al., 2016) and methanogenic source indicator index (%GDGT-0; Eq 10; Inglis et al., 2015) to validate against possible non-thermal GDGT sources contribution:

$$RI_{sample} = 0x[isoGDGT\text{-}0] + 1x[isoGDGT\text{-}1] + 2x[isoGDGT\text{-}2] + 3x[isoGDGT\text{-}3] + 4x[crenarchaeol] + 4x[regio.\ crenarchaeol'] \quad (7)$$

$$RI_{calculated} = -0.77 \times TEX_{86} + 3.32 \times (TEX_{86})^2 + 1.59 \quad (8)$$

$$|\Delta RI| = RI_{calculated} - RI_{sample} \quad (9)$$

$$\%isoGDGT\text{-}0 = \frac{[isoGDGT-0]}{[isoGDGT-0]+[Crenarchaeol]} \times 100\% \quad (10)$$

3.3 Diatom analyses

41 smear slides were prepared for a quantitative diatom assemblage analysis at respective depths of the core. Between 400-600 diatom valves, inclusive of those from *Chaetoceros* resting spores (*Chaetoceros* rs), were counted in each sample to ensure statistical significance of the results. Diatoms were identified to species or species group level and, if possible, to forma or variety level. The ~~P~~presence of sea ice is inferred from the percentage of sea-ice indicating diatoms. A combined relative abundance of *Fragilariopsis curta* and *Fragilariopsis cylindus* (hereon referred to as *F. curta* gp) of >3% is used as a qualitative threshold to represent presence of WSI, while values between 1 and 3% estimates the edge of maximum winter sea ice (Gersonde et al., 2003; 2005). Likewise, *Fragilariopsis obliquecostata* is used to indicate summer sea ice (Gersonde and Zielinski, 2000).

We reconstructed WSI concentration (WSIC) by applying a marine diatom transfer function developed by Esper and Gersonde (2014b; TF MAT-D274/28/4an). This transfer function consists of 274 reference samples from surface sediments in the Atlantic, Pacific and western Indian sectors of the SO, with 28 diatom taxa and taxa groups, and an average of 4 analogs (Esper and Gersonde, 2014b). The WSI estimates refer to September sea-ice concentration averaged over a period between 1981 and 2010 at each surface sediment site (National Oceanic and Atmospheric Adminstration, NOAA; Reynolds et al., 2002; 2007). The reference dataset fits our approach as it uses a 1° by 1° grid, providing a higher resolution than previously used, and giving a root mean square error of prediction of 5.52% (Esper and Gersonde, 2014b).

The SSST w~~ere~~as estimated using TF IKM-D336/29/3q (standard error of ±0.86ºC), comprising 336 reference samples from surface sediments in the Atlantic, Pacific and western Indian sectors of the SO, with 29 diatom taxa and taxa groups, and a 3-factor model calculated with quadratic regression (Esper and Gersonde, 2014a). The SSST estimates refer to summer (January-March) temperatures at 10 m water depth averaged over a time period from ≤1900 to 1991 (Hydrographic Atlas of the Southern Ocean; Olbers et al., 1992). The Hydrographic Atlas of the Southern Ocean was used because it represents an oceanographic reference dataset least influenced by the recent warming in the SO (Esper and Gersonde, 2014a).

3.4 Comparison with other proxy records

The EDML ice core and the marine sediment core PS67/219-1 are used in this study for regional comparison due to proximity of both cores to our ~~marine~~ core site (Fig. 1a; see also Table 1 for details). Water isotope ($\delta^{18}O$) and $ssNa^{+}$ records of the EDML ice core were investigated by EPICA Community Members (2006) and Fischer et al. (2007a), respectively. ~~The data is available on Pangaea (EPICA Community Members, 2010; Fischer et al., 2007b).~~ Marine sediment core PS67/219-1, retrieved from

the South Scotia Sea, is located south of the Polar Front and just north of the modern-day winter sea-ice extent. This core offers data on sea ice, SSST and biogenic opal, which extend at least to the LIG period, making it suitable for comparison with ~~inferences from~~ core site PS118_63-1. The chronology and biogenic opal data of core PS67/219-1 was described and published in Xiao et al. (2016b), while investigations on sea-ice reconstruction and SSST for the last 30 ka BP are presented in Xiao et al. (2016a). We further extend~~review~~ the WSIC and SSST records, back to 150 ka BP, using the ~~Imbrie and Kipp Method~~ transfer functions TF MAT-D274/28/4an and TF IKM-D336/29/3q, respectively~~from~~ (Esper and Gersonde, 2014b; 2014b) ~~to achieve a best-fit WSIC estimation for the last 150 kyrs~~.

3.5 Comparison with~~Numerical~~ simulations from climate model(s)

Here, we also analyze model-simulated sea ice, SST and OT estimates for further comparison and evaluation against our proxy results. In this respect, the strength of our modeling approach is twofold. First, the model shall provide reasonable coverage of our intended studied time slices, mainly 6, 21, 125, 128 and 140 ka BP. Second, the model's sensitivity to various climate forcings and boundary conditions across the Quaternary and the entire Cenozoic era must be known. To this end, the Community Earth System Models (COSMOS; Jungclaus et al., 2006) is chosen over other climate models due to its proven track record. For example, the simulation ensemble that has been produced over the years with COSMOS is extensive and not available from international modeling initiatives like the Paleoclimate Modeling Intercomparison Project (PMIP; e.g., Braconnot et al., 2012). Likewise, the model has reproduced various aspects of reconstructed paleoclimate data (see Supplement S3.1 for a list of paleo-studies using the COSMOS model), is shown to be sensitive to paleogeography and climate forcing, and is being characterized by a large Climate and Earth System Sensitivity (Haywood et al., 2013; Stepanek and Lohmann, 2012). Additionally, COSMOS has been proven useful for the study of both warmer (Pfeiffer and Lohmann, 2016) and colder (Zhang et al., 2013; 2017) climates than today and supported research in sometimes very interdisciplinary frameworks (e.g., Guagnin et al., 2016; Klein et al., 2023). For some of the periods relevant here – Holocene, Last Glacial Maximum, LIG – standalone applications of the model are documented (e.g., Pfeiffer and Lohmann, 2016; Wei and Lohmann, 2012; Zhang et al., 2013). More importantly, results from COSMOS have been extensively compared to other models, particularly within the framework of the PMIP, with a focus on the Holocene (Dallmeyer et al., 2013; 2015; Varma et al., 2012) and the Last Interglacial (Bakker et al., 2014; Jennings et al., 2015; Lunt et al., 2013). A relevant inference from comparing PMIP3-class models is that, from the viewpoint of model performance in the SO, COSMOS has shown to be among the models with a comparably minor warm bias in SST (see Fig. 4e and f in Lunt et al., 2013). This makes COSMOS particularly suitable for the studies of ocean temperatures and sea ice around the Weddell Sea. We refer to additional discussion on the rationale for choosing COSMOS over the PMIP models in our study in the Supplement S3.3. Additionally, we also provide an in-depth comparison and evaluation of the simulated results from PMIP3 and PMIP4 ensemble models, within the context of our study, and agreement between COSMOS and PMIP ensemble models in the Supplement S3.4.

3.5.1 Community Earth System Models

In our study, t~~T~~he model data is derived from climate simulations performed with COSMOS. ~~the Community Earth System Models (COSMOS; Jungclaus et al., 2006). For information on its application, refer to S3.1 in the Supplement. Its~~The model's atmospheric module is the fifth generation of the European Centre for Medium-Range Weather Forecasts' Model (ECHAM5), a model of the general circulation of the atmosphere with a spectral dynamical core developed at the Max Planck Institute for Meteorology in Hamburg (Stevens et al., 2013). In our model setup, the ECHAM5 is employed at a truncation of T31, corresponding to a spatial resolution of approximately 3.75°x3.75°, or 375 km at the equator. The atmospheric column is discretized at a resolution of 19 vertical hybrid sigma-pressure levels. The ECHAM5 also encompasses a land surface component (JSBACH) that represents multiple land cover classification types (Loveland et al., 2000; Raddatz et al., 2007). We employ JSBACH's capability to reflect vegetation dynamics (Brovkin et al., 2009) in the course of climate simulations. In our setup, we consider eight different plant functional types that the model adapts in response to changes in the simulated climate, thereby reflecting important feedback processes between vegetation and climate in our simulations. The ocean module is the Max Planck Institute Ocean Model (MPIOM; Marsland et al., 2003), employed at 40 unevenly spaced pressure levels with a bipolar curvilinear GR30 grid that has a formal resolution of 1.8°x3.0°. This enables the horizontal resolution to reach grid cell dimensions that are as small as 29 km at high latitudes. Sea ice computation is based on dynamic-thermodynamic processes with viscous-plastic rheology and follows the formulation by Hibler (1979). Various parameterizations improve the representation of small-scale ocean dynamics in the simulations. For additional information about the parameterizations utilized in our model setup and the steps taken to create geographic setups to apply the model in paleoclimatological research, see, for example, Stepanek et al. (2020) and references therein.

~~3.5.1~~3.5.2 COSMOS~~Climate~~ simulation settings

The simulation ensemble consists of a pre-industrial reference state (simulation *piControl*, 1850 CE; Wei and Lohmann, 2012), a Holocene climate (simulation *mh6k*, 6 ka BP; Wei and Lohmann, 2012), an LGM state (simulation *lgm21k*, 21 ka BP; Zhang et al., 2013), two time-slices of the LIG, one for conditions at 125 ka BP (simulation *lig125k*) and one for conditions at 128 ka (simulation *lig128k*), and a Penultimate Glacial Maximum (PGM) climate (simulation *pgm140k*). In order to filter out short-term climate variability on interannual and multidecadal time scales, and to derive average climatic conditions that are representative of the respective Quaternary time-slice, we average the modeled climate state over a period of 100 model years. For interglacial climates we employ a modern geography. The boundary conditions for the Last and Penultimate Glacial Maximum have been set up for a study by Zhang et al. (2013) based on the PMIP3 modeling protocol. Details of the ice-sheet reconstruction, that is a blend of ICE-6G v2.0 (Argus and Peltier, 2010), ANU (Lambeck et al., 2010) and GLAC-1a (Tarasov et al., 2012), are described by Abe-Ouchi et al. (2015). For further details on the climate states and simulation configurations, we refer to S3.2 and Supplementary Table S3, respectively in the Supplement. For analysis purposes, the climate model output is interpolated from the native grid of the ocean model to a regular resolution of 0.25°x0.25°, in order to preserve the geographic features of the

ocean model. Additionally, we also derived climate model data specifically tailored to the two marine core sites discussed in this paper, achieving this through interpolating relevant climate fields to the geographic coordinates of each core using a nearest-neighbor interpolation algorithm. Any reference to the modeled sea-ice edges in this publication specifies the isoline of 15% of sea-ice cover.

4 Results

4.1 HBIs

~~In this study, t~~The concentration of the sea~~-~~ice biomarker ($IPSO_{25}$; Fig. 3a) in core PS118_63-1 varies significantly between 0 and 2.41 µg/g OC. Peak concentration is found at ca. 112 ka BP, while very low concentrations are noted throughout MIS 2-4, 5d, 5e and 6. Moderate to low concentrations are observed during MIS 1 and through both terminations. The concentration of the ice marginal-open water phytoplankton biomarkers varies between 0 - 3.03 µg/g OC (z-triene) and 0 - 0.76 µg/g OC (e-triene; Fig. 3b). Higher concentrations are observed at MIS 1 and 5e, while lower concentrations are noted throughout MIS 2-4, 5d and 6. In our investigation, we utilized both z- and e-trienes, respectively, to calculate the semi-quantitative spring/summer sea-ice indices ($P_{z/e}IPSO_{25}$). This combined use of biomarkers, indicative of ice marginal-open water conditions and $IPSO_{25}$, helps to circumvent ambiguous interpretations especially when dealing with scenarios of permanent sea ice and open ocean conditions. Our P_zIPSO_{25} index ranges between 0.09 and 1, while the P_eIPSO_{25} index varies from 0.06 to 1 (Fig. 3c). Instances, where both values of $IPSO_{25}$ and z-/e-triene are zero, the $P_{z/e}IPSO_{25}$ index is assigned a value of 1, indicating permanent ice cover. Both index profiles presented a similar trend ($r = 0.98$), with higher values (>0.8) throughout MIS 2-4, 5d and 6, while reduced values noted for MIS 1 and 5e. Notably, the lowest $P_{z/e}IPSO_{25}$ values (<0.2) are observed during MIS 5e, specifically between 119 and 128 ka BP, signifying a distinct decline in sea ice and more open ocean conditions during this time interval. Comparable low $P_{z/e}IPSO_{25}$ values are also observed around 4 and 12 ka BP.

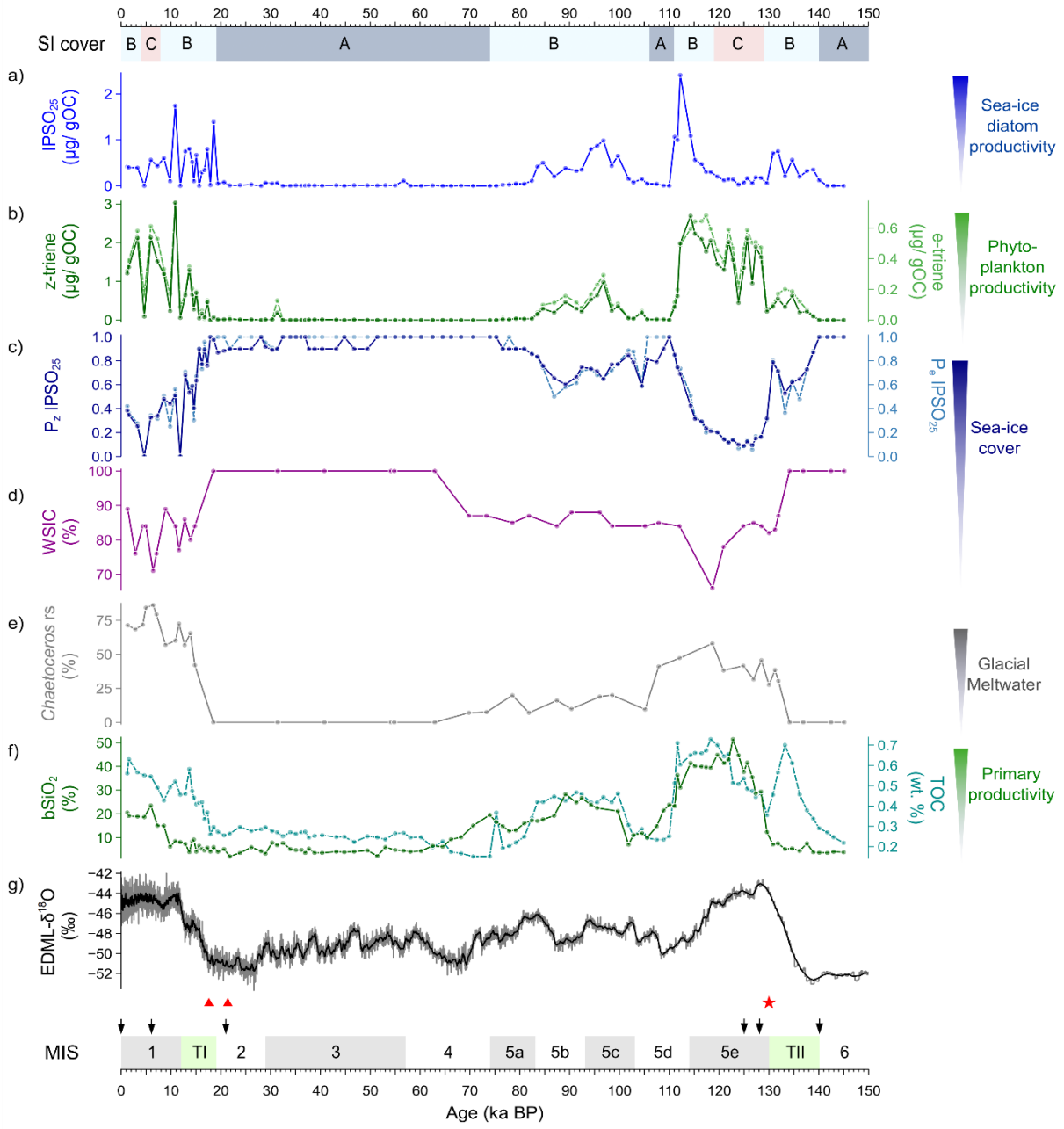

Figure 3. Multiproxy analyses of sea-ice conditions in Powell Basin, reconstructed from marine sediment core PS118_63-1. Sea-ice (SI) cover scenarios: A - permanent sea-ice cover (dark blue), B - dynamic sea-ice cover (light blue) and C - minimal sea-ice cover (light red). From top to bottom: a) HBI-based sea ice biomarker ($IPSO_{25}$), b) HBI-based phytoplankton biomarkers (z-/e-trienes), c) Phytoplankton-$IPSO_{25}$ index ($PIPSO_{25}$), d) Diatom-based winter sea-ice concentration (WSIC), e) Glacial meltwater indicator (*Chaetoceros* resting spores) and f) Biogenic opal ($bSiO_2$), and total organic carbon (TOC). Atmospheric temperature is implied by g) the $\delta^{18}O$ record from the EDML ice core. AMS ^{14}C dates are marked with red triangles, the biostratigraphic marker (*R. leventerae*) is indicated by the red star. The black arrows delineated the time-slices for the model simulations in this study. MIS stages are depicted in alternating grey (odd) and white (even) shades, while the terminations TI and TII are shown in green.

4.2 GDGTs

Downcore OT estimates using the RI-OH' index cover a temperature range between -2.5 and 1.0°C (Fig. 4g) while TEX_{86}^{L}-derived OT fluctuates between -2.6 and 1.0°C (Supplementary Fig. S5a). These GDGT-based OTs likely reflect (mean) annual ocean temperature between the water depths of 0 and 200 m (Hagemann et al., 2023; Kim et al., 2012; Liu et al., 2020), and this seems to be

corroborated by the modern-day vertical ocean temperature profile nearby core site PS118_63-1 (Fig. 1b). Certainly, these minimum temperatures of less than -1.9°C – freezing temperature of seawater – need to be considered with caution due to factors influencing the ocean temperature calibration, for example, ~~as the calibration equations for RI-OH' and TEX_{86}^{L} are based on datasets with residual errors of 6°C (Lü et al., 2015) and 0.6°C (Hagemann et al., 2023), respectively. Other factors influencing the ocean temperature calibration include~~ bias from terrestrial input, water depth, use of satellite-assigned ocean temperature below the freezing point of seawater and inadequate samples from polar areas (Fietz et al., 2020; Xiao et al., 2023). Nevertheless, both OT proxies consistently indicate a cold-water subsurface regime (0 – 200 m; <1°C) with a 0-2°C temperature fluctuation, and no significant glacial/interglacial variability over the last 145 kyrs. We further note that the RI-OH'-based OTs fluctuate within the error range of the temperature calibration based on a global surface sediment dataset (Lü et al., 2015) and call for attention when interpreting OT variability. Calculation of terrestrial originated-GDGT (i.e. BIT) and isoGDGT-related indices ~~such as BIT, (i.e.~~ %isoGDGT-0 and ΔRI; Supplementary Fig. S5b-e) reveals the presence of potential non-thermal influences on the TEX_{86}^{L} index, which may lead to bias in the temperature reconstruction (see also S4 in the Supplement). In light of the ~~conflicting trends and potential~~ non-thermal influences on TEX_{86}^{L}, we have decided not to further discuss on the TEX_{86}^{L}-derived OT in this paper. Concerning the RI-OH' approach, the presence of OH-GDGT has, thus far, only been observed within the cultivated marine thaumarchaeal group I.1a (Pitcher et al., 2011; Liu et al., 2012b; Elling et al., 2014; 2015). Its absence in the terrestrial thaumarchaeal group I.1b (Sinninghe Damsté et al., 2012) suggests a predominantly planktic origin (Lü et al., 2015). While both isoGDGTs and OH-GDGTs are derived from the phylum *Thaumarchaeota*, variances in their ring composition indicate that the OH-GDGTs may be biosynthesized from different source organisms or differing conditions (Liu et al., 2012b). Additionally, previous studies compared the relationship between various GDGT-based indices (i.e. RI-OH, RI-OH', TEX_{86} and TEX_{86}^{L}) and temperature, and determined that the RI-OH'-temperature relationship shows the most significant correlation in cold-water (<15ºC) regions, making the RI-OH' a robust temperature proxy for the (sub)polar regions (Lü et al., 2015; Lamping et al., 2021; Park et al., 2019; Fietz et al., 2020). Therefore, we suggest that the RI-OH' index holds promise as a potential OT proxy for our study site. However, further work on the distribution of OH-GDGT and calibration studies are still essential to enhance the applicability of RI-OH' as a (paleo)temperature proxy.

4.3 Diatoms

The diatom-based data for cores PS118_63-1 and PS67/219-1 are presented in Fig. 4c and d. For core PS118_63-1 from the Powell Basin, the relative abundance of sea ice-related diatoms ranges between 2 and 39% for *F. curta* gp, and from 0 to 6% for *F. obliquecostata*. The relative abundance of diatoms between ca. 15 and 70 ka BP, and before 131 ka BP, is rare/absent (Fig. 4c). Such cases generally indicate the presence of permanent sea ice over the core site (Zielinski and Gersonde, 1997). We, therefore, assign the diatoms' relative abundance as 0, and WSIC as 100%, to above-mentioned time intervals (i.e., MIS 2 - 4 and 6). The abundance of *F. curta* gp is noted to be above the 3% threshold (indicative of presence of WSI) throughout the remaining time periods – except at 6 ka BP, where the

lowest abundance (2%) is observedregistered. Whereas, theA relative abundance of *F. obliquecostata* fluctuates around the 3% threshold, likely indicatesing a dynamic summer sea-ice edge over the area during MIS 1 and 5. The WSIC across the rest of the time frame, namely MIS 1 and 5, isare generally high (>75%) as well, with a couple of lower WSIC observed at ca. 6 ka BP (71%) and at 119 ka BP (66%). The abundance of *Chaetoceros* resting spores (*Chaetoceros* rs) varies between 0 and 86%, with higher values noted during MIS 1 and 5e (Fig. 3e). Such increases in the abundance of the *Chaetoceros* rs imply the presence of glacial meltwater at the core location (Crosta et al., 1997). The diatom-derived SSST – typically indicating summer ocean temperature between the water depth of 0 and 10 m – coversrecords a temperature range between -0.8 and 0.4°C (Fig. 4h), and describes a cold-water region during MIS 1 and 5, similar to the RI-OH'-derived OT (Fig. 4g).

To the north in the South Scotia Sea, core PS67/219-1 documents an overall lower percentage of sea ice-related diatoms (Fig. 4d). Similar to core PS118_63-1, the relative abundance of *F. curta* gp (0.5-20%) is noted to be mostly above the 3% threshold, indicating presence of WSI over the region, with higher abundance observed for MIS 2 and 3, and lowest abundance (<1%) observed during MIS 5e. However, the relative abundance of *F. obliquecostata* for core PS67/219-1 remains below the 3% threshold, between 0 and 3%, suggesting a lack of summer sea ice over the core site. The percentage of WSIC in the South Scotia Sea is also lower than that ofat Powell Basin, withhaving a record of 37-82%, with the lowest WSIC noted at MIS 5e. The diatom-based SSST documents a SSST range of -0.7 to 2°C, with colder SSST registered during MIS 2 and 3, and warmer SSST noted during MIS 1 and 5e (Fig. 4i).

4.4 TOC and Biogenic opal

In this study, both TOC and biogenic opal (Fig. 3f) are interpreted to reflect used as indicators of primary productivity (r = 0.65). The TOC content varies between 0.2 and 0.7% while biogenic opal ranges from 2 to 51%. Highest productivity is observed during MIS 1 and 5e, indicative of favorably warmer conditions that promote primary productivity blooms at the core location. A rather moderate productivity level is observed between MIS 5a to c, while lowest values are noted for MIS 2-4, 5d and 6. Both profiles also exhibit some differences. For example, peak biogenic opal occurs around 124 ka BP whilst peak TOC is recorded at 119 ka BP. We also observe a more pronounced increase in the TOC content during the terminations than in the biogenic opal content. This is likely due to greater input from non-siliceous organisms, such as archaeal, bacterial and terrestrial input (see Supplementary Fig. S4).

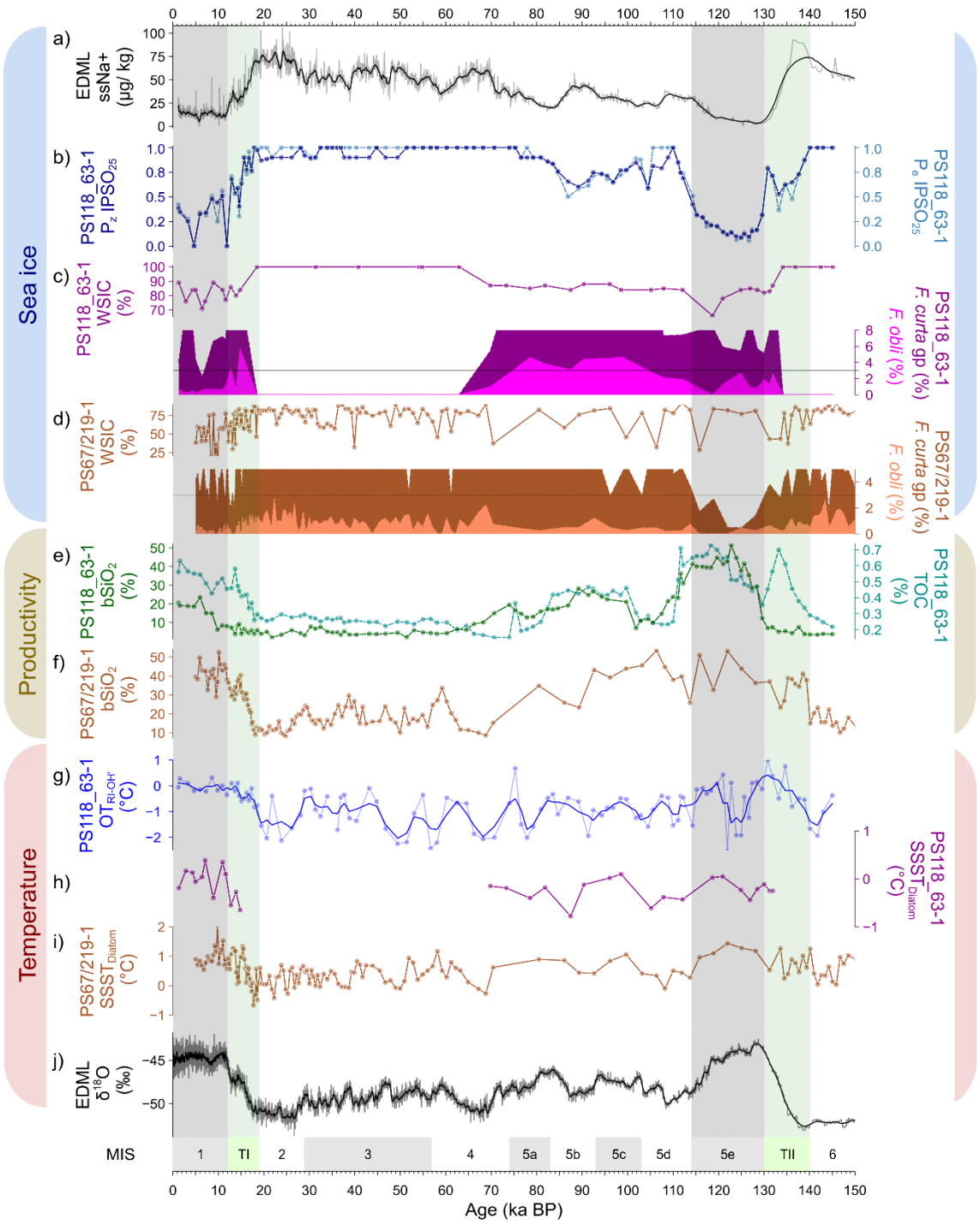

Figure 4. Regional sea ice, productivity and temperature variability in the South Atlantic sector of the Southern Ocean as inferred from EDML ice core, Powell Basin (PS118_63-1) and South Scotia Sea (PS67/219-1). For sea ice: a) sea-ice estimation (ssNa+; black) from EDML ice core, b) HBI-based sea ice indicator (P_zIPSO_{25} – dark blue; P_eIPSO_{25} – dotted light blue), c) diatom-based winter sea-ice concentration (WSIC – dark magenta), *F. curta* group (*F. curta* gp – dark magenta), *F. obliquecostata* (*F. obli* – light magenta) from PS118_63-1, and d) diatom-based WSIC (brown), *F. curta* group (*F. curta* gp – brown), *F. obliquecostata* (*F. obli* – light brown) from PS67/219-1. For productivity: e) biogenic opal ($bSiO_2$ – dark green) and total organic carbon (TOC – dotted light green) from PS118_63-1 and f) $bSiO_2$ (brown) from PS67/219-1. For temperature: g) RI-OH'-derived subsurface ocean temperature with three-point smoothing ($OT_{RI\text{-}OH'}$ – navy blue) and h) summer sea surface temperature ($SSST_{Diatom}$ – dark magenta) from PS118_63-1, i) $SSST_{Diatom}$ (brown) from PS67/219-1 and j) EDML water stable isotope record ($\delta^{18}O$ – black). The 3% threshold for diatom species relative abundance is indicated by a black horizontal line. MIS stages are depicted in alternating grey (odd) and white (even) shades, while the terminations TI and TII are shown in green. For the full *F. curta gp* abundance data, refer to the relevant datasets in Pangaea.

4.5 Sea-ice conditions – a multiproxy approach

Using a multiproxy approach, our analysis of the data from core PS118_63-1 provides a continuous glacial-interglacial sea-ice history in the Powell Basin since the PGM. We distinguish three different sea-ice scenarios, spanning the last 145 kyrs (Fig. 3).

A) Perennial sea-ice cover. This scenario is characterized by remarkably low (sea ice) diatom abundances, minimum $IPSO_{25}$ and HBI-triene concentrations, as well as minimum $bSiO_2$ and TOC contents. We deduce the presence of maximum WSIC and a spring/summer sea ice ($PIPSO_{25}$) cover. These results indicate a glacial setting, with our core site situated under a perennial sea ice or ice-shelf cover suppressing and exposed to minimal primary production in the water column. Such a scenario persisted throughout the glacial periods MIS 2-4, MIS 6, and during MIS stadial 5d.

B) Dynamic sea-ice cover. This scenario is described by fluctuations in each of the proxy profiles, in particular WSIC, $PIPSO_{25}$, HBI-trienes, $bSiO_2$ and TOC contents. These records reflect the dynamic nature of sea-ice conditions over our core site, with varied primary production at different time intervals. This scenario is prevalent during periods of climate transition, such as terminations I and II, and during MIS 1 and 5a-c.

C) Minimal (winter-only) sea-ice cover. This scenario is denoted by a considerably reduced sea-ice diatom ($IPSO_{25}$) production, WSIC and $PIPSO_{25}$, coupled with high phytoplankton productivity (HBI-trienes), $bSiO_2$ and TOC contents. These findings suggest that our core site experienced ice-free or winter-only ice conditions, permitting enhanced primary production in the water column. This scenario occurs in short time intervals within the interglacials, for example, 8-5 ka BP (MIS 1) and 130-119 ka BP (and MIS 5e).

4.6 Inferences from COSMOS numerical climate simulations

Covering the Atlantic sector of the SO, Here, we present our model-simulated sea ice, SST and OT (at 220 m water depth), covering the Atlantic sector of the SO, at six glacial-interglacial time-slices: cover the PGM at 140 ka BP, LIG at 128 (sea ice only) and 125 ka BP, LGM at 21 ka BP, Holocene at 6 ka BP and pre-industrial (Fig. 5 - 7). In For Fig. 5, the left column (Fig. 5a) shows the simulated sea-ice cover/extent for the spring/summer seasons (NDJFMA, this averaging period considers the time lag in sea-ice extent vs. spring/summer temperature evolution) while the right column (Fig. 5b) illustrates the simulated sea-ice cover/extent for the winter (ASO) season. In general, a greater sea-ice cover is generally observed during winter than spring/summer for each time-slice. During the glacial periods, the model highlights a northward expansion of the sea-ice extent beyond both marine core sites (PGM: Fig. 5.1; LGM: Fig. 5.4). At the more southern site (Powell Basin; core PS118_63-1), the modeled glacial sea-ice cover varies between ~93 to 94% (winter) and ~79 to 82% (spring/summer), while at the more northern site (South Scotia Sea; core PS67/219-1), sea-ice cover varies around ~91% (winter) and ~26 to 34% (spring/summer). In contrast, during the interglacials, fluctuations in the sea-ice extent are more pronounced fluctuates between seasons. WSI extent is observed to be located north of both core sites (Fig. 5.2b, 5.3b, 5.5b and 5.6b), with the WSI cover ranging between ~86 and 89% at core site PS118_63-1, and ~52 to 69% at core site PS67/219-1. While dDuring spring/summer, the sea-ice extent

retreats to a latitude between both sites (Fig. 5.2a, 5.3a, 5.5a and 5.6a), with the spring/summer sea-ice cover varying from ~31 to 35% at core site PS118_63-1 and between ~0 and 4% at core site PS67/219-1.

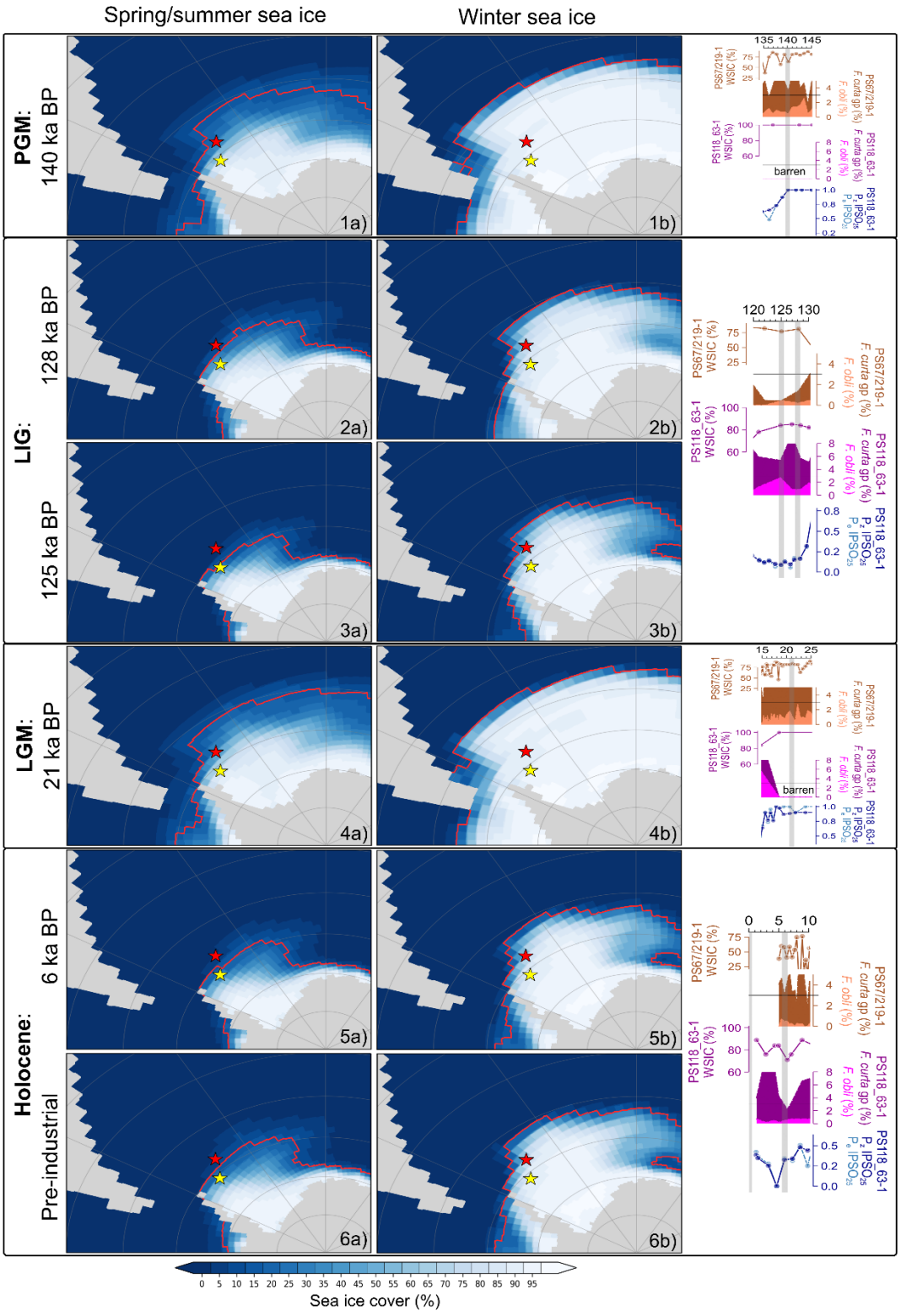

Figure 5. Model-simulated mean a) spring/summer (NDJFMA) and b) winter (ASO) sea-ice cover for the various time slices: 1) PGM: 140 ka BP, 2) LIG: 128 ka BP, 3) LIG: 125 ka BP, 4) LGM: 21 ka BP, 5) mid-Holocene: 6 ka BP and 6) Pre-industrial. The red line depicts the sea-ice extent and is defined as the isoline of 15% sea ice coverage. Location of marine sediment cores is indicated with stars: PS118_63-1 (yellow)

and PS67/219-1 (red). Proxy-derived winter sea-ice concentration (WSIC), sea ice-related diatom abundance and spring/summer sea ice ($PIPSO_{25}$) for each time slice are shaded in grey~~in yellow shadings~~.

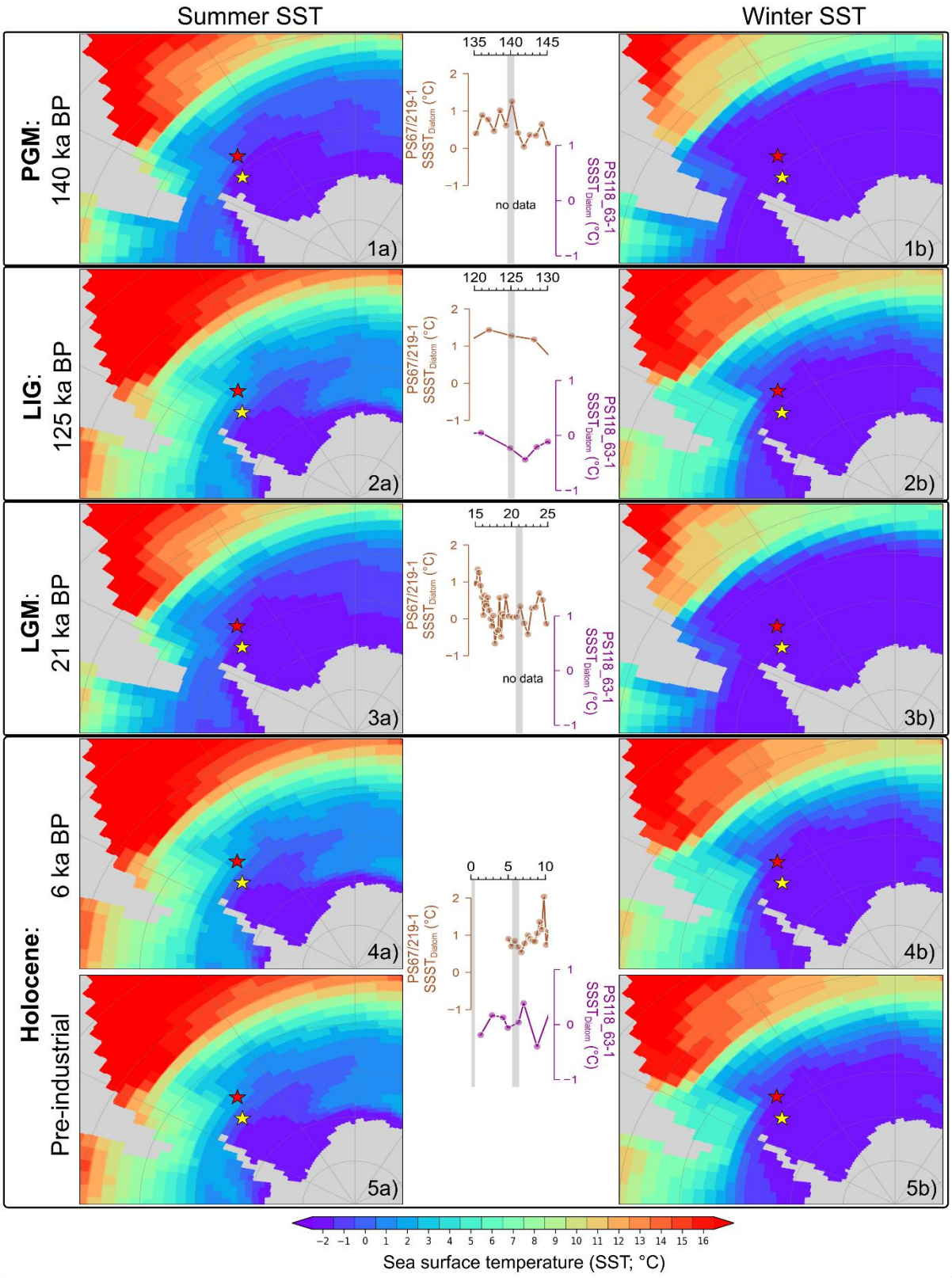

Figure 6. Model-simulated mean a) summer (DJF) and b) winter (JJA) sea surface temperature (SST) for the various time slices: 1) PGM: 140 ka BP, 2) LIG: 125 ka BP, 3) LGM: 21 ka BP, 4) mid-Holocene: 6 ka BP and 5) Pre-industrial. Marine sediment cores, PS118_63-1 (yellow) and PS67/219-1(red), are indicated by the colored stars. Diatom-based summer sea surface temperature ($SSST_{Diatom}$) for the respective time slice is highlighted in grey~~yellow~~.

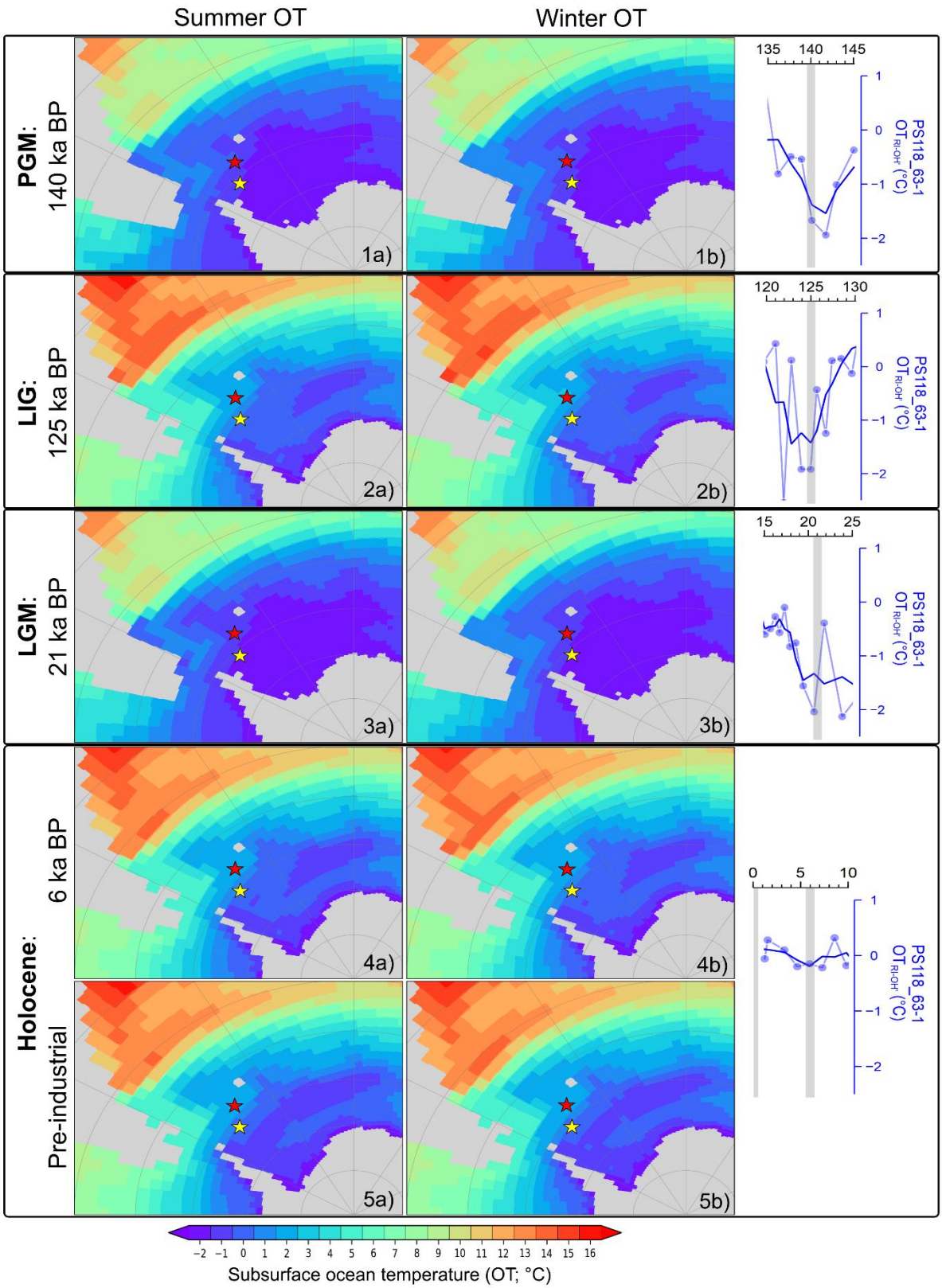

Figure 7. Model-simulated mean a) summer (DJF) and b) winter (JJA) subsurface ocean temperature (OT; 220 m water depth) for the various time slices: 1) PGM: 140 ka BP, 2) LIG: 125 ka BP, 3) LGM: 21 ka BP, 4) mid-Holocene: 6 ka BP and 5) Pre-industrial. Marine sediment cores are presented in colored stars: PS118_63-1 (yellow) and PS67/219-1(brown). Biomarker-based ocean temperature with three-point smoothing ($OT_{RI\text{-}OH'}$) for the respective time slice is indicated by the grey~~yellow~~ shadings.

For the SST and OT, the left columns (Fig. 6a and 7a) represent the summer (DJF) temperature, and the right columns (Fig. 6b and 7b) depicts the winter (JJA) temperatures, respectively. The simulated~~- result observed for the~~ SST (Fig. 6) appears similar to that of the modeled sea~~-~~-ice output. In general, widespread, low SST, close to the freezing point of seawater (that is approximately -1.9°C at salinity values modeled in the SO in our simulations), is exhibited across all time-slices during winter (Fig. 6b), while in summer (Fig. 6a), low SST mainly occurs in the Weddell Sea and along the coast of the Antarctic continent. For instance, at the core site PS118_63-1 in Powell Basin, Weddell Sea, there is no observed difference in SST between winter and summer during the glacial periods PGM (Fig. 6.1) and LGM (Fig. 6.3). Both sites were surrounded by sea ice during these periods (Fig. 5.1 and 5.4). However, in interglacials, a seasonal SST cycle of ~1°C is noted in the basin (Fig. 6.2, 6.4 and 6.5). In contrast, at the more northern core site PS67/219-1, the model estimates a seasonal SST cycle of ~1°C during the glacial periods (Fig. 6.1 and 6.3) and ~3.4°C during the interglacial (Fig. 6.2, 6.4 and 6.5). Moreover, the modeled climate states are characterized by spatial SST gradients between the two core locations of between 0°C (glacial) and ~0.4°C (interglacial) during winter. For summer SST, the gradient between the two core locations varies between ~1°C (glacial) and ~2.8°C (interglacial). As for the simulated OT, the model displays~~simulates~~ a ~1.6 and ~3°C glacial-interglacial variation at core sites PS 118_63-1 and PS67/219-1, respectively, but no appreciable OT change is observed between the winter and summer seasons of each time slices ~~if the glacial-interglacial variability range is taken as a reference~~ (Fig. 7). The model also reveals a spatial OT gradient between both marine core sites of ~0.7°C (glacial) and ~2.1°C (interglacial).

5 Discussion

5.1 Regional sea ice and oceanic conditions

5.1.1 Penultimate Glacial Maximum – Termination II

Our records show~~ed~~ that during the PGM, the Powell Basin (core PS118_63-1) remained under a layer of persistent (sea) ice cover, as evidenced by a 100% WSIC and peak $PIPSO_{25}$ values inferred from the absence of diatoms, alongside notable reductions in $IPSO_{25}$ and HBI-triene concentrations (see also Sect 4.1 and 4.3). This coincided with the lowest levels of primary production~~s~~ reflected~~observed~~ in the biogenic opal and TOC records (Fig 4b, c and e). This condition persisted until ca. 140 ka BP, when a decline in spring/summer sea ice ($PIPSO_{25}$) is observed, accompanied by a rise in TOC and subsurface ocean temperature (Fig. 4b, e and g). ~~While a~~At a more northern~~n~~ly location in the South Scotia Sea, core PS67/219-1 records a less pronounced~~more dynamic~~ sea-ice cover~~condition~~ during the PGM with~~. High~~ WSIC ~~(~~fluctuating at around 65%~~),~~ and~~together with~~ a 1-3% abundance of *F. obliquecostata*~~,~~ suggesting the proximity of a permanent sea-ice edge (Fig. 4d). These findings from the geological record are supported by our model simulation for the 140 ka BP time-slice, which shows an overall high simulated-WSI cover (94%; 92%), but slightly lower simulated-spring/summer sea-ice cover (79%; 27%) at core sites PS118_63-1 and PS67/219-1, respectively (Fig. 5a). Likewise, higher $ssNa^+$ concentrations and $\delta^{18}O$ values from EDML ice core point to cold conditions

and an extensive sea-ice cover in the Atlantic region (Fig. 4a and j; EPICA Community Members, 2006; Fischer et al., 2007a).

Termination II (TII; 140-130 ka BP) marks the transition from a glacial into an interglacial environment. The onset of this deglaciation was probably initiated by a warming event caused by a maximum southern high latitude summer insolation at around 138 ka BP (Bianchi and Gersonde, 2002; Broecker and Henderson, 1998) and further sustained by the Heinrich Stadial 11 (HS11) event occurring in the Northern Hemisphere (NH) between 135 and 130 ka BP (Turney et al., 2020). The HS11 is a prominent North Atlantic meltwater event that may have triggered the eventual shutdown of the AMOC, thus reinforcing the warming in the SO via the bipolar seesaw effect (Marino et al., 2015).

In the Powell Basin, the WSIC remains high (100%) and only starts to decrease (80%) at ca. 134 ka BP, while gradually declining $PIPSO_{25}$ values since 140 ka BP accompany the onset of the deglaciation and mark a shift from a perennial sea ice to a dynamic seasonal sea-ice cover (see Sect 4.5 for ~~a~~ definition). A concurrent rise in subsurface ocean temperature is also observed during this timeframe. In contrast, core PS67/219-1 in the South Scotia Sea recorded a different sea-ice regime~~.~~ ~~An oscillating~~ with generally lower and declining~~e in~~ WSIC and <1% abundance of *F. obliquecostata*, suggesting a less extended sea-ice cover~~variable WSI cover with a distal summer sea-ice edge~~. The different sea-ice conditions in both regions are supported by a higher biogenic opal production recorded in the South Scotia Sea as compared to the minimum biogenic opal content observed for the Powell Basin (Fig. 4e and f). The Powell Basin TOC profile is also different from its opal counterpart, with the former peaking between 135-131 ka BP. We surmise that this peak may relate to a preferential growth environment for non-siliceous marine organisms and/or increased input of terrestrial organic matter during this interval.

The persistent warming was interrupted by a short period of spring/summer sea ice ($PIPSO_{25}$) re-expansion and weakened decline in WSI towards the end of TII (ca. 132-130 ka BP; Fig 4b and c), along with an increasing *Chaetoceros RS* abundance that peaks at ca. 131 ka BP (Fig. 43e). These conditions coincide with the northward shift of the sea-ice edge at ODP Site 1094 around 129.5 ka BP (Bianchi and Gersonde, 2002). A comparable reduction in SSST at around 131 ka BP is also observed in the South Scotia Sea (core PS67/219-1, Fig. 4i) and apparent at ODP Site 1089 and core PS2821-1 (Cortese and Abelmann, 2002). In the Powell Basin, however, this cooling event is not reflected in ocean temperature (Fig. 4g) and we propose that the lack of temperature change during this event may be attributed to the discharge of meltwater from expanding sub-ice shelf cavities, which caused a stronger stratification and an effective isolation of the warmer subsurface layer.~~also associated with reduced primary production, although no decline in temperature is detected (Fig. 4). Considering age uncertainties, we postulate that the sea ice expansion and ocean cooling are part of the same event, likely influenced by meltwater influx as a result of cavity(ies) expansion beneath major Antarctic ice shelves (such as the Filchner-Ronne Ice Shelf; Ashley et al., 2021; Hellmer, 2004).~~

5.1.2 Last Interglacial - MIS 5 stadials/interstadials

Following the short-lived sea~~-~~ice expansion in Powell Basin at the end of TII, we observe a rapid decline, and minimum spring/summer sea-ice cover is reached (see Sect 4.5) by ca. 129 ka BP (Fig.

4b). Lowest spring/summer sea ice ($PIPSO_{25}$) is observed between 126 and 124 ka BP, while minimum WSIC is observed around 119 ka BP. These conditions promoted primary productivity, as reflected in the maximum biogenic opal and TOC contents, at the respective timeframes (Fig. 4e). Likewise, sea ice and temperature profiles from core PS67/219-1, the EDML ice core and model simulations also favor a warm and predominantlytely open ocean condition for the South Atlantic sector throughout the LIG (Fig. 4d, 4i, 5.3 and 6.3; EPICA Community Members, 2006; Fischer et al., 2007a). Holloway et al. (2017) investigated the simulated-spatial structure of the Antarctic WSI minimum at 128 ka BP with respect to the $\delta^{18}O$-isotopic peak recorded in the East Antarctica ice cores. They tested numerous WSI retreat scenarios and concluded that the $\delta^{18}O$ maximum could be explained by a significant decline in Antarctic WSI, with the Atlantic sector experiencing the largest reduction of 67%. Contrastingly, while our spring/summer sea ice ($PIPSO_{25}$) data aligns with their $\delta^{18}O$-accorded simulated-findings, our diatom data - revealing a constant presence of WSI in the Powell Basin and South Scotia Sea with even minor increases between 130 and 127 ka BP - disagrees. Holloway et al. (2017)Furthermore, the WSI record from marine core PS2305-6, located slightly north of our core site, also indicates the presence of WSI during MIS 5e (see also Supplementary Table S1 in Holloway et al., 2017; Bianchi and Gersonde, 2002; Gersonde and Zielinski, 2000). We assume that the modeled winter sea-ice retreat seems to be valid for more distal ocean areas, whereas at the core sites in Powell Basin and South Scotia Sea, ice-sheet-derived meltwater may have acted as a driving mechanism fostering local sea-ice formation during winter, which is not captured by the simulation in Holloway et al. (2017). Our interpretation is, that such inconsistency could possibly be linked to sea-ice variations between seasons (Eayrs et al., 2019; Roach et al., 2022). MoreoverInterestingly, the hereinour simulated sea ice at the 128 ka BP time-slice corroborates our proxy-based data, indicating the presence of WSI in the region amidst lower sea-ice concentration and continued retreat of sea ice over the spring/summer seasons (Fig. 5.2). A similar sea-ice scenario is also established for the 125 ka BP time-slice, consideredknown to be the warmest period of the LIG (Fig. 5.3; Goelzer et al., 2016; Hoffman et al., 2017), where Southern Hemisphere (SH) mid- to high-latitude spring insolation forcing reached a maximum within the period from 130 ka BP to 125 ka BP (Lunt et al., 2013). The contrasting observation between our marine sediment proxy and model data against that of the ice core $\delta^{18}O$-accorded simulated-finding emphasizes the need for more robust marine-based reconstructions, especially south of the modern sea-ice edge, to sufficiently substantiate model results for these regions, and to enable comprehensive input knowledge for future model simulations and predictions (Holloway et al., 2017; Otto-Bliesner et al., 2013).

The reconstructed SSST trends in the Powell Basin and the South Scotia Sea are largely comparable with the atmospheric temperature profile from the EDML ice core (Fig. 4h-j), suggesting atmosphere-ocean interactions in the study arearegions. The lack of significant glacial-interglacial temperature variability within the Powell Basin could potentially be linked to its locality and close proximity to the continental margin, where constant mixing of cold ice-shelf water with the WDW persists. Within the Powell Basin, both the SSST and subsurface ocean temperature started to decrease around 130 ka BP. While the SSST appeared to have cooled from -0.2°C to -0.4°C (127 ka BP) and recovered thereafter – similar to the dip observed in the EDML $\delta^{18}O$ profile, – the subsurface

ocean temperature declined distinctly from 0 to ca. -1.9°C and remained cold until 124 ka BP (Fig. 4g and h). The variance in the magnitude of decline observed between the two temperature records (SSST vs. OT) may be attributed to the distinctly different seasonal signals depicted by the proxies (i.e., summer vs. annual temperature) and water depths (0-10 m vs. 0-200 m; see also Sect 4.2 and 4.3). We speculate that the decline in seawater temperature since 130 ka BP may be the result of intense melting of the Antarctic ice sheet and sea ice, leading to a freshening of coastal ~~This approximate 3-kyr interval of further-reduced subsurface temperature coincided with a brief surge in the North Atlantic Deep Water (NADW) formation, instigated by the collapse of the AABW between 127 and 125 ka BP (Hayes et al., 2014). This event triggered an intense incursion of WDW upon a receding West Antarctic Ice Sheet (WAIS) margin, resulting in the discharge of a substantial volume of meltwater into the southern Weddell Sea (Marino et al., 2015). We hypothesize that, similar~~waters. Similar to the modern-day Weddell Gyre circulation (see Sect 2 for details), the increased discharge of cold (sea) ice-shelf meltwater into the Powell Basin, via the Antarctic Coastal Current and Antarctic Slope Current, ~~and~~ may have deepened the cold-water stratification in the basin, thus causing the observed dip in ocean temperature~~short-lived extreme cold subsurface water regime~~ between 13027 and 124 ka BP. ~~There has been substantial evidence supporting a significant retreat (or collapse) of the WAIS during the LIG. For example,~~ Turney et al. (2020) discovered that the WAIS had retreated from the Patriot Hills blue ice area by the end of TII (130.1 ± 1.8 ka BP). This area is located 50 km inland from the present-day grounding line of the Filchner-Ronne Ice Shelf. Their investigation revealed a 50 kyrs hiatus in the blue ice record, indicative of a collapse of the ice shelf at the end of TII, followed by its subsequent recovery during late MIS 5. Holloway et al. (2016) also propose ~~for~~ a maximum ice-sheet retreat at around 126 ka BP based on distinct differences between the isotopic records observed for Mt Moulton and East Antarctic ice cores. Assuming that~~,~~ the distinct reduction in spring/summer sea-ice recorded in core PS118_63-1 was not confined to the Powell Basin but may reflect a more extensive sea ice decline in the Weddell Sea embayment, we posit that this loss of sea ice (i.e., the loss of an effective buffer protecting ice-shelf fronts) may have accelerated the disintegration of the Weddell Sea ice shelves and, ultimately, the WAIS.

Following the peak of the LIG around 119 ka BP, the Powell Basin sea-ice records reflect a cycle of sea ice advance and retreat throughout the remaining MIS 5 substages. WSIC strengthened and remained at ca. 80%, while spring/summer sea ice ($PIPSO_{25}$) experienced a substantial increase between MIS 5e and 5d (reaching PGM values at 5d), and remained elevated (> ca. 0.6) for the rest of the MIS (Fig. 4b and c). This expansion of sea ice into MIS 5d, and its persisting presence throughout the remaining MIS 5, is accompanied by a gradual decline in both sea surface and subsurface ocean temperatures, along with reduced primary production ~~(Fig. 4)~~. Likewise, an increasing WSIC, lowered SSST and primary productivity are also noted in the South Scotia Sea (Fig. 4d-h). However, being more northern~~n~~ly located, the South Scotia Sea experienced a lower and more varied WSIC (ca. 48 - 68%) and~~, with a distal~~minimum summer sea-ice cover~~edge~~ evident by a lower abundance of *F. obliquecostata* (<1%) than in the Powell Basin (Fig. 4d).

5.1.3 *Glacial period – Last Glacial Maximum – Termination I*

After MIS 5, Antarctica transited into the last glacial period (74-19 ka BP). In our Powell Basin records, this is reflected in~~reflects~~ a northward expansion of the sea-ice extent (peak $PIPSO_{25}$ values and 100% WSIC). Additionally, the lack of sea ice- and phytoplankton-related biomarkers and diatoms points towards an extremely suppressed production in the basin (Fig. 3a and b, ~~and~~ 4b and c). We postulate that at that time the basin was likely covered by permanent sea-ice cover or a floating ice shelf, which inhibited primary production in the underlying water column. The South Scotia Sea record (PS67/219-1) further to the north also points to~~presents~~ an overall higher winter and summer sea-ice cover, with elevated abundance of *F. obliquecostata* (0 - 3%) during this period suggesting a permanent sea-ice edge close to the core site (Xiao et al., 2016a). The oscillating patterns observed in both the sea-ice record and the biogenic opal content further point to alternating advance and retreat phases of the sea-ice edge in the South Scotia Sea (Fig. 4d and f; Allen et al., 2011).

In the Powell Basin, capped by an overlying (sea) ice cover throughout the glacial period, subsurface ocean temperatures somewhat resemble the millennial-scale variability in the EDML temperature profile (Fig. 4g). We presume that the subsurface temperature variations may possibly reflect changes in the ocean circulation in the Atlantic sector of the SO (Böhm et al., 2015; Williams et al., 2021). However, the age uncertainties and the low resolution of our subsurface ocean temperature record hamper~~is too low to make~~ an affirmative conclusion, and more data points will be required to ascertain corresponding oceanic variability.

The last glacial period culminated during the LGM between 26.5 and 19 ka BP with a most northwardly extending sea-ice edge, as identified in several marine sediment cores (Fig. 4b and c; Gersonde et al., 2005; Xiao et al., 2016a) and deduced from maximum $ssNa^+$ concentrations in the EDML ice core (Fig. 4a; Fischer et al., 2007a). Evidence from previous studies indicated the advance of grounded ice sheet and island ice caps to the edge of the outer continental shelf (Davies et al., 2012; Dickens et al., 2014). These grounded ice sheets were surrounded by floating ice shelves that extended seaward to 58°S on the western side of Antarctica (Herron and Anderson, 1990; Johnson and Andrews, 1986). In the Atlantic sector, the 60 - 70% expansion of WSI towards the modern Polar Front (~50°S; Gersonde et al., 2003) also promoted a northward shift of the summer sea-ice edge beyond core site PS67/219-1 to around 55°S (Allen et al., 2011; Collins et al., 2012), which lead to restricted primary productivity as reflected in the minimum biogenic opal content of core PS67/219-1 (Fig. 4f). The LGM is also considered the coldest interval, with a northward expansion of the (sub)Antarctic cold waters by 4 - 5° in latitude towards the subtropical warm waters (Gersonde and Zielinski, 2000; Gersonde et al., 2003). Sea-ice extent (Fig. 5.4) and SSST (Fig. 6.3) derived from our climate simulation during the peak of LGM (21 ka BP) align with these findings. This distinct growth of the (sea) ice-field in the SO, coupled with lower reconstructed and modeled LGM subsurface temperatures (Fig. 4g and 7.3), suggests an intensified cold-water stratification at our core sites, and a possible northward displacement of the WDW upwelling zone towards the edge of the summer sea-ice field~~. According to~~ (Ferrari et al., 2014)~~, during the LGM, the upwelling zone of the circumpolar deep water shifted further from the continental margin, nearing the edge of the summer sea-ice field. In this period, intensified AABW penetrated northward into the deep North Atlantic, causing the NADW to shoal above 2 km water depth (Curry and Oppo,~~

~~2005). This displacement of the NADW has a profound impact on heat distribution in deep-ocean circulation, as vertical mixing of the AABW and NADW – typically occurring below 2 km water depth in proximity to seamounts and midocean ridge – is prevented. Consequently, greater volume of cold AABW, rather than warm NADW, was recirculated back to the SO as circumpolar deep water (Ferrari et al., 2014; Watson et al., 2015).~~

TI began around 18 ka BP, when our records from Powell Basin indicate a transition from a perennial-ice cover to a dynamic sea-ice scenario (see Sect 4.5), with several cycles of advance and retreat. Similarly, the sea ice-related records from the South Scotia Sea (PS67/219-1) and the EDML $ssNa^+$ record depict a decrease in sea-ice cover, along with rapid increases in primary productivity and ocean temperature (Fig. 4). This deglaciation is attributed to a weakening AMOC circulation as a result of reduced NADW formation caused by increasing NH summer insolation and significant ice sheet melt at 18 ka BP, also known as Heinrich Stadial 1 (Clark et al., 2020; Denton et al., 2010; Waelbroeck et al., 2011). The gradual warming of TI was interrupted by a brief cooling between 14 and 12 ka BP. During this interval, our records reveal a short-term re-advancement in sea ice, coupled with a drop in productivity and temperature (Fig. 4). This event seems to coincide with multiple South Atlantic records (Xiao et al., 2016a) and higher $ssNa^+$ concentrations and a plateau in $\delta^{18}O$ values recorded in the EDML ice core (Fischer et al., 2007a). We hence propose~~believe~~ this event to be the Antarctic Cold Reversal (ACR), which is linked to the Bølling-Allerød warm interval in the NH via the bipolar seesaw mechanism (Pedro et al., 2011; 2016).

5.1.4 Holocene

Following the brief cooling of the ACR, the deglacial warming resumed its pace and Antarctica transited into the present interglacial (Holocene: 12 ka BP-present), which is marked by intervals of warming and cooling events (Bentley et al., 2009; Bianchi and Gersonde, 2004; Xiao et al., 2016a). Our data support these findings and document periods characterized by seasonal/dynamic and minimum sea-ice cover (see Sect 4.5) since 12 ka BP. We acknowledge that the age constraints and data availability of core PS118_63-1 for the Holocene is limited and exercise caution on the interpretation of the Holocene proxy records. Nevertheless, our data ~~but~~ still permit the discrimination of Holocene ~~different~~ warming and cooling trends~~cold intervals~~. ~~The first post-ACR warming is noted between 12 and 9 ka BP, while a possible second warming is observed between 8 and 5 ka BP.~~

The Powell Basin experienced an overall rapid decline in the winter and spring/summer sea-ice (Fig. 4b and c), concurrent with a rise in SSST (-0.5 to 0.5°C; Fig. 4h) and primary productivity between 12 and ~~5~~9 ka PB (Fig. 4e), suggesting a seasonal sea-ice cover. ~~In contrast, between 8 and 5 ka BP, our proxy data reveals~~The significant reduction in the abundance of the *F. curta* gp (below 3% ~~threshold~~), WSIC and spring/summer sea ice ($PIPSO_{25}$; Fig. 4b and c) culminates at ca. 5 ka BP and is accompanied by an~~. This, alongside a further~~ elevated primary productivity reflected in rising biogenic opal and TOC contents, which seems to~~signal, may~~ indicate a brief open-ocean setting for the Powell Basin during this warm interval~~ (Fig. 4)~~. We further note fluctuating SSSTs, while the subsurface ocean temperature remains relatively stable between 9 and 5 ka BP and the remainder of the Holocene (Fig. 4g and h). This somehow contrasts with a subtle decline in SSSTs recorded in core PS67/219-1 (Fig.

4i) inWhile at the South Scotia Sea, trace levels (<1%) of *F. obliquecostata* recorded in core PS67/219-1, coupled with a fluctuating WSI cover, centering around 50%, implies an open-ocean condition with occasional WSI in the region. Interestingly, a higher – though varying – SSST (0.6 to 2.0°C) and peak biogenic production is observed between 12 and 9 ka BP, while a less elevated SSST (0.5 to 1°C) and biogenic production is observed between 8 and 5 ka BP (Fig. 4f and i; Xiao et al., 2016a). The cooling and mild warming experienced in the South Scotia Sea between 9 and 5 ka BP probably indicate a northward export of increased glacial meltwater from the Weddell Sea (Powell Basin) – substantiated by the elevated presence of *Chaetoceros* rs recorded in core PS118_63-1 (Fig. 3e). We may attribute this cooling to a northward export of increased glacial meltwater. Our model simulation at 6 ka BP depicts a somewhat similar oceanic condition, with <40% spring/summer sea ice at the studied sites (Fig. 5.5a). However, in comparison with our proxy records, the model appears to have overestimated the WSI, SST and OT (Fig. 5.5b, 6.4 and 7.4). This overestimation may be attributed to the complex ice-ocean interactions and feedbacks alongof the Antarctic coastal region, which may not be fully represented in the model that has a spatial resolution in the order of tens of kilometers.

While the limited age constraints for the Holocene in core PS118_63-1, preclude us from further allocating short-term climate variations, we propose that the interval around 5 ka BP may reflect the Holocene climate optimum, while the upper part of the core depicts the later Holocene conditions. Here, increasing $PIPSO_{25}$ values and WSI reflect a re-expansion of seasonal sea ice still permitting primary productivity as derived from elevated biogenic opal and TOC contents (Fig. 4b, c and e). We propose that a distinct Holocene climate optimum occurred at each core site, as evident from our findings. For example, the South Scotia Sea witnessed the climate optimum from 12 to 9 ka BP (Xiao et al., 2016a), whereas the warmest interval (Holocene) in the Powell Basin occurred between 8 and 5 ka BP. Michalchuk et al. (2009) also established similar deglacial conditions for the northern Antarctic Peninsula – where the ice sheet/glacier retreated by 8.3 ka BP, followed by the mid-Holocene climate optimum between 8.3 and 6 ka BP. Moreover, tThe climate optimum experienced in the Powell Basin seems to correspond to the mid-Holocene climate optimum identified in sediment cores from the South Orkney Plateau between 8.2 and 4.8 ka BP and around Antarctica (Crosta et al., 2008; Denis et al., 2010; Kim et al., 2012; Lee et al., 2010; Taylor et al., 2001). However, reports of differing timings and mode for the mid-Holocene climate optimum around the Antarctic Peninsula have been noted in previous studies (Bentley et al., 2009; Davies et al., 2012; Shevenell et al., 1996; Taylor and Sjunneskog, 2002). Vorrath et al. (2023) determined the mid-Holocene climate optimum to have occurred between 8.2 and 4.2 ka BP, based on biomarker analyses of a sedimentmarine core from the eastern Bransfield Strait. They suggest that the climatic changes at their core site were influenced predominantly by the warm Antarctic Circumpolar Current rather than the cold-water Weddell Sea. This is contrary to a shorter climate optimum (6.8-5.9 ka BP) proposed by Heroy et al. (2008), where they examined the climate history of western Bransfield Strait using sediment and diatom analyses. Such diverse research outcomes highlight the complexity of responses to micro-region variations in glacial, atmospheric and oceanic changes in the Antarctic Peninsula throughout the Holocene (Bentley et al., 2009; Davies et al., 2012; Heroy et al., 2008; Vorrath et al., 2023).

5.2 Comparison between interglacials / transition periods

A comparison of the environmental changes caused by climate warming during TII and TI as well as the peak LIG and the Holocene, may yield valuable information on common or different driving and feedback mechanisms. As marine cores PS118_63-1 and PS67/219-1 provide continuous records of the environmental evolution in the northwestern Weddell Sea and South Scotia Sea, respectively, dating back to at least 145 ka BP, they offer a distinct opportunity to evaluate (sea-ice) conditions between the two terminations (TII and TI) and both warm periods (LIG and Holocene), particularly in proximity to the continental margin. Denton et al. (2010) studied the last four terminations and concluded that the terminations were triggered by a sequence of comparable events: maximum NH summer insolation that caused substantial NH ice sheet melting (due to marine ice sheet instability) over an extended (>5 kyrs) NH stadial interval. The huge release of meltwater slowed the AMOC, thus triggering an intense warming in the southern high-latitudes through the bipolar seesaw teleconnection, accompanied by a poleward shift in the southern westerlies. In line with this hypothesis, o~~O~~ur records from cores PS118_63-1 and PS67/219-1 portray a consistent and rapid decline in sea ice throughout both terminations (TII and TI). Interestingly, both deglaciations feature a short-term re~~-~~advance~~ment~~ of sea ice during their latest stage, at ca. 130 ka BP and during the ACR, respectively, likely due to meltwater-discharge from retreating ice shelves/ice sheets in the SO. This suggests that short-term sea ice growth stimulated by deglacial meltwater may be a common feature during glacial terminations. Despite commonalities in the sea-ice records, some differences are discernible. For instance, during TII, there is an abrupt surge in biogenic opal in the South Scotia Sea, along~~side~~ a consistent rise in TOC content within the Powell Basin~~, can be observed for TII~~. In contrast, TI exhibits a pattern characterized by a gradual increase with periodic fluctuations throughout the termination ~~saw-toothed pattern~~ for both TOC and biogenic opal content~~these proxies~~. Additionally, the South Scotia Sea (PS67/219-1) recorded a higher mean biogenic opal content and SSST across TII (35%; 0.7°C) than TI (26%; 0.5°C). Likewise, in the Powell Basin (PS118_63-1), higher mean TOC~~, SSST~~ and subsurface ocean temperature are perceived during TII (0.5%; ~~-0.3°C;~~ 0°C) than during TI (0.4%; ~~-0.5°C;~~ -0.3°C). ~~These variations likely reflect differing deglacial magnitudes experienced in the South Atlantic across the two terminations. For instance,~~ These data are in agreement with the EDML $\delta^{18}O$ record, which registered a stronger deglacial amplitude (32%) in TII than TI (Masson-Delmotte et al., 2011). Broecker and Henderson (1998) also speculated that the amplitude of the SH summer insolation during TII was higher than during TI. Additionally, a delay of approximately 10 kyrs between the SH and NH summer insolation (and subsequent NH ice sheet melting) during TII – as compared to TI's SH summer insolation peak just before the melting of the NH ice sheet – probably contributed to a more pronounced TII warming ~~than TI~~ in the SO. The differing magnitude of warming observed between both core sites in the South Atlantic, however, is likely attributed to their latitudinal differences.

The climate during the LIG appeared to be warmer than during the Holocene. In the Powell Basin, the LIG peak interval (i.e., MIS 5e) was characterized by a significantly reduced spring/summer sea-ice cover and peak productivity, while a higher spring/summer sea-ice cover, along with an only gradually increasing productivity are observed for the Holocene warm period (Fig. 4b and e). However, no significant difference in the WSIC between both interglacial was noted. The discrepancy in warming

intensity likely occurred seasonally and coincided with maximum summer insolation (see also Fig. 4 in Bova et al., 2021). Nonetheless, a lower mean annual regional insolation (-1.1 W/m^2 difference; Laskar et al., 2004) during the LIG does not explain the warmer conditions observed in the region. Bova et al. (2021) hypothesized that the LIG was relatively warmer than the Holocene as a result of its preceding deglacial dynamics: specifically, the magnitude of the last deglaciation was half that of the penultimate deglaciation – where a rapid and intense warming destabilized and significantly reduced the (sea) ice cover to near modern-day level by the onset of the LIG (Bova et al., 2021), and possibly a collapse of the WAIS in the first half of the LIG (Pollard and Deconto, 2009; Sutter et al., 2016). As such, we opine that the lower magnitude of warming during TI was a consequence of spatially and temporally varying retreats and advances in ~~(sea)~~ ice cover (including sea ice, ice shelves and glaciers) in the SO. The higher ice coverage throughout the Holocene resulted in a higher surface albedo and a cooler Holocene, as compared to the LIG. This is witnessed in our rather variable Holocene sea-ice proxy records (Fig. 4b and c) and differing reports of mid-Holocene warming and repeated fluctuations in environmental conditions around ~~the~~ Antarctica (see sect 5.1.4; Bentley et al., 2014; Davies et al., 2012; Ó Cofaigh et al., 2014).

5.3 Evaluating COSMOS performance: Addressing boundary conditions and model selection

With regard to COSMOS simulations, we note very similar sea-ice conditions being depicted for the peak interglacial 125 ka BP and 6 ka BP time slices (Fig 5.3 and 5.5), while subtle differences are resolved for SSTs and OTs (Fig. 6.2 and 6.4, 7.2 and 7.4, respectively). When considering the disparity observed in our proxy data between these two interglacial intervals, we infer that these similarities in the simulations likely result from using the same geographic boundary conditions for both time slices, while climate forcing data (e.g., greenhouse gases, orbital parameters) differ, of course. Our study aligns with the PMIP framework in maintaining a constant modern-day geography across each interglacial time slice, specifically the mid-Holocene (e.g., 6 ka BP) and the LIG (e.g., 128 and 125 ka BP). For the 6 ka BP time slice, this decision is supported by evidence indicating that ice sheets had reached their modern configuration (Otto-Bliesner et al., 2017). In the case of the LIG, the use of the modern ice-sheet configuration is primarily due to uncertainties in the LIG reconstructions (Otto-Bliesner et al., 2017). We acknowledge that the consideration of a single configuration throughout the LIG certainly is a simplification. However, it is also important to note that the changes in the Antarctic ice sheets' contribution to global mean sea level were small between 128 and 125 ka BP, compared to the remainder of the LIG (Barnett et al., 2023). Therefore, we propose that using a constant ice-sheet configuration for our LIG time slices is a reasonable approximation. Similarly, we estimated a constant ice-sheet setting for both the PGM and LGM time slices. While there are indications of different NH ice-sheet extents between the two glacial periods (Rohling et al., 2017), uncertainty remains regarding the exact distribution of ice on Antarctica. Understanding this distribution is crucial to determine whether different ice-sheet configurations should be considered for the boundary conditions of the respective glacial climate simulations. Given the varied trends observed in our proxy data for each glacial and interglacial periods, we propose that future studies should explore different plausible Antarctic ice-sheet

configurations and their effects on glacial-interglacial sea ice and oceanic conditions in the SO, particularly in the coastal regions.

In our modeling approach, we have relied exclusively on simulations from COSMOS rather than adopting a multi-model approach based on available PMIP simulations. This decision was motivated by the need to cover specific time slices pertinent to our study (see also Sect 3.5). To validate the reliability of our results, we conducted a comparison of COSMOS-simulated sea-ice cover and SST results against those from the PMIP3 and PMIP4 ensemble models. We refer to Supplement S3.4 for full detail. In general, the model-to-model comparison shows good agreement (<2σ threshold) between our COSMOS results and those from the PMIP3 ensemble – especially at our study locations, with some disagreement noted for the 21 ka BP time slice (Supplementary Fig. S4 and S5, S8 and S9). These deviations largely occur around the sea-ice edge and are primarily due to uncertainties generated within the PMIP3 ensemble itself. In contrast, our COSMOS-to-PMIP4 ensemble comparison shows greater disagreement. The COSMOS simulation shows a milder warm bias in the SO compared to various other PMIP3 models (Lunt et al., 2013), whereas CMIP6 models, which provide the foundation for PMIP4, are documented to have a warm bias in the SO (Luo et al., 2023). Beyond the difference in warm bias, the disagreements between COSMOS and PMIP4 may arise from several factors, including evolution of modeling protocols, boundary conditions, and model development from PMIP3 to PMIP4, with COSMOS remaining a PMIP3-class model. Based on the comparative outcomes, we demonstrate that our results align with PMIP in many relevant aspects, though this comparison is limited by the incomplete coverage of time slices within PMIP. Where our model shows disagreement with the PMIP3 ensemble, the uncertainty within the ensemble itself is quite large. This highlights that the uncertainty in simulated sea-ice conditions at our core locations, which we acknowledge as a limitation of using only one model in our study, is not necessarily mitigated by using an ensemble of models instead. Given that COSMOS is mostly within the 2σ threshold – defined as a measure for agreement with the PMIP3 ensemble – at the study sites, we would not expect to derive substantially different inferences if we relied on the PMIP3 ensemble instead. Although COSMOS has not undergone the updates that PMIP4 models received and has been exposed to boundary conditions only partly comparable to PMIP4 simulations, it remains one of the most extensively utilized models for reconstructing Quaternary climates and beyond to date. This enables our study's results to be considered within the much larger context of the Cenozoic climate. Despite these limitations, it is worth noting that COSMOS has been successfully employed alongside other PMIP4 models (Stepanek et al., 2020).

6 Summary and conclusions

Multiproxy analyses on marine sediment core PS118_63-1 from the Powell Basin provide new insights into the glacial-interglacial environmental variability in proximity to the Antarctic continental margin. With the use of the novel sea ice and open-water biomarkers and diatom assemblage data, alongside primary productivity proxies, we are able to reconstruct sea-ice conditions in the Powell Basin for the past ca. 145 kyrs. Our findings reveal year-round ice-cover with minimal productivity during glacial periods, while dynamic sea-ice conditions with varied productivity are recorded in the Powell

Basin during climate transitions and interglacial periods, such as the Holocene and MIS 5. Peak reduction in sea ice and near open ocean conditions are noted for MIS 5e. In contrast, no significant glacial-interglacial temperature variation was registered in the basin, which is attributed to~~in line with~~ the ~~generally~~ cold-water regime of the Weddell Sea. Comparison between the current and last interglacial, and their respective~~corresponding~~ climate transitions (TI and TII), suggests a relationship between deglacial amplitude and warming intensity during the corresponding interglacial: in general, an abrupt and intense (gradual and slow) deglaciation leads to a warmer (cooler) interglacial, with higher (lesser) ice-~~-~~sheet retreat (Bova et al., 2021). Our data presented in this study reinforce earlier paleo sea-ice reconstructions in the South Atlantic sector of the SO and provide new~~fresh~~ insights into the ice-proximal sea-ice response during varying climate conditions. Evaluation of both proxy and model data highlights similarities between sea-ice reconstruction and simulation. However, notable discrepancies remain, such as the differing proxy-model data~~are~~ observed for the Holocene compared to the LIG, and subsurface temperature profile for the LIG~~estimations~~. It is therefore pivotal to explore different Antarctic ice-sheet configurations in future studies, as well to expand on the~~se~~ paleoclimate data for the region.~~,~~ These will help to ~~further~~ close the gap in our understanding of ocean-ice-atmosphere interactions and dynamics and ultimately ~~towards~~ enhanc~~e~~ing climate model predictions closer to the Antarctic continental margins.

Data availability. Data mentioned in this article will be available on PANGAEA (Proxy records: address; COSMOS model output: address). For specific model output requests beyond the climate variables included in the PANGAEA data publication, please contact Christian Stepanek at christian.stepanek@awi.de. CMIP/PMIP data is available via the Earth System Grid Federation using one of their publicly available data portals (e.g., https://esgf-data.dkrz.de/search/cmip5-dkrz/ and https://esgf-data.dkrz.de/search/cmip6-dkrz/).

Code availability. Requests for the source code of the COSMOS climate model should be directed to the Max Planck Institute for Meteorology, Bundesstrasse 53, 20146 Hamburg, Germany.

Supplement. The supplement related to this article is available online at:

Author contributions. This study was conceived by WWK and JM. Data collection and interpretation was conducted by WWK, together with OE (diatom), JM (HBI), JH and GM (GDGT). WG produced the U/Th-dating data. CS and GL selected, documented, and post-processed the data from an ensemble of simulations that provided the climate model data for this study. Three of the six simulations presented here, namely *lig125k*, *lig128k*, and *pgm140k*, represent previously unpublished climate model output created by PG. WX supplied unpublished data for PS67/219-1. WWK wrote the paper and created the visualizations, supported by CS who visualized model output and interpolated climate model output to core locations. JM supervised the study. All authors contributed to the analyses, discussion of the results, and the conclusion of this study.

Competing interests. The authors declare that they have no conflict of interest.

Acknowledgements. We thank the captain, crew and science team of the RV Polarstern cruise PS118 (Grant No. AWI_PS118_04). Special thanks go to Michael Schreck, Nele Steinberg, Sabine Hanisch and Frank Niessen for PS118 marine geology operations. Appreciation is also extended to Denise Diekstall (HBI), Mandy Kuck (HBI), Ulrike Böttjer (Biogenic Opal) for their support. Simon Belt is acknowledged for providing the 7-HND internal standard for HBI quantification. This research is funded through the Alfred Wegener Institute Helmholtz Centre for Polar and Marine Research (International Science Program for Integrative Research in Earth Systems, INSPIRES II). Gerrit Lohmann, Paul Gierz, and Christian Stepanek are funded through the Alfred Wegener Institute's research program: Changing Earth - Sustaining our Future of the Helmholtz Association. Christian Stepanek also acknowledges funding from the Helmholtz Climate Initiative REKLIM. We acknowledge the World Climate Research Programme's Working Group on Coupled Modeling for CMIP, and the Paleoclimate Model Intercomparison Project and its working groups for coordinating the model intercomparison in PMIP3 and PMIP4. Appreciation is extended to the climate modeling groups (listed in Table S4) for their contribution and availability of model output to CMIP5/6 and PMIP3/4. The U.S. Department of Energy's Program for Climate Model Diagnosis and Intercomparison is recognized for providing coordinating support and leading software infrastructure development with the Global Organization for Earth System Science Portals. The Earth System Grid Federation is also acknowledged for preserving and providing CMIP and PMIP model output. We are also appreciative of the support from the Alfred Wegener Institute's Open Access Publication Funds. Lastly, we thank the editor, Dr. Alberto Reyes, Dr. Xavier Crosta and an anonymous reviewer for their constructive comments that helped to improve the paper.

References

Abe-Ouchi, A., Saito, F., Kageyama, M., Braconnot, P., Harrison, S. P., Lambeck, K., Otto-Bliesner, B. L., Peltier, W. R., Tarasov, L., Peterschmitt, J. Y., and Takahashi, K.: Ice-sheet configuration in the CMIP5/PMIP3 Last Glacial Maximum experiments, Geosci. Model Dev., 8, 3621-3637, https://doi.org/10.5194/gmd-8-3621-2015, 2015.

Abernathey, R. P., Cerovecki, I., Holland, P. R., Newsom, E., Mazloff, M., and Talley, L. D.: Water-mass transformation by sea ice in the upper branch of the Southern Ocean overturning, Nature Geoscience, 9, 596-601, https://doi.org/10.1038/ngeo2749, 2016.

Abram, N. J., Wolff, E. W., and Curran, M. A. J.: A review of sea ice proxy information from polar ice cores, Quaternary Science Reviews, 79, 168-183, https://doi.org/10.1016/j.quascirev.2013.01.011, 2013.

Allen, C. S., Pike, J., and Pudsey, C. J.: Last glacial–interglacial sea-ice cover in the SW Atlantic and its potential role in global deglaciation, Quaternary Science Reviews, 30, 2446-2458, https://doi.org/10.1016/j.quascirev.2011.04.002, 2011.

Argus, D. F. and Peltier, W. R.: Constraining models of postglacial rebound using space geodesy: a detailed assessment of model ICE-5G (VM2) and its relatives, Geophysical Journal International, 181, 697-723, https://doi.org/10.1111/j.1365-246X.2010.04562.x, 2010.

Ashley, K. E., McKay, R., Etourneau, J., Jimenez-Espejo, F. J., Condron, A., Albot, A., Crosta, X., Riesselman, C., Seki, O., Massé, G., Golledge, N. R., Gasson, E., Lowry, D. P., Barrand, N. E., Johnson, K., Bertler, N., Escutia, C., Dunbar, R., and Bendle, J. A.: Mid-Holocene Antarctic sea-ice increase driven by marine ice sheet retreat, Clim. Past, 17, 1-19, https://doi.org/10.5194/cp-17-1-2021, 2021.

Bakker, P., Masson-Delmotte, V., Martrat, B., Charbit, S., Renssen, H., Gröger, M., Krebs-Kanzow, U., Lohmann, G., Lunt, D. J., Pfeiffer, M., Phipps, S. J., Prange, M., Ritz, S. P., Schulz, M., Stenni, B., Stone, E. J., and Varma, V.: Temperature trends during the Present and Last Interglacial periods – a multi-model-data comparison, Quaternary Science Reviews, 99, 224-243, https://doi.org/10.1016/j.quascirev.2014.06.031, 2014.

Barbara, L., Crosta, X., Schmidt, S., and Massé, G.: Diatoms and biomarkers evidence for major changes in sea ice conditions prior the instrumental period in Antarctic Peninsula, Quaternary Science Reviews, 79, 99-110, https://doi.org/10.1016/j.quascirev.2013.07.021, 2013.

Barbara, L., Crosta, X., Leventer, A., Schmidt, S., Etourneau, J., Domack, E., and Massé, G.: Environmental responses of the Northeast Antarctic Peninsula to the Holocene climate variability, Paleoceanography, 31, 131-147, https://doi.org/10.1002/2015PA002785, 2016.

Barnett, R. L., Austermann, J., Dyer, B., Telfer, M. W., Barlow, N. L. M., Boulton, S. J., Carr, A. S., and Creel, R. C.: Constraining the contribution of the Antarctic Ice Sheet to Last Interglacial sea level, Science Advances, 9, eadf0198, https://doi.org/10.1126/sciadv.adf0198, 2023.

Belt, S. T.: Source-specific biomarkers as proxies for Arctic and Antarctic sea ice, Organic Geochemistry, 125, 277-298, https://doi.org/10.1016/j.orggeochem.2018.10.002, 2018.

Belt, S. T. and Müller, J.: The Arctic sea ice biomarker IP25: a review of current understanding, recommendations for future research and applications in palaeo sea ice reconstructions, Quaternary Science Reviews, 79, 9-25, https://doi.org/10.1016/j.quascirev.2012.12.001, 2013.

Belt, S. T., Allard, W. G., Massé, G., Robert, J.-M., and Rowland, S. J.: Highly branched isoprenoids (HBIs): identification of the most common and abundant sedimentary isomers, Geochimica et Cosmochimica Acta, 64, 3839-3851, https://doi.org/10.1016/S0016-7037(00)00464-6, 2000.

Belt, S. T., Brown, T. A., Rodriguez, A. N., Sanz, P. C., Tonkin, A., and Ingle, R.: A reproducible method for the extraction, identification and quantification of the Arctic sea ice proxy IP25 from marine sediments, Analytical Methods, 4, 705-713, https://doi.org/10.1039/C2AY05728J, 2012.

Belt, S. T., Smik, L., Brown, T. A., Kim, J. H., Rowland, S. J., Allen, C. S., Gal, J. K., Shin, K. H., Lee, J. I., and Taylor, K. W. R.: Source identification and distribution reveals the potential of the geochemical Antarctic sea ice proxy IPSO25, Nature Communications, 7, 12655, https://doi.org/10.1038/ncomms12655, 2016.

Bentley, M. J., Hodgson, D. A., Smith, J. A., Cofaigh, C. Ó., Domack, E. W., Larter, R. D., Roberts, S. J., Brachfeld, S., Leventer, A., Hjort, C., Hillenbrand, C.-D., and Evans, J.: Mechanisms of Holocene palaeoenvironmental change in the Antarctic Peninsula region, The Holocene, 19, 51-69, https://doi.org/10.1177/0959683608096603, 2009.

Bentley, M. J., Ó Cofaigh, C., Anderson, J. B., Conway, H., Davies, B., Graham, A. G. C., Hillenbrand, C.-D., Hodgson, D. A., Jamieson, S. S. R., Larter, R. D., Mackintosh, A., Smith, J. A., Verleyen, E., Ackert, R. P., Bart, P. J., Berg, S., Brunstein, D., Canals, M., Colhoun, E. A., Crosta, X., Dickens, W. A., Domack, E., Dowdeswell, J. A., Dunbar, R., Ehrmann, W., Evans, J., Favier, V., Fink, D., Fogwill, C. J., Glasser, N. F., Gohl, K., Golledge, N. R., Goodwin, I., Gore, D. B., Greenwood, S. L., Hall, B. L., Hall, K., Hedding, D. W., Hein, A. S., Hocking, E. P., Jakobsson, M., Johnson, J. S., Jomelli, V., Jones, R. S., Klages, J. P., Kristoffersen, Y., Kuhn, G., Leventer, A., Licht, K., Lilly, K., Lindow, J., Livingstone, S. J., Massé, G., McGlone, M. S., McKay, R. M., Melles, M., Miura, H., Mulvaney, R., Nel, W., Nitsche, F. O., O'Brien, P. E., Post, A. L., Roberts, S. J., Saunders, K. M., Selkirk, P. M., Simms, A. R., Spiegel, C., Stolldorf, T. D., Sugden, D. E., van der Putten, N., van Ommen, T., Verfaillie, D., Vyverman, W., Wagner, B., White, D. A., Witus, A. E., and Zwartz, D.: A community-based geological reconstruction

of Antarctic Ice Sheet deglaciation since the Last Glacial Maximum, Quaternary Science Reviews, 100, 1-9, https://doi.org/10.1016/j.quascirev.2014.06.025, 2014.

Bianchi, C. and Gersonde, R.: The Southern Ocean surface between Marine Isotope Stages 6 and 5d: Shape and timing of climate changes, Palaeogeography, Palaeoclimatology, Palaeoecology, 187, 151-177, https://doi.org/10.1016/S0031-0182(02)00516-3, 2002.

Bianchi, C. and Gersonde, R.: Climate evolution at the last deglaciation: the role of the Southern Ocean, Earth and Planetary Science Letters, 228, 407-424, https://doi.org/10.1016/j.epsl.2004.10.003, 2004.

Böhm, E., Lippold, J., Gutjahr, M., Frank, M., Blaser, P., Antz, B., Fohlmeister, J., Frank, N., Andersen, M. B., and Deininger, M.: Strong and deep Atlantic meridional overturning circulation during the last glacial cycle, Nature, 517, 73-76, https://doi.org/10.1038/nature14059, 2015.

Bova, S., Rosenthal, Y., Liu, Z., Godad, S. P., and Yan, M.: Seasonal origin of the thermal maxima at the Holocene and the last interglacial, Nature, 589, 548-553, https://doi.org/10.1038/s41586-020-03155-x, 2021.

Braconnot, P., Harrison, S. P., Kageyama, M., Bartlein, P. J., Masson-Delmotte, V., Abe-Ouchi, A., Otto-Bliesner, B., and Zhao, Y.: Evaluation of climate models using palaeoclimatic data, Nature Climate Change, 2, 417-424, https://doi.org/10.1038/nclimate1456, 2012.

Broecker, W. S. and Henderson, G. M.: The sequence of events surrounding Termination II and their implications for the cause of glacial-interglacial CO2 changes, Paleoceanography, 13, 352-364, https://doi.org/10.1029/98PA00920, 1998.

Brovkin, V., Raddatz, T., Reick, C. H., Claussen, M., and Gayler, V.: Global biogeophysical interactions between forest and climate, Geophysical Research Letters, 36, https://doi.org/10.1029/2009GL037543, 2009.

Carmack, E. C. and Foster, T. D.: On the flow of water out of the Weddell Sea, Deep Sea Research and Oceanographic Abstracts, 22, 711-724, https://doi.org/10.1016/0011-7471(75)90077-7, 1975.

Chadwick, M., Allen, C. S., Sime, L. C., and Hillenbrand, C. D.: Analysing the timing of peak warming and minimum winter sea-ice extent in the Southern Ocean during MIS 5e, Quaternary Science Reviews, 229, 106134, https://doi.org/10.1016/j.quascirev.2019.106134, 2020.

Chadwick, M., Allen, C. S., Sime, L. C., Crosta, X., and Hillenbrand, C. D.: Reconstructing Antarctic winter sea-ice extent during Marine Isotope Stage 5e, Clim. Past, 18, 129-146, https://doi.org/10.5194/cp-18-129-2022, 2022.

Chadwick, M., Jones, J., Lawler, K.-A., Prebble, J., Kohfeld, K. E., and Crosta, X.: Understanding glacial-interglacial changes in Southern Ocean sea ice, Past Global Changes Magazine, 27(2), 86, https://doi.org/10.22498/pages.27.2.86, 2019.

Clark, P. U., He, F., Golledge, N. R., Mitrovica, J. X., Dutton, A., Hoffman, J. S., and Dendy, S.: Oceanic forcing of penultimate deglacial and last interglacial sea-level rise, Nature, 577, 660-664, https://doi.org/10.1038/s41586-020-1931-7, 2020.

Collins, L. G., Pike, J., Allen, C. S., and Hodgson, D. A.: High-resolution reconstruction of southwest Atlantic sea-ice and its role in the carbon cycle during marine isotope stages 3 and 2, Paleoceanography, 27, https://doi.org/10.1029/2011PA002264, 2012.

Collins, L. G., Allen, C. S., Pike, J., Hodgson, D. A., Weckström, K., and Massé, G.: Evaluating highly branched isoprenoid (HBI) biomarkers as a novel Antarctic sea-ice proxy in deep ocean glacial age sediments, Quaternary Science Reviews, 79, 87-98, https://doi.org/10.1016/j.quascirev.2013.02.004, 2013.

Coren, F., Ceccone, G., Lodolo, E., Zanolla, C., Zitellini, N., Bonazzi, C., and Centonze, J.: Morphology, seismic structure and tectonic development of the Powell Basin, Antarctica, Journal of the Geological Society, 154, 849-862, https://doi.org/10.1144/gsjgs.154.5.0849, 1997.

Cortese, G. and Abelmann, A.: Radiolarian-based paleotemperatures during the last 160 kyr at ODP Site 1089 (Southern Ocean, Atlantic Sector), Palaeogeography, Palaeoclimatology, Palaeoecology, 182, 259-286, https://doi.org/10.1016/S0031-0182(01)00499-0, 2002.

Crosta, X., Denis, D., and Ther, O.: Sea ice seasonality during the Holocene, Adélie Land, East Antarctica, Marine Micropaleontology, 66, 222-232, https://doi.org/10.1016/j.marmicro.2007.10.001, 2008.

Crosta, X., Pichon, J.-J., and Labracherie, M.: Distribution of Chaetoceros resting spores in modern peri-Antarctic sediments, Marine Micropaleontology, 29, 283-299, https://doi.org/10.1016/S0377-8398(96)00033-3, 1997.

Crosta, X., Kohfeld, K. E., Bostock, H. C., Chadwick, M., Du Vivier, A., Esper, O., Etourneau, J., Jones, J., Leventer, A., Müller, J., Rhodes, R. H., Allen, C. S., Ghadi, P., Lamping, N., Lange, C. B., Lawler, K. A., Lund, D., Marzocchi, A., Meissner, K. J., Menviel, L., Nair, A., Patterson, M., Pike, J., Prebble, J. G., Riesselman, C., Sadatzki, H., Sime, L. C., Shukla, S. K., Thöle, L., Vorrath, M. E., Xiao, W., and Yang, J.: Antarctic sea ice over the past 130,000 years – Part 1: a review of what proxy records tell us, Clim. Past, 18, 1729-1756, https://doi.org/10.5194/cp-18-1729-2022, 2022.

Curry, W. B. and Oppo, D. W.: Glacial water mass geometry and the distribution of δ13C of ΣCO2 in the western Atlantic Ocean, Paleoceanography, 20, https://doi.org/10.1029/2004PA001021, 2005.

Dallmeyer, A., Claussen, M., Wang, Y., and Herzschuh, U.: Spatial variability of Holocene changes in the annual precipitation pattern: a model-data synthesis for the Asian monsoon region, Climate Dynamics, 40, 2919-2936, https://doi.org/10.1007/s00382-012-1550-6, 2013.

Dallmeyer, A., Claussen, M., Fischer, N., Haberkorn, K., Wagner, S., Pfeiffer, M., Jin, L., Khon, V., Wang, Y., and Herzschuh, U.: The evolution of sub-monsoon systems in the Afro-Asian monsoon region during the Holocene– comparison of different transient climate model simulations, Clim. Past, 11, 305-326, https://doi.org/10.5194/cp-11-305-2015, 2015.

Davies, B. J., Hambrey, M. J., Smellie, J. L., Carrivick, J. L., and Glasser, N. F.: Antarctic Peninsula Ice Sheet evolution during the Cenozoic Era, Quaternary Science Reviews, 31, 30-66, https://doi.org/10.1016/j.quascirev.2011.10.012, 2012.

de Vernal, A., Gersonde, R., Goosse, H., Seidenkrantz, M.-S., and Wolff, E. W.: Sea ice in the paleoclimate system: the challenge of reconstructing sea ice from proxies – an introduction, Quaternary Science Reviews, 79, 1-8, https://doi.org/10.1016/j.quascirev.2013.08.009, 2013.

Deacon, G.: The hydrography of the southern ocean, Discovery Rep, 15, 1-124, 1937.

DeConto, R. M. and Pollard, D.: Contribution of Antarctica to past and future sea-level rise, Nature, 531, 591-597, https://doi.org/10.1038/nature17145, 2016.

Denis, D., Crosta, X., Barbara, L., Massé, G., Renssen, H., Ther, O., and Giraudeau, J.: Sea ice and wind variability during the Holocene in East Antarctica: insight on middle–high latitude coupling, Quaternary Science Reviews, 29, 3709-3719, https://doi.org/10.1016/j.quascirev.2010.08.007, 2010.

Denton, G. H., Anderson, R. F., Toggweiler, J. R., Edwards, R. L., Schaefer, J. M., and Putnam, A. E.: The Last Glacial Termination, Science, 328, 1652-1656, https://doi.org/10.1126/science.1184119, 2010.

Dickens, W. A., Graham, A. G. C., Smith, J. A., Dowdeswell, J. A., Larter, R. D., Hillenbrand, C.-D., Trathan, P. N., Erik Arndt, J., and Kuhn, G.: A new bathymetric compilation for the South Orkney Islands region, Antarctic Peninsula (49°–39°W to 64°–59°S): Insights into the glacial development of the

continental shelf, Geochemistry, Geophysics, Geosystems, 15, 2494-2514, https://doi.org/10.1002/2014GC005323, 2014.

Dieckmann, G. S. and Hellmer, H. H.: The importance of sea ice: an overview, in: Sea ice, edited by: Dieckmann, G. S., and Hellmer, H. H., Blackwell Science Ltd, 1-22, 2010.

Dorschel, B.: The Expedition PS118 of the Research Vessel POLARSTERN to the Weddell Sea in 2019, Alfred Wegener Institute for Polar and Marine Research, Bremerhaven, https://doi.org/10.2312/BzPM_0735_2019, 2019.

Eayrs, C., Holland, D., Francis, D., Wagner, T., Kumar, R., and Li, X.: Understanding the Seasonal Cycle of Antarctic Sea Ice Extent in the Context of Longer-Term Variability, Reviews of Geophysics, 57, 1037-1064, https://doi.org/10.1029/2018RG000631, 2019.

Ebert, E. E., Schramm, J. L., and Curry, J. A.: Disposition of solar radiation in sea ice and the upper ocean, Journal of Geophysical Research: Oceans, 100, 15965-15975, https://doi.org/10.1029/95JC01672, 1995.

Elling, F. J., Könneke, M., Mußmann, M., Greve, A., and Hinrichs, K.-U.: Influence of temperature, pH, and salinity on membrane lipid composition and TEX86 of marine planktonic thaumarchaeal isolates, Geochimica et Cosmochimica Acta, 171, 238-255, https://doi.org/10.1016/j.gca.2015.09.004, 2015.

Elling, F. J., Könneke, M., Lipp, J. S., Becker, K. W., Gagen, E. J., and Hinrichs, K.-U.: Effects of growth phase on the membrane lipid composition of the thaumarchaeon Nitrosopumilus maritimus and their implications for archaeal lipid distributions in the marine environment, Geochimica et Cosmochimica Acta, 141, 579-597, https://doi.org/10.1016/j.gca.2014.07.005, 2014.

EPICA Community Members: One-to-one coupling of glacial climate variability in Greenland and Antarctica, Nature, 444, 195-198, https://doi.org/10.1038/nature05301, 2006.

EPICA Community Members: Stable oxygen isotopes of ice core EDML, PANGAEA [dataset], https://doi.org/10.1594/PANGAEA.754444, 2010.

Esper, O. and Gersonde, R.: Quaternary surface water temperature estimations: New diatom transfer functions for the Southern Ocean, Palaeogeography, Palaeoclimatology, Palaeoecology, 414, 1-19, https://doi.org/10.1016/j.palaeo.2014.08.008, 2014a.

Esper, O. and Gersonde, R.: New tools for the reconstruction of Pleistocene Antarctic sea ice, Palaeogeography, Palaeoclimatology, Palaeoecology, 399, 260-283, https://doi.org/10.1016/j.palaeo.2014.01.019, 2014b.

Etourneau, J., Collins, L. G., Willmott, V., Kim, J. H., Barbara, L., Leventer, A., Schouten, S., Sinninghe Damsté, J. S., Bianchini, A., Klein, V., Crosta, X., and Massé, G.: Holocene climate variations in the western Antarctic Peninsula: evidence for sea ice extent predominantly controlled by changes in insolation and ENSO variability, Clim. Past, 9, 1431-1446, https://doi.org/10.5194/cp-9-1431-2013, 2013.

Fahrbach, E., Rohardt, G., and Krause, G.: The Antarctic coastal current in the southeastern Weddell Sea, Polar Biology, 12, 171-182, https://doi.org/10.1007/BF00238257, 1992.

Fedotova, A. A. and Stepanova, S. V.: Water Mass Transformation in the Powell Basin, in: Antarctic Peninsula Region of the Southern Ocean: Oceanography and Ecology, edited by: Morozov, E. G., Flint, M. V., and Spiridonov, V. A., Springer International Publishing, Cham, 115-129, https://doi.org/10.1007/978-3-030-78927-5_8, 2021.

Ferrari, R., Jansen, M. F., Adkins, J. F., Burke, A., Stewart, A. L., and Thompson, A. F.: Antarctic sea ice control on ocean circulation in present and glacial climates, Proceedings of the National Academy of Sciences, 111, 8753-8758, https://doi.org/10.1073/pnas.1323922111, 2014.

Fietz, S., Ho, S. L., and Huguet, C.: Archaeal Membrane Lipid-Based Paleothermometry for Applications in Polar Oceans, Oceanography, 33, 104-114, https://www.jstor.org/stable/26937748, 2020.

Fischer, H., Fundel, F., Ruth, U., Twarloh, B., Wegner, A., Udisti, R., Becagli, S., Castellano, E., Morganti, A., Severi, M., Wolff, E., Littot, G., Röthlisberger, R., Mulvaney, R., Hutterli, M. A., Kaufmann, P., Federer, U., Lambert, F., Bigler, M., Hansson, M., Jonsell, U., de Angelis, M., Boutron, C., Siggaard-Andersen, M.-L., Steffensen, J. P., Barbante, C., Gaspari, V., Gabrielli, P., and Wagenbach, D.: Reconstruction of millennial changes in dust emission, transport and regional sea ice coverage using the deep EPICA ice cores from the Atlantic and Indian Ocean sector of Antarctica, Earth and Planetary Science Letters, 260, 340-354, https://doi.org/10.1016/j.epsl.2007.06.014, 2007a.

Fischer, H., Fundel, F., Ruth, U., Twarloh, B., Wegner, A., Udisti, R., Becagli, S., Castellano, E., Morganti, A., Severi, M., Wolff, E. W., Littot, G. C., Röthlisberger, R., Mulvaney, R., Hutterli, M. A., Kaufmann, P. R., Federer, U., Lambert, F., Bigler, C., Hansson, M. E., Jonsell, U., de Angelis, M., Boutron, C. F., Siggaard-Andersen, M.-L., Steffensen, J. P., Barbante, C., Gaspari, V., Gabrielli, P., and Wagenbach, D.: EPICA EDML chemical concentrations and fluxes, PANGAEA [dataset], https://doi.org/10.1594/PANGAEA.683642, 2007b.

Geibert, W., Stimac, I., Rutgers Van Der Loeff, M., and Kuhn, G.: Dating Deep-Sea Sediments With 230Th Excess Using a Constant Rate of Supply Model, Paleoceanography and Paleoclimatology, 34, 1895-1912, https://doi.org/10.1029/2019PA003663, 2019.

Gersonde, R. and Zielinski, U.: The reconstruction of late Quaternary Antarctic sea-ice distribution—the use of diatoms as a proxy for sea-ice, Palaeogeography, Palaeoclimatology, Palaeoecology, 162, 263-286, https://doi.org/10.1016/S0031-0182(00)00131-0, 2000.

Gersonde, R., Crosta, X., Abelmann, A., and Armand, L.: Sea-surface temperature and sea ice distribution of the Southern Ocean at the EPILOG Last Glacial Maximum—a circum-Antarctic view based on siliceous microfossil records, Quaternary Science Reviews, 24, 869-896, https://doi.org/10.1016/j.quascirev.2004.07.015, 2005.

Gersonde, R., Abelmann, A., Brathauer, U., Becquey, S., Bianchi, C., Cortese, G., Grobe, H., Kuhn, G., Niebler, H.-S., Segl, M., Sieger, R., Zielinski, U., and Fütterer, D. K.: Last glacial sea surface temperatures and sea-ice extent in the Southern Ocean (Atlantic-Indian sector): A multiproxy approach, Paleoceanography, 18, https://doi.org/10.1029/2002PA000809, 2003.

Goelzer, H., Huybrechts, P., Loutre, M. F., and Fichefet, T.: Last Interglacial climate and sea-level evolution from a coupled ice sheet–climate model, Clim. Past, 12, 2195-2213, https://doi.org/10.5194/cp-12-2195-2016, 2016.

Gordon, A. L., Visbeck, M., and Huber, B.: Export of Weddell Sea deep and bottom water, Journal of Geophysical Research: Oceans, 106, 9005-9017, https://doi.org/10.1029/2000JC000281, 2001.

Greene, C. A., Young, D. A., Gwyther, D. E., Galton-Fenzi, B. K., and Blankenship, D. D.: Seasonal dynamics of Totten Ice Shelf controlled by sea ice buttressing, The Cryosphere, 12, 2869-2882, https://doi.org/10.5194/tc-12-2869-2018, 2018.

Guagnin, M., Jennings, R., Eager, H., Parton, A., Stimpson, C., Stepanek, C., Pfeiffer, M., Groucutt, H. S., Drake, N. A., Alsharekh, A., and Petraglia, M. D.: Rock art imagery as a proxy for Holocene environmental change: A view from Shuwaymis, NW Saudi Arabia, The Holocene, 26, 1822-1834, https://doi.org/10.1177/0959683616645949, 2016.

Hagemann, J. R., Lembke-Jene, L., Lamy, F., Vorrath, M. E., Kaiser, J., Müller, J., Arz, H. W., Hefter, J., Jaeschke, A., Ruggieri, N., and Tiedemann, R.: Upper-ocean temperature characteristics in the subantarctic southeastern Pacific based on biomarker reconstructions, Clim. Past, 19, 1825-1845, https://doi.org/10.5194/cp-19-1825-2023, 2023.

Hayes, C. T., Martínez-García, A., Hasenfratz, A. P., Jaccard, S. L., Hodell, D. A., Sigman, D. M., Haug, G. H., and Anderson, R. F.: A stagnation event in the deep South Atlantic during the last interglacial period, Science, 346, 1514-1517, https://doi.org/10.1126/science.1256620, 2014.

Haywood, A. M., Hill, D. J., Dolan, A. M., Otto-Bliesner, B. L., Bragg, F., Chan, W. L., Chandler, M. A., Contoux, C., Dowsett, H. J., Jost, A., Kamae, Y., Lohmann, G., Lunt, D. J., Abe-Ouchi, A., Pickering, S. J., Ramstein, G., Rosenbloom, N. A., Salzmann, U., Sohl, L., Stepanek, C., Ueda, H., Yan, Q., and Zhang, Z.: Large-scale features of Pliocene climate: results from the Pliocene Model Intercomparison Project, Clim. Past, 9, 191-209, https://doi.org/10.5194/cp-9-191-2013, 2013.

Hellmer, H. H.: Impact of Antarctic ice shelf basal melting on sea ice and deep ocean properties, Geophysical Research Letters, 31, https://doi.org/10.1029/2004GL019506, 2004.

Heroy, D. C., Sjunneskog, C., and Anderson, J. B.: Holocene climate change in the Bransfield Basin, Antarctic Peninsula: evidence from sediment and diatom analysis, Antarctic Science, 20, 69-87, https://doi.org/10.1017/S0954102007000788, 2008.

Herron, M. J. and Anderson, J. B.: Late quaternary glacial history of the South Orkney Plateau, Antarctica, Quaternary Research, 33, 265-275, https://doi.org/10.1016/0033-5894(90)90055-P, 1990.

Hibler, W. D.: A Dynamic Thermodynamic Sea Ice Model, Journal of Physical Oceanography, 9, 815-846, https://doi.org/10.1175/1520-0485(1979)009<0815:ADTSIM>2.0.CO;2, 1979.

Hoffman, J. S., Clark, P. U., Parnell, A. C., and He, F.: Regional and global sea-surface temperatures during the last interglaciation, Science, 355, 276-279, https://doi.org/10.1126/science.aai8464, 2017.

Holloway, M. D., Sime, L. C., Singarayer, J. S., Tindall, J. C., Bunch, P., and Valdes, P. J.: Antarctic last interglacial isotope peak in response to sea ice retreat not ice-sheet collapse, Nature Communications, 7, 12293, https://doi.org/10.1038/ncomms12293, 2016.

Holloway, M. D., Sime, L. C., Allen, C. S., Hillenbrand, C. D., Bunch, P., Wolff, E., and Valdes, P. J.: The spatial structure of the 128 ka Antarctic sea ice minimum, Geophysical Research Letters, 44, 11,129-111,139, https://doi.org/10.1002/2017GL074594, 2017.

Hopmans, E. C., Weijers, J. W. H., Schefuß, E., Herfort, L., Sinninghe Damsté, J. S., and Schouten, S.: A novel proxy for terrestrial organic matter in sediments based on branched and isoprenoid tetraether lipids, Earth and Planetary Science Letters, 224, 107-116, https://doi.org/10.1016/j.epsl.2004.05.012, 2004.

Huhn, O., Hellmer, H. H., Rhein, M., Rodehacke, C., Roether, W., Schodlok, M. P., and Schröder, M.: Evidence of deep- and bottom-water formation in the western Weddell Sea, Deep Sea Research Part II: Topical Studies in Oceanography, 55, 1098-1116, https://doi.org/10.1016/j.dsr2.2007.12.015, 2008.

Inglis, G. N., Farnsworth, A., Lunt, D., Foster, G. L., Hollis, C. J., Pagani, M., Jardine, P. E., Pearson, P. N., Markwick, P., Galsworthy, A. M. J., Raynham, L., Taylor, K. W. R., and Pancost, R. D.: Descent toward the Icehouse: Eocene sea surface cooling inferred from GDGT distributions, Paleoceanography, 30, 1000-1020, https://doi.org/10.1002/2014PA002723, 2015.

Jacobs, S. S.: On the nature and significance of the Antarctic Slope Front, Marine Chemistry, 35, 9-24, https://doi.org/10.1016/S0304-4203(09)90005-6, 1991.

Jennings, R. P., Singarayer, J., Stone, E. J., Krebs-Kanzow, U., Khon, V., Nisancioglu, K. H., Pfeiffer, M., Zhang, X., Parker, A., Parton, A., Groucutt, H. S., White, T. S., Drake, N. A., and Petraglia, M. D.: The greening of Arabia: Multiple opportunities for human occupation of the Arabian Peninsula during the Late Pleistocene inferred from an ensemble of climate model simulations, Quaternary International, 382, 181-199, https://doi.org/10.1016/j.quaint.2015.01.006, 2015.

Johnson, R. G. and Andrews, J. T.: Glacial terminations in the oxygen isotope record of deep sea cores: hypothesis of massive Antarctic ice-shelf destruction, Palaeogeography, Palaeoclimatology, Palaeoecology, 53, 107-138, https://doi.org/10.1016/0031-0182(86)90041-6, 1986.

Jungclaus, J. H., Keenlyside, N., Botzet, M., Haak, H., Luo, J.-J., Latif, M., Marotzke, J., Mikolajewicz, U., and Roeckner, E.: Ocean Circulation and Tropical Variability in the Coupled Model ECHAM5/MPI-OM, Journal of Climate, 19, 3952-3972, https://doi.org/10.1175/JCLI3827.1, 2006.

Kim, J.-H., Crosta, X., Willmott, V., Renssen, H., Bonnin, J., Helmke, P., Schouten, S., and Sinninghe Damsté, J. S.: Holocene subsurface temperature variability in the eastern Antarctic continental margin, Geophysical Research Letters, 39, https://doi.org/10.1029/2012GL051157, 2012.

Kim, J.-H., van der Meer, J., Schouten, S., Helmke, P., Willmott, V., Sangiorgi, F., Koç, N., Hopmans, E. C., and Damsté, J. S. S.: New indices and calibrations derived from the distribution of crenarchaeal isoprenoid tetraether lipids: Implications for past sea surface temperature reconstructions, Geochimica et Cosmochimica Acta, 74, 4639-4654, https://doi.org/10.1016/j.gca.2010.05.027, 2010.

Klein, K., Weniger, G.-C., Ludwig, P., Stepanek, C., Zhang, X., Wegener, C., and Shao, Y.: Assessing climatic impact on transition from Neanderthal to anatomically modern human population on Iberian Peninsula: a macroscopic perspective, Science Bulletin, 68, 1176-1186, https://doi.org/10.1016/j.scib.2023.04.025, 2023.

Lambeck, K., Purcell, A., Zhao, J., and Svensson, N.-O.: The Scandinavian Ice Sheet: from MIS 4 to the end of the Last Glacial Maximum, Boreas, 39, 410-435, https://doi.org/10.1111/j.1502-3885.2010.00140.x, 2010.

Lamping, N., Müller, J., Esper, O., Hillenbrand, C.-D., Smith, J. A., and Kuhn, G.: Highly branched isoprenoids reveal onset of deglaciation followed by dynamic sea-ice conditions in the western Amundsen Sea, Antarctica, Quaternary Science Reviews, 228, 106103, https://doi.org/10.1016/j.quascirev.2019.106103, 2020.

Lamping, N., Müller, J., Hefter, J., Mollenhauer, G., Haas, C., Shi, X., Vorrath, M. E., Lohmann, G., and Hillenbrand, C. D.: Evaluation of lipid biomarkers as proxies for sea ice and ocean temperatures along the Antarctic continental margin, Clim. Past, 17, 2305-2326, https://doi.org/10.5194/cp-17-2305-2021, 2021.

Laskar, J., Robutel, P., Joutel, F., Gastineau, M., Correia, A. C. M., and Levrard, B.: A long-term numerical solution for the insolation quantities of the Earth, A&A, 428, 261-285, https://doi.org/10.1051/0004-6361:20041335, 2004.

Lee, J. I., Bak, Y.-S., Yoo, K.-C., Lim, H. S., Yoon, H. I., and Yoon, S. H.: Climate changes in the South Orkney Plateau during the last 8600 years, The Holocene, 20, 395-404, https://doi.org/10.1177/0959683609353430, 2010.

Leventer, A.: The fate of Antarctic “sea ice diatoms” and their use as paleoenvironmental indicators, Antarctic sea ice: biological processes, interactions and variability, 73, 121-137, 1998.

Liu, R., Han, Z., Zhao, J., Zhang, H., Li, D., Ren, J., Pan, J., and Zhang, H.: Distribution and source of glycerol dialkyl glycerol tetraethers (GDGTs) and the applicability of GDGT-based temperature proxies in surface sediments of Prydz Bay, East Antarctica, Polar Research, 39, https://doi.org/10.33265/polar.v39.3557, 2020.

Liu, X.-L., Summons, R. E., and Hinrichs, K.-U.: Extending the known range of glycerol ether lipids in the environment: structural assignments based on tandem mass spectral fragmentation patterns, Rapid Communications in Mass Spectrometry, 26, 2295-2302, https://doi.org/10.1002/rcm.6355, 2012a.

Liu, X.-L., Lipp, J. S., Simpson, J. H., Lin, Y.-S., Summons, R. E., and Hinrichs, K.-U.: Mono- and dihydroxyl glycerol dibiphytanyl glycerol tetraethers in marine sediments: Identification of both core and intact polar lipid forms, Geochimica et Cosmochimica Acta, 89, 102-115, https://doi.org/10.1016/j.gca.2012.04.053, 2012b.

Locarnini, R. A., Mishonov, A. V., Baranova, O. K., Boyer, T. P., Zweng, M. M., Garcia, H. E., Reagan, J. R., Seidov, D., Weathers, K., Paver, C. R., and Smolyar, I.: World Ocean Atlas 2018, Volume 1: Temperature [dataset], 2018.

Loveland, T. R., Reed, B. C., Brown, J. F., Ohlen, D. O., Zhu, Z., Yang, L., and Merchant, J. W.: Development of a global land cover characteristics database and IGBP DISCover from 1 km AVHRR data, International Journal of Remote Sensing, 21, 1303-1330, https://doi.org/10.1080/014311600210191, 2000.

Lü, X., Liu, X.-L., Elling, F. J., Yang, H., Xie, S., Song, J., Li, X., Yuan, H., Li, N., and Hinrichs, K.-U.: Hydroxylated isoprenoid GDGTs in Chinese coastal seas and their potential as a paleotemperature proxy for mid-to-low latitude marginal seas, Organic Geochemistry, 89-90, 31-43, https://doi.org/10.1016/j.orggeochem.2015.10.004, 2015.

Lunt, D. J., Abe-Ouchi, A., Bakker, P., Berger, A., Braconnot, P., Charbit, S., Fischer, N., Herold, N., Jungclaus, J. H., Khon, V. C., Krebs-Kanzow, U., Langebroek, P. M., Lohmann, G., Nisancioglu, K. H., Otto-Bliesner, B. L., Park, W., Pfeiffer, M., Phipps, S. J., Prange, M., Rachmayani, R., Renssen, H., Rosenbloom, N., Schneider, B., Stone, E. J., Takahashi, K., Wei, W., Yin, Q., and Zhang, Z. S.: A multi-model assessment of last interglacial temperatures, Clim. Past, 9, 699-717, https://doi.org/10.5194/cp-9-699-2013, 2013.

Luo, F., Ying, J., Liu, T., and Chen, D.: Origins of Southern Ocean warm sea surface temperature bias in CMIP6 models, npj Climate and Atmospheric Science, 6, 127, https://doi.org/10.1038/s41612-023-00456-6, 2023.

Marino, G., Rohling, E. J., Rodríguez-Sanz, L., Grant, K. M., Heslop, D., Roberts, A. P., Stanford, J. D., and Yu, J.: Bipolar seesaw control on last interglacial sea level, Nature, 522, 197-201, https://doi.org/10.1038/nature14499, 2015.

Marsland, S. J., Haak, H., Jungclaus, J. H., Latif, M., and Röske, F.: The Max-Planck-Institute global ocean/sea ice model with orthogonal curvilinear coordinates, Ocean Modelling, 5, 91-127, https://doi.org/10.1016/S1463-5003(02)00015-X, 2003.

Massé, G., Belt, S. T., Crosta, X., Schmidt, S., Snape, I., Thomas, D. N., and Rowland, S. J.: Highly branched isoprenoids as proxies for variable sea ice conditions in the Southern Ocean, Antarctic Science, 23, 487-498, https://doi.org/10.1017/S0954102011000381, 2011.

Massom, R. A., Scambos, T. A., Bennetts, L. G., Reid, P., Squire, V. A., and Stammerjohn, S. E.: Antarctic ice shelf disintegration triggered by sea ice loss and ocean swell, Nature, 558, 383-389, https://doi.org/10.1038/s41586-018-0212-1, 2018.

Massom, R. A., Giles, A. B., Warner, R. C., Fricker, H. A., Legrésy, B., Hyland, G., Lescarmontier, L., and Young, N.: External influences on the Mertz Glacier Tongue (East Antarctica) in the decade leading up to its calving in 2010, Journal of Geophysical Research: Earth Surface, 120, 490-506, https://doi.org/10.1002/2014JF003223, 2015.

Masson-Delmotte, V., Buiron, D., Ekaykin, A., Frezzotti, M., Gallée, H., Jouzel, J., Krinner, G., Landais, A., Motoyama, H., Oerter, H., Pol, K., Pollard, D., Ritz, C., Schlosser, E., Sime, L. C., Sodemann, H., Stenni, B., Uemura, R., and Vimeux, F.: A comparison of the present and last interglacial periods in six Antarctic ice cores, Clim. Past, 7, 397-423, https://doi.org/10.5194/cp-7-397-2011, 2011.

Michalchuk, B. R., Anderson, J. B., Wellner, J. S., Manley, P. L., Majewski, W., and Bohaty, S.: Holocene climate and glacial history of the northeastern Antarctic Peninsula: the marine sedimentary record from a long SHALDRIL core, Quaternary Science Reviews, 28, 3049-3065, https://doi.org/10.1016/j.quascirev.2009.08.012, 2009.

Morozov, E. G., Frey, D. I., and Tarakanov, R. Y.: Antarctic Bottom Water Flow through the Eastern Part of the Philip Passage in the Weddell Sea, Oceanology, 60, 589-592, https://doi.org/10.1134/S000143702005015X, 2020.

Müller, J., Wagner, A., Fahl, K., Stein, R., Prange, M., and Lohmann, G.: Towards quantitative sea ice reconstructions in the northern North Atlantic: A combined biomarker and numerical modelling approach, Earth and Planetary Science Letters, 306, 137-148, https://doi.org/10.1016/j.epsl.2011.04.011, 2011.

Müller, P. J. and Schneider, R.: An automated leaching method for the determination of opal in sediments and particulate matter, Deep Sea Research Part I: Oceanographic Research Papers, 40, 425-444, 1993.

Naughten, K. A., Meissner, K. J., Galton-Fenzi, B. K., England, M. H., Timmermann, R., Hellmer, H. H., Hattermann, T., and Debernard, J. B.: Intercomparison of Antarctic ice-shelf, ocean, and sea-ice interactions simulated by MetROMS-iceshelf and FESOM 1.4, Geosci. Model Dev., 11, 1257-1292, https://doi.org/10.5194/gmd-11-1257-2018, 2018.

Naveira Garabato, A. C., McDonagh, E. L., Stevens, D. P., Heywood, K. J., and Sanders, R. J.: On the export of Antarctic Bottom Water from the Weddell Sea, Deep Sea Research Part II: Topical Studies in Oceanography, 49, 4715-4742, https://doi.org/10.1016/S0967-0645(02)00156-X, 2002.

Ó Cofaigh, C., Davies, B. J., Livingstone, S. J., Smith, J. A., Johnson, J. S., Hocking, E. P., Hodgson, D. A., Anderson, J. B., Bentley, M. J., Canals, M., Domack, E., Dowdeswell, J. A., Evans, J., Glasser, N. F., Hillenbrand, C.-D., Larter, R. D., Roberts, S. J., and Simms, A. R.: Reconstruction of ice-sheet changes in the Antarctic Peninsula since the Last Glacial Maximum, Quaternary Science Reviews, 100, 87-110, https://doi.org/10.1016/j.quascirev.2014.06.023, 2014.

Olbers, D., Gouretsky, V., Seiss, G., and Schröter, J.: Hydrographic atlas of the Southern Ocean, Alfred-Wegener-Institut, Bremerhaven1992.

Orsi, A. H., Johnson, G. C., and Bullister, J. L.: Circulation, mixing, and production of Antarctic Bottom Water, Progress in Oceanography, 43, 55-109, https://doi.org/10.1016/S0079-6611(99)00004-X, 1999.

Orsi, A. H., Nowlin, W. D., and Whitworth, T.: On the circulation and stratification of the Weddell Gyre, Deep Sea Research Part I: Oceanographic Research Papers, 40, 169-203, https://doi.org/10.1016/0967-0637(93)90060-G, 1993.

Orsi, A. H., Whitworth, T., and Nowlin, W. D.: On the meridional extent and fronts of the Antarctic Circumpolar Current, Deep Sea Research Part I: Oceanographic Research Papers, 42, 641-673, https://doi.org/10.1016/0967-0637(95)00021-W, 1995.

Otto-Bliesner, B. L., Rosenbloom, N., Stone, E. J., McKay, N. P., Lunt, D. J., Brady, E. C., and Overpeck, J. T.: How warm was the last interglacial? New model–data comparisons, Philosophical Transactions of the Royal Society A: Mathematical, Physical and Engineering Sciences, 371, 20130097, https://doi.org/10.1098/rsta.2013.0097, 2013.

Otto-Bliesner, B. L., Braconnot, P., Harrison, S. P., Lunt, D. J., Abe-Ouchi, A., Albani, S., Bartlein, P. J., Capron, E., Carlson, A. E., Dutton, A., Fischer, H., Goelzer, H., Govin, A., Haywood, A., Joos, F., LeGrande, A. N., Lipscomb, W. H., Lohmann, G., Mahowald, N., Nehrbass-Ahles, C., Pausata, F. S. R., Peterschmitt, J. Y., Phipps, S. J., Renssen, H., and Zhang, Q.: The PMIP4 contribution to CMIP6 – Part 2: Two interglacials, scientific objective and experimental design for Holocene and Last Interglacial simulations, Geosci. Model Dev., 10, 3979-4003, https://doi.org/10.5194/gmd-10-3979-2017, 2017.

Park, E., Hefter, J., Fischer, G., Iversen, M. H., Ramondenc, S., Nöthig, E. M., and Mollenhauer, G.: Seasonality of archaeal lipid flux and GDGT-based thermometry in sinking particles of high-latitude oceans: Fram Strait (79°N) and Antarctic Polar Front (50°S), Biogeosciences, 16, 2247-2268, https://doi.org/10.5194/bg-16-2247-2019, 2019.

Pedro, J. B., van Ommen, T. D., Rasmussen, S. O., Morgan, V. I., Chappellaz, J., Moy, A. D., Masson-Delmotte, V., and Delmotte, M.: The last deglaciation: timing the bipolar seesaw, Clim. Past, 7, 671-683, https://doi.org/10.5194/cp-7-671-2011, 2011.

Pedro, J. B., Bostock, H. C., Bitz, C. M., He, F., Vandergoes, M. J., Steig, E. J., Chase, B. M., Krause, C. E., Rasmussen, S. O., Markle, B. R., and Cortese, G.: The spatial extent and dynamics of the Antarctic Cold Reversal, Nature Geoscience, 9, 51-55, https://doi.org/10.1038/ngeo2580, 2016.

Pellichero, V., Sallée, J.-B., Chapman, C. C., and Downes, S. M.: The southern ocean meridional overturning in the sea-ice sector is driven by freshwater fluxes, Nature Communications, 9, 1789, https://doi.org/10.1038/s41467-018-04101-2, 2018.

Pfeiffer, M. and Lohmann, G.: Greenland Ice Sheet influence on Last Interglacial climate: global sensitivity studies performed with an atmosphere–ocean general circulation model, Clim. Past, 12, 1313-1338, https://doi.org/10.5194/cp-12-1313-2016, 2016.

Pitcher, A., Hopmans, E. C., Mosier, A. C., Park, S. J., Rhee, S. K., Francis, C. A., Schouten, S., and Sinninghe Damsté, J. S.: Core and intact polar glycerol dibiphytanyl glycerol tetraether lipids of ammonia-oxidizing Archaea enriched from marine and estuarine sediments, Applied and Environmental Microbiology, 77, 3468-3477, https://doi.org/10.1128/AEM.02758-10, 2011.

Pollard, D. and DeConto, R. M.: Modelling West Antarctic ice sheet growth and collapse through the past five million years, Nature, 458, 329-332, https://doi.org/10.1038/nature07809, 2009.

Raddatz, T. J., Reick, C. H., Knorr, W., Kattge, J., Roeckner, E., Schnur, R., Schnitzler, K. G., Wetzel, P., and Jungclaus, J.: Will the tropical land biosphere dominate the climate–carbon cycle feedback during the twenty-first century?, Climate Dynamics, 29, 565-574, https://doi.org/10.1007/s00382-007-0247-8, 2007.

Reynolds, R. W., Rayner, N. A., Smith, T. M., Stokes, D. C., and Wang, W.: An Improved In Situ and Satellite SST Analysis for Climate, Journal of Climate, 15, 1609-1625, https://doi.org/10.1175/1520-0442(2002)015<1609:AIISAS>2.0.CO;2, 2002.

Reynolds, R. W., Smith, T. M., Liu, C., Chelton, D. B., Casey, K. S., and Schlax, M. G.: Daily High-Resolution-Blended Analyses for Sea Surface Temperature, Journal of Climate, 20, 5473-5496, https://doi.org/10.1175/2007JCLI1824.1, 2007.

Rhodes, R., Kohfeld, K., Bostock, H., Crosta, X., Leventer, A., Meissner, K., and Esper, O.: Understanding past changes in sea ice in the Southern Ocean, Past Global Changes Magazine, 27(1), 31, https://doi.org/10.22498/pages.27.1.31, 2019.

Riaux-Gobin, C. and Poulin, M.: Possible symbiosis of Berkeleya adeliensis Medlin, Synedropsis fragilis (Manguin) Hasle et al. and Nitzschia lecointei Van Heurck (Bacillariophyta) associated with land-fast ice in Adélie Land, Antarctica, Diatom Research, 19, 265-274, 2004.

Rintoul, S. R.: The global influence of localized dynamics in the Southern Ocean, Nature, 558, 209-218, https://doi.org/10.1038/s41586-018-0182-3, 2018.

Roach, L. A., Eisenman, I., Wagner, T. J. W., Blanchard-Wrigglesworth, E., and Bitz, C. M.: Asymmetry in the seasonal cycle of Antarctic sea ice driven by insolation, Nature Geoscience, 15, 277-281, https://doi.org/10.1038/s41561-022-00913-6, 2022.

Robel, A. A.: Thinning sea ice weakens buttressing force of iceberg mélange and promotes calving, Nature Communications, 8, 14596, https://doi.org/10.1038/ncomms14596, 2017.

Rohling, E. J., Hibbert, F. D., Williams, F. H., Grant, K. M., Marino, G., Foster, G. L., Hennekam, R., de Lange, G. J., Roberts, A. P., Yu, J., Webster, J. M., and Yokoyama, Y.: Differences between the last two glacial maxima and implications for ice-sheet, δ18O, and sea-level reconstructions, Quaternary Science Reviews, 176, 1-28, https://doi.org/10.1016/j.quascirev.2017.09.009, 2017.

Ryves, D. B., Battarbee, R. W., and Fritz, S. C.: The dilemma of disappearing diatoms: Incorporating diatom dissolution data into palaeoenvironmental modelling and reconstruction, Quaternary Science Reviews, 28, 120-136, https://doi.org/10.1016/j.quascirev.2008.08.021, 2009.

Sadatzki, H., Opdyke, B., Menviel, L., Leventer, A., Hope, J. M., Brocks, J. J., Fallon, S., Post, A. L., O'Brien, P. E., Grant, K., and Armand, L.: Early sea ice decline off East Antarctica at the last glacial–interglacial climate transition, Science Advances, 9, eadh9513, https://doi.org/10.1126/sciadv.adh9513, 2023.

Seabrooke, J. M., Hufford, G. L., and Elder, R. B.: Formation of Antarctic bottom water in the Weddell Sea, Journal of Geophysical Research (1896-1977), 76, 2164-2178, https://doi.org/10.1029/JC076i009p02164, 1971.

Shevenell, A. E., Domack, E. W., and Kernan, G. M.: Record of Holocene palaeoclimate change along the Antarctic Peninsula: evidence from glacial marine sediments, Lallemand Fjord, Papers and Proceedings of the Royal Society of Tasmania, 55-64,

Sinninghe Damsté, J. S., Rijpstra, W. I. C., Hopmans, E. C., Jung, J., Kim, J. H., Rhee, S. K., Stieglmeier, M., and Schleper, C.: Intact Polar and Core Glycerol Dibiphytanyl Glycerol Tetraether Lipids of Group I.1a and I.1b Thaumarchaeota in Soil, Applied and Environmental Microbiology, 78, 6866-6874, https://doi.org/10.1128/AEM.01681-12, 2012.

Smik, L., Belt, S. T., Lieser, J. L., Armand, L. K., and Leventer, A.: Distributions of highly branched isoprenoid alkenes and other algal lipids in surface waters from East Antarctica: Further insights for biomarker-based paleo sea-ice reconstruction, Organic Geochemistry, 95, 71-80, https://doi.org/10.1016/j.orggeochem.2016.02.011, 2016.

Stepanek, C. and Lohmann, G.: Modelling mid-Pliocene climate with COSMOS, Geosci. Model Dev., 5, 1221-1243, https://doi.org/10.5194/gmd-5-1221-2012, 2012.

Stepanek, C., Samakinwa, E., Knorr, G., and Lohmann, G.: Contribution of the coupled atmosphere–ocean–sea ice–vegetation model COSMOS to the PlioMIP2, Clim. Past, 16, 2275-2323, https://doi.org/10.5194/cp-16-2275-2020, 2020.

Stevens, B., Giorgetta, M., Esch, M., Mauritsen, T., Crueger, T., Rast, S., Salzmann, M., Schmidt, H., Bader, J., Block, K., Brokopf, R., Fast, I., Kinne, S., Kornblueh, L., Lohmann, U., Pincus, R., Reichler, T., and Roeckner, E.: Atmospheric component of the MPI-M Earth System Model: ECHAM6, Journal of Advances in Modeling Earth Systems, 5, 146-172, https://doi.org/10.1002/jame.20015, 2013.

Sutter, J., Gierz, P., Grosfeld, K., Thoma, M., and Lohmann, G.: Ocean temperature thresholds for Last Interglacial West Antarctic Ice Sheet collapse, Geophysical Research Letters, 43, 2675-2682, https://doi.org/10.1002/2016GL067818, 2016.

Tarasov, L., Dyke, A. S., Neal, R. M., and Peltier, W. R.: A data-calibrated distribution of deglacial chronologies for the North American ice complex from glaciological modeling, Earth and Planetary Science Letters, 315-316, 30-40, https://doi.org/10.1016/j.epsl.2011.09.010, 2012.

Taylor, F. and Sjunneskog, C.: Postglacial marine diatom record of the Palmer Deep, Antarctic Peninsula (ODP Leg 178, Site 1098) 2. Diatom assemblages, Paleoceanography, 17, PAL 2-1-PAL 2-12, https://doi.org/10.1029/2000PA000564, 2002.

Taylor, F., Whitehead, J., and Domack, E.: Holocene paleoclimate change in the Antarctic Peninsula: evidence from the diatom, sedimentary and geochemical record, Marine Micropaleontology, 41, 25-43, https://doi.org/10.1016/S0377-8398(00)00049-9, 2001.

Thompson, A. F., Stewart, A. L., Spence, P., and Heywood, K. J.: The Antarctic Slope Current in a Changing Climate, Reviews of Geophysics, 56, 741-770, https://doi.org/10.1029/2018RG000624, 2018.

Turney, C. S. M., Fogwill, C. J., Golledge, N. R., McKay, N. P., van Sebille, E., Jones, R. T., Etheridge, D., Rubino, M., Thornton, D. P., Davies, S. M., Ramsey, C. B., Thomas, Z. A., Bird, M. I., Munksgaard, N. C., Kohno, M., Woodward, J., Winter, K., Weyrich, L. S., Rootes, C. M., Millman, H., Albert, P. G., Rivera, A., van Ommen, T., Curran, M., Moy, A., Rahmstorf, S., Kawamura, K., Hillenbrand, C.-D., Weber, M. E., Manning, C. J., Young, J., and Cooper, A.: Early Last Interglacial ocean warming drove substantial ice mass loss from Antarctica, Proceedings of the National Academy of Sciences, 117, 3996-4006, https://doi.org/10.1073/pnas.1902469117, 2020.

Varma, V., Prange, M., Merkel, U., Kleinen, T., Lohmann, G., Pfeiffer, M., Renssen, H., Wagner, A., Wagner, S., and Schulz, M.: Holocene evolution of the Southern Hemisphere westerly winds in transient

simulations with global climate models, Clim. Past, 8, 391-402, https://doi.org/10.5194/cp-8-391-2012, 2012.

Vaughan, D. G., Comiso, J. C., Allison, I., Carrasco, J., Kaser, G., Kwok, R., Mote, P., Murray, T., Paul, F., Ren, J., Rigno, E., Solomina, O., Steffen, K., and Zhang, T.: Observations: Cryosphere, Cambridge University Press, Cambridge, United Kingdom and New York, NY, USA, 2013.

Vernet, M., Geibert, W., Hoppema, M., Brown, P. J., Haas, C., Hellmer, H. H., Jokat, W., Jullion, L., Mazloff, M., Bakker, D. C. E., Brearley, J. A., Croot, P., Hattermann, T., Hauck, J., Hillenbrand, C.-D., Hoppe, C. J. M., Huhn, O., Koch, B. P., Lechtenfeld, O. J., Meredith, M. P., Naveira Garabato, A. C., Nöthig, E.-M., Peeken, I., Rutgers van der Loeff, M. M., Schmidtko, S., Schröder, M., Strass, V. H., Torres-Valdés, S., and Verdy, A.: The Weddell Gyre, Southern Ocean: Present Knowledge and Future Challenges, Reviews of Geophysics, 57, 623-708, https://doi.org/10.1029/2018RG000604, 2019.

Viseras, C. and Maldonado, A.: Facies architecture, seismic stratigraphy and development of a high-latitude basin: the Powell Basin (Antarctica), Marine Geology, 157, 69-87, https://doi.org/10.1016/S0025-3227(98)00136-4, 1999.

Vorrath, M. E., Müller, J., Esper, O., Mollenhauer, G., Haas, C., Schefuß, E., and Fahl, K.: Highly branched isoprenoids for Southern Ocean sea ice reconstructions: a pilot study from the Western Antarctic Peninsula, Biogeosciences, 16, 2961-2981, https://doi.org/10.5194/bg-16-2961-2019, 2019.

Vorrath, M. E., Müller, J., Rebolledo, L., Cárdenas, P., Shi, X., Esper, O., Opel, T., Geibert, W., Muñoz, P., Haas, C., Kuhn, G., Lange, C. B., Lohmann, G., and Mollenhauer, G.: Sea ice dynamics in the Bransfield Strait, Antarctic Peninsula, during the past 240 years: a multi-proxy intercomparison study, Clim. Past, 16, 2459-2483, https://doi.org/10.5194/cp-16-2459-2020, 2020.

Vorrath, M. E., Müller, J., Cárdenas, P., Opel, T., Mieruch, S., Esper, O., Lembke-Jene, L., Etourneau, J., Vieth-Hillebrand, A., Lahajnar, N., Lange, C. B., Leventer, A., Evangelinos, D., Escutia, C., and Mollenhauer, G.: Deglacial and Holocene sea-ice and climate dynamics in the Bransfield Strait, northern Antarctic Peninsula, Clim. Past, 19, 1061-1079, https://doi.org/10.5194/cp-19-1061-2023, 2023.

Waelbroeck, C., Skinner, L. C., Labeyrie, L., Duplessy, J.-C., Michel, E., Vazquez Riveiros, N., Gherardi, J.-M., and Dewilde, F.: The timing of deglacial circulation changes in the Atlantic, Paleoceanography, 26, https://doi.org/10.1029/2010PA002007, 2011.

Watson, A. J., Vallis, G. K., and Nikurashin, M.: Southern Ocean buoyancy forcing of ocean ventilation and glacial atmospheric CO2, Nature Geoscience, 8, 861-864, https://doi.org/10.1038/ngeo2538, 2015.

Weber, M. E., Bailey, I., Hemming, S. R., Martos, Y. M., Reilly, B. T., Ronge, T. A., Brachfeld, S., Williams, T., Raymo, M., Belt, S. T., Smik, L., Vogel, H., Peck, V. L., Armbrecht, L., Cage, A., Cardillo, F. G., Du, Z., Fauth, G., Fogwill, C. J., Garcia, M., Garnsworthy, M., Glüder, A., Guitard, M., Gutjahr, M., Hernández-Almeida, I., Hoem, F. S., Hwang, J.-H., Iizuka, M., Kato, Y., Kenlee, B., Oconnell, S., Pérez, L. F., Seki, O., Stevens, L., Tauxe, L., Tripathi, S., Warnock, J., and Zheng, X.: Antiphased dust deposition and productivity in the Antarctic Zone over 1.5 million years, Nature Communications, 13, 2044, https://doi.org/10.1038/s41467-022-29642-5, 2022.

Wei, W. and Lohmann, G.: Simulated Atlantic Multidecadal Oscillation during the Holocene, Journal of Climate, 25, 6989-7002, https://doi.org/10.1175/JCLI-D-11-00667.1, 2012.

Williams, T. J., Martin, E. E., Sikes, E., Starr, A., Umling, N. E., and Glaubke, R.: Neodymium isotope evidence for coupled Southern Ocean circulation and Antarctic climate throughout the last 118,000 years, Quaternary Science Reviews, 260, 106915, https://doi.org/10.1016/j.quascirev.2021.106915, 2021.

Xiao, W., Esper, O., and Gersonde, R.: Last Glacial - Holocene climate variability in the Atlantic sector of the Southern Ocean, Quaternary Science Reviews, 135, 115-137, https://doi.org/10.1016/j.quascirev.2016.01.023, 2016a.

Xiao, W., Frederichs, T., Gersonde, R., Kuhn, G., Esper, O., and Zhang, X.: Constraining the dating of late Quaternary marine sediment records from the Scotia Sea (Southern Ocean), Quaternary Geochronology, 31, 97-118, https://doi.org/10.1016/j.quageo.2015.11.003, 2016b.

Xiao, W., Xu, Y., Zhang, C., Lin, J., Wu, W., Lü, X., Tan, J., Zhang, X., Zheng, F., Song, X., Zhu, Y., Yang, Y., Zhang, H., Wenzhöfer, F., Rowden, A. A., and Glud, R. N.: Disentangling Effects of Sea Surface Temperature and Water Depth on Hydroxylated Isoprenoid GDGTs: Insights From the Hadal Zone and Global Sediments, Geophysical Research Letters, 50, e2023GL103109, https://doi.org/10.1029/2023GL103109, 2023.

Zhang, X., Knorr, G., Lohmann, G., and Barker, S.: Abrupt North Atlantic circulation changes in response to gradual CO2 forcing in a glacial climate state, Nature Geoscience, 10, 518-523, https://doi.org/10.1038/ngeo2974, 2017.

Zhang, X., Lohmann, G., Knorr, G., and Xu, X.: Different ocean states and transient characteristics in Last Glacial Maximum simulations and implications for deglaciation, Clim. Past, 9, 2319-2333, https://doi.org/10.5194/cp-9-2319-2013, 2013.

Zhang, Y. G., Pagani, M., and Wang, Z.: Ring Index: A new strategy to evaluate the integrity of TEX86 paleothermometry, Paleoceanography, 31, 220-232, https://doi.org/10.1002/2015PA002848, 2016.

Zielinski, U. and Gersonde, R.: Diatom distribution in Southern Ocean surface sediments (Atlantic sector): Implications for paleoenvironmental reconstructions, Palaeogeography, Palaeoclimatology, Palaeoecology, 129, 213-250, https://doi.org/10.1016/S0031-0182(96)00130-7, 1997.

Ice-proximal sea-ice reconstruction in Powell Basin, Antarctica since the Last Interglacial

Wee Wei Khoo et al.

S1: Age model

The age model of marine sediment core PS118_63-1 was first established using a comparative analysis ofbetween the XRF-Ti, magnetic susceptibility (MS), wet bulk density and total organic carbon (TOC) records against that of with the EDML $\delta^{18}O$ record (Supplementary Fig. S1). Glacial and/or cold periods (i.e., MIS 2-4, 5d and 6) within core PS118_63-1 were identified based on higher XRF-Ti, MS and density values, and lower TOC contents, while low/decreasing XRF-Ti, MS and density values with elevated TOC contents reflect the interglacial/warm periods (i.e., MIS 1 and 5e) in the core. Furthermore, the MIS 5/6 boundary is indicated by the biostratigraphic marker *Rouxia leventerae* (ca. 130 ka BP; Zielinski et al., 2002). Since <1% relative abundance of *Rouxia leventerae* was found at core depth 6.19 m (0.6%), we estimated the last occurrence of *Rouxia leventerae* to be around 6.2 m. Planktic foraminifera were also selected for AMS ^{14}C-dating (Supplementary Table S1) using the Mini Carbon Dating System (MICADAS; Mollenhauer et al., 2021) at the Alfred Wegener Institute (AWI), Bremerhaven, Germany. The ^{14}C ages were calibrated to calendar ages using the PaleoDataView software (v0.9.5.25; Butzin et al., 2017; Heaton et al., 2020; Langner and Mulitza, 2019).

Additionally, tTo further refine the age model within each glacial/interglacial interval, we considered additional age control tie points identified in records from a nearby marine core U1537 (MS, XRF-Fe and Opal) and the EDML ice core (ssNa+). See Supplementary Fig. S2 for the tie points identified in the respective records of marine core PS118_63-1 with marine core U1537 and the EDML ice core. During the correlation analysis, multiple records from the same core were examined collectively to ensure that the age-depth ranges of respective tie points remained consistent across all records. The eventual tuning of theserecords from cores U1537 and EDML ice core with marine core PS118_63-1 was conducted using the QAnalyseries software (v1.5.1; Kotov and Pälike, 2018). A final comparison was then made between all the tie points identified from marine cores PS118_63-1 (XRF-Ti, Fe, MS, opal and $PIPSO_{25}$), U1537 (MS, XRF-Fe and opal) and EDML ice core ($\delta^{18}O$ and ssNa+). The most suited and/or fitting tie points were selected, while duplicates were rejected (as indicated by the black crosses in Supplementary Fig. S1 and S2). A summary of the tie points used for the establishment of the age model of marine core PS118_63-1 is provided in Supplementary Table S2. To account for age uncertainty, we adopted four age errors provided in the age model of core U1537imposed an age error of ±1 kyr for all the tuning tie points, with the exception of four tie points from U1537-MS. We adopted the age errors from the age model of U1537 for these four tie points instead (refer to Supplementary Table 2 of Weber et al., 2022), and with them as reference, an age error of ±1 kyr was imposed for tie points between MIS 1 and 3, while ±2 kyr was prescribed for tie points from MIS 4-6 (Supplementary Table S2). We also imposed an age error of ±1 kyr for the tie points derived from the EDML $\delta^{18}O$ record. Lastly, the Bayesian age-depth modeling was established using Bacon v2.5.8 (Blaauw and Christen, 2011) on RStudio v2022.07.02.

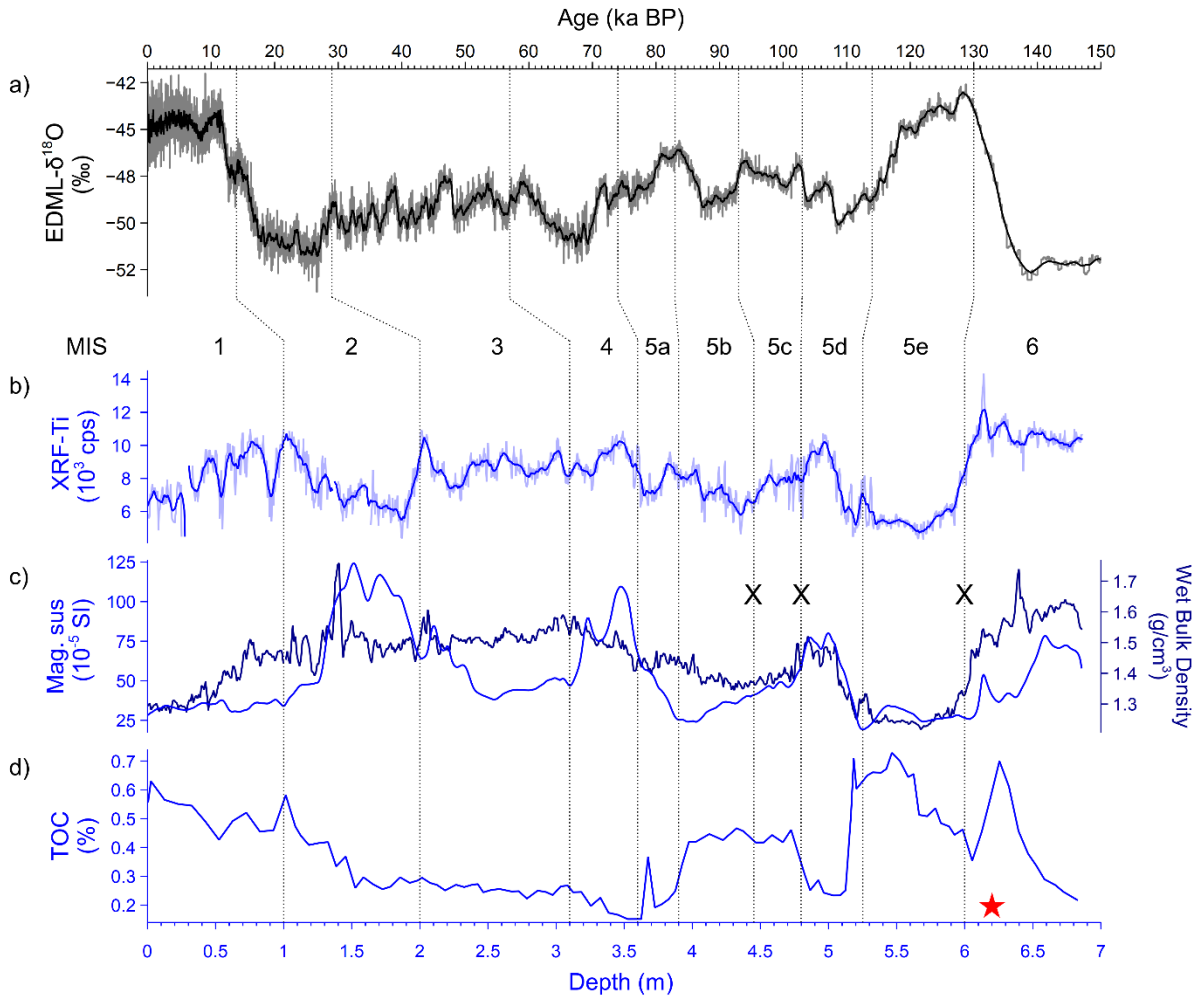

Supplementary Figure S1. Age-depth comparison between the a) EDML $\delta^{18}O$ record against that of records, b) XRF-Ti, c) magnetic susceptibility, wet bulk density and d) TOC from marine sediment core PS118_63-1. Black crosses indicate tie points that were not chosen for use in the final age model after careful comparison between all age control tie points. Red star denotes the depth at which *R. leventerae*, a marker for MIS 5/6 boundary, has been identified. Age intervals for MIS 1-4 and 6 are in accordance to Lisiecki and Raymo (2005) and MIS 5 substages are referenced to Bianchi and Gersonde (2002).

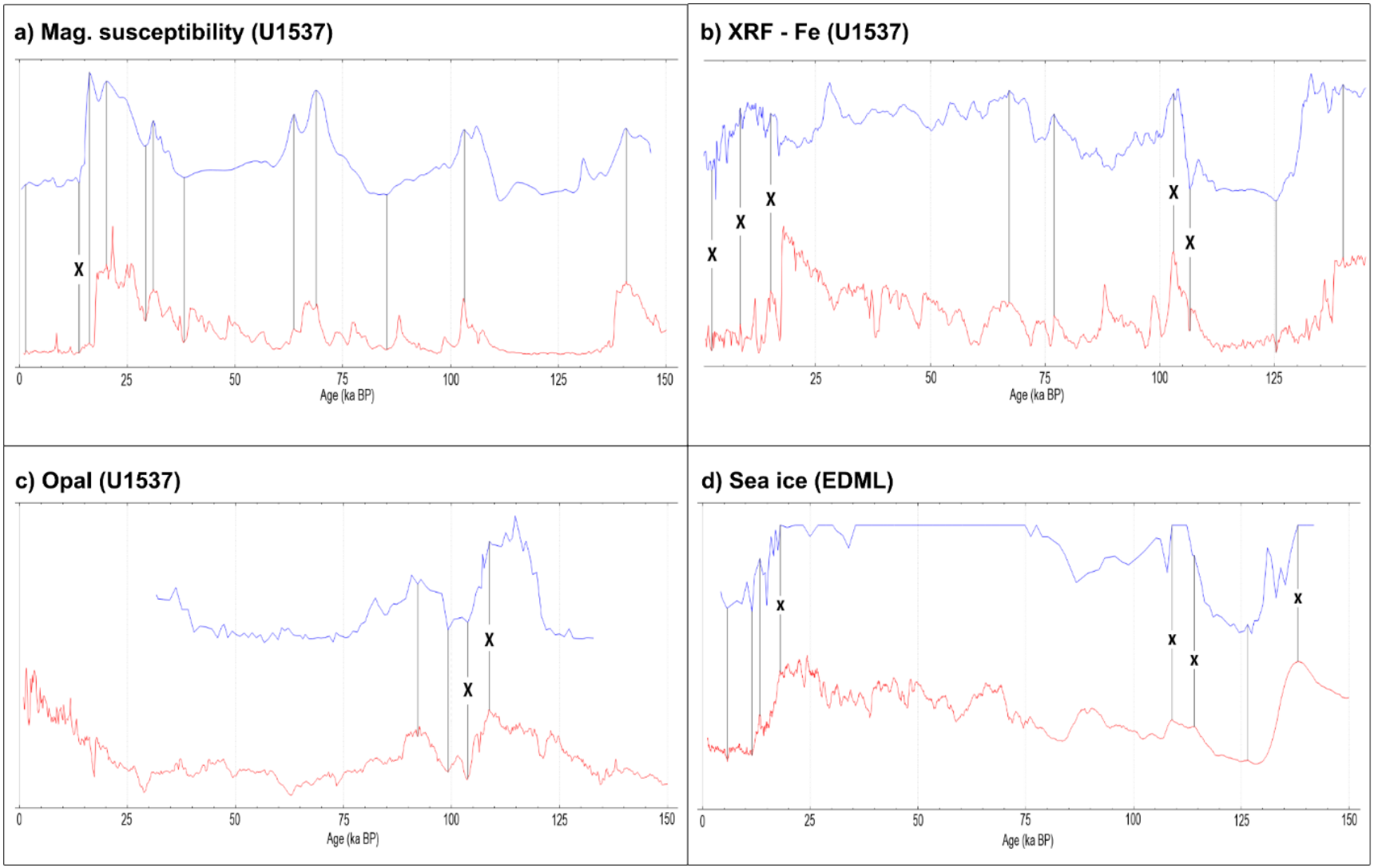

Supplementary Figure S2. Plots of age control tie points identified in records a) magnetic susceptibility, b) XRF – Fe and c) opal records of marine core U1537 (red) against marine core PS118_63-1 (blue), and d) EDML ssNa+ record (red) against that of the $PIPSO_{25}$ record from marine core PS118_63-1 (blue). Black crosses indicate tie points that were not selected for inclusion in the final age model after careful comparison between all tie point records.

Supplementary Table S1. Radiocarbon dates taken from marine sediment core PS118_63-1. Calendar and reservoir ages are in respect to IntCal20 as defined in the PaleoDataView software.

Sample Name	AWI Nr.	Material	$F^{14}C$ (abs)	^{14}C age (kyrs)	Cal age (ka BP)	Reservoir age (kyrs)
PS118_63-1_ 163-165cm	9742.1.1	*N. pachyderma*	0.1259 ±0.0025	16.647 ±0.158	17.603 ±0.935	2.216 ±0.287
PS118_63-1_ 179-181cm	9743.1.1	*N. pachyderma*	0.0845 ±0.0023	19.850 ±0.221	21.422 ±0.862	2.192 ±0.286

Supplementary Table S2: Tie points used for age-depth model for marine sediment core PS118_63-1.

S/N	MIS	Depth (m)	Age (ka BP)	± Age (kyrs)	Tie point
1	1	0.076	1.2	1	U1537-MS
2	1	0.125	5.772	1	EDML-ssNa+
3	1	0.625	10.675	1	EDML-ssNa+
4	1	0.925	13.352	1	EDML-ssNa+
5	1	1	14	1	EDML-$\delta^{18}O$
6	2	1.516	16.2	1	U1537-MS
7	2	1.64	17.603	0.935^	^{14}C-dating
8	2	1.706	20	1	U1537-MS
9	2	1.8	21.422	0.862^	^{14}C-dating
10	3	2	29	1	EDML-$\delta^{18}O$
11	3	2.018	29.21	0.78*	U1537-MS
12	3	2.098	31.2	1	U1537-MS
13	3	2.548	38	1	U1537-MS
14	4	3.1	57	1	EDML-$\delta^{18}O$
15	4	3.228	63.64	2.28*	U1537-MS
16	4	3.46	67.2	~~1~~2	U1537-Fe
17	4	3.478	68.8	2.1*	U1537-MS
18	5a	3.6	74	1	EDML-$\delta^{18}O$
19	5a	3.84	76.8	~~1~~2	U1537-Fe
20	5b	3.9	83	1	EDML-$\delta^{18}O$
21	5b	4.028	85	~~1~~2	U1537-MS
22	5b	4.33	92	~~1~~2	U1537-Opal
23	5c	4.83	99.2	~~1~~2	U1537-Opal
24	5d	4.868	103.17	1.71*	U1537-MS
25	5e	5.25	114	1	EDML-$\delta^{18}O$
26	5e	5.68	125.2	~~1~~2	U1537-Fe
27	5e	5.83	126.336	~~1~~2	EDML-ssNa+
28	6	6.2	130	~~1~~2	*R. leventerae*
29	6	6.56	139.8	~~1~~2	U1537-Fe
30	6	6.588	140.6	~~1~~2	U1537-MS

^Age error taken from calibrated age uncertainty (refer to Supplementary Table S1)

*Age error adopted from age model for marine core U1537 (refer to Supplementary Table 2 of Weber et al., 2022)

S2: ^{230}Th-excess constant-rate-of-supply model

To estimate the ^{230}Th-excess constant-rate-of-supply (CRS) age model for PS118_63-1, a total of 54 freeze-dried, ground~~ed~~ and homogenized sediment samples were selected (at specific depth intervals) for the determination of uranium (U) and thorium (Th) isotopes (^{230}Th, ^{232}Th, ^{238}U and ^{234}U). The samples were first digested in a pressure-assisted microwave digestion system (CEM MarsXpress; 24 samples per batch). Following which, 15 mL of the digested solution underwent a separation and purification process via the seaFAST automatic column separation system, using TRU resin. Each Th/U fraction was then analyzed via sector-field inductively coupled plasma mass spectrometry (SF-ICP-MS Element2). U-isotopes were measured in low resolution using a cyclonic spray chamber, while Th-isotopes were measured with an Apex IR desolvation device for increasing ion yield, and in a custom-made resolution of R=2000 for increasing abundance sensitivity. The methods employed in the determination of ^{230}Th-excess and subsequent CRS-dating for PS118_63-1 are described in Geibert et al. (2019), with the calculation of the CRS age following a method by Appleby and Oldfield (1978).

The robustness of the age model for PS118_63-1 determined using 30 tie points (Supplementary Table S2) is supported by the strong correlation between the tie points-derived age model and estimations via the ^{230}Th-excess CRS-dating approach (Supplementary Fig. S3). The deviations are to be expected considering possible changes in focusing and the limited ^{230}Th-inventory considered in this core.

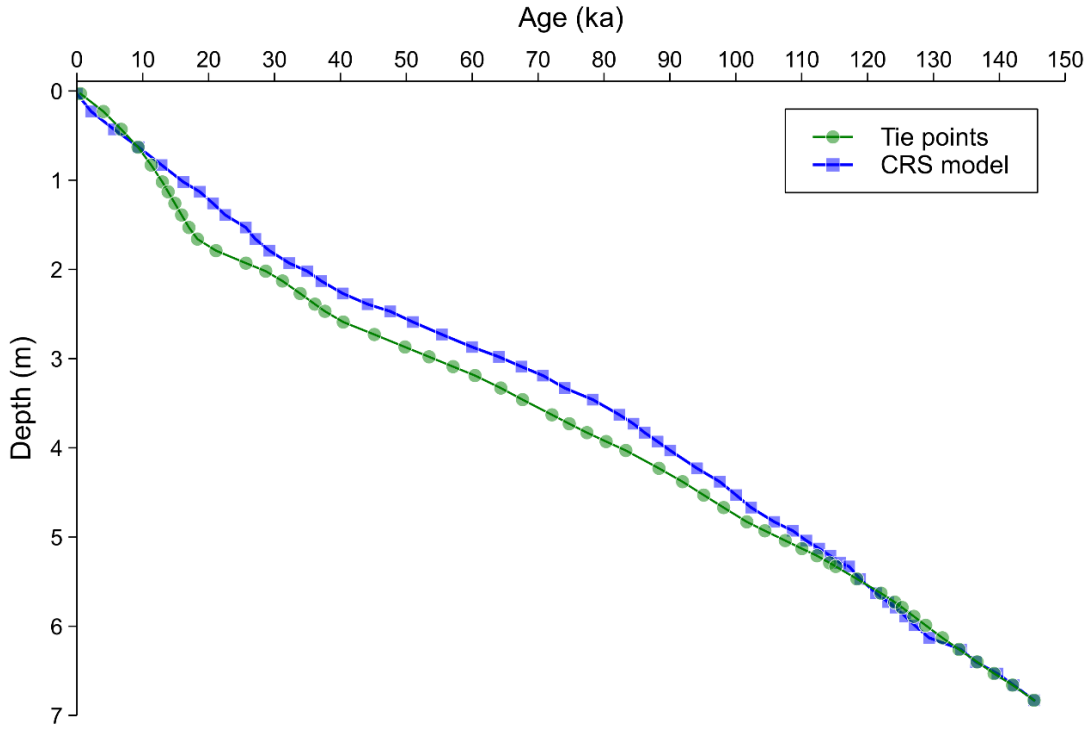

Supplementary Figure S3. Comparison of age-depth profile of PS118_63-1 established based on tie points and ^{230}Th-excess CRS model.

S3: Numerical model and climate simulations

3.1 Community Earth System Models applications

The Community Earth System Models (COSMOS) have been successfully applied for the study of both colder and warmer than present climates – during, and beyond, the Cenozoic, both at orbital and tectonic time scales. In many cases, ~~the~~ COSMOS ~~have~~has helped to improve our understanding of inferences from the geologic record. They have provided a dynamical framework of relevant processes in the climate system that may mechanistically explain reconstructed climate patterns. Examples for this work include simulations of the climates of the Cretaceous (Klages et al., 2020; Niezgodzki et al., 2019), of the Miocene (Hossain et al., 2020; 2021; Knorr and Lohmann, 2014; Knorr et al., 2011; Stein et al., 2016), of the Pliocene (Stepanek and Lohmann, 2012; Stepanek et al., 2020), of the Penultimate Glacial (Stein et al., 2017), of the LIG (Gierz et al., 2017; Pfeiffer and Lohmann, 2016; Stein et al., 2017), of the LGM (Zhang et al., 2013), and of the Holocene (Guagnin et al., 2016). Furthermore, the model has been employed towards a large number of process studies. Among these are the works by Knorr et al. (2021) on glacial termination, the study by Kaboth-Bahr et al. (2021) on the delay of Northern Hemisphere glaciation by Mediterranean heat injection into the North Atlantic Ocean during the Pliocene, the publication by Zhang et al. (2021) on the impact of astronomical forcing on Pleistocene millennial climate variability, and the investigation by Lohmann et al. (2022) on the potential contribution of increased vertical mixing towards reduced meridional temperature gradients in warm climates of the Pliocene and Miocene.

3.2 ~~M~~COSMOS-modeled climate states

The climate states *piControl*, *mh6k*, *lgm21k*, *lig125k*, and *pgm140k* are derived from equilibrium climate simulations, where we analyze the climate state at the end of a spin up. In these cases, ~~the~~ COSMOS have been instantaneously exposed to reconstructions of greenhouse gases and of orbital forcing, and to paleogeography, if applicable. An exception to this methodology is the LIG climate state at 128 ka BP, derived from simulation *lig128k*. This simulation stems from the computation of a transient evolution of LIG climate from 130 ka BP to 115 ka BP, where the COSMOS have been employed with time-varying greenhouse gas concentrations and orbital forcing applying an acceleration of a factor of 10. The initial ocean state at 130 ka BP has been created to mirror conditions that are representative for the penultimate deglaciation, Termination II (TII; 140 – 130 ka BP). This ocean state has been created based on a weak hosing (0.05 Sv) under perpetual 130 ka BP forcing. To derive the climate conditions at 128 ka BP, we average the transient model climate state over the 100 model years that refer to the period from 128.5 ka BP to 127.5 ka BP. Details of the model setups of the various simulations are provided in Supplementary Table S3.

3.3 Comparison of COSMOS with other climate models

There exists an extensive bibliographic record evaluating the performance of COSMOS, in comparison to other climate models including those in the context of the third and fourth phases of the Paleoclimate Modeling Intercomparison Project (PMIP3; Braconnot et al., 2012; PMIP4; Kageyama et al., 2017), which are part of the Climate Modeling Intercomparison Project (CMIP; Eyring et al., 2016). These studies span a wide range of time periods, including the Holocene (Varma et al., 2012; Dallmeyer et al., 2013; 2015), the Last Interglacial (Bakker et al., 2014; Jennings et al., 2015; Lunt et al., 2013), the Pliocene (Haywood et al., 2013; 2020), the Miocene (Burls et al., 2021), and the Eocene (Lunt et al., 2021). A key inference from these published works, relevant to our study, is that among the ensemble of PMIP3-class model simulations of the Southern Ocean, COSMOS, like some models, is known to project a relatively small warm bias in sea surface temperature (SST; see Fig. 4e and f in Lunt et al., 2013). This supports the use of said model in the study of sea ice and SST in the Weddell Sea region.

While the previously mentioned studies cover various aspects of COSMOS's modeled climate in comparison to simulations from other models, these studies provide no perfect match with regard to the time slices and variables considered in our study. Therefore, we provide additional comparison of our results with other PMIP models for those variables and time slices that are relevant to our study. Unfortunately, such an analysis is only possible in an incomplete manner. For instance, direct comparisons of the COSMOS-simulated sea ice and SST with data from the PMIP ensembles must focus on the pre-industrial (PI), mid-Holocene, and Last Glacial Maximum climate states. For the Penultimate Glacial Maximum (140 ka BP) and the two Last Interglacial time slices (128 ka BP and 125 ka BP) employed by us, no comparable PMIP simulations are available. In particular, PMIP3 does not cover any time slice for the Last Interglacial, while PMIP4 considers *lig127k* (127 ka BP) as one singular

time slice during the Last Interglacial (Otto-Bliesner et al., 2017), which is unfortunately out of sync with our Last Interglacial model simulations. Higher-tiered Last Interglacial simulations from PMIP4 (Otto-Bliesner et al., 2017) are as well not overlapping with our work. For reference, we will nevertheless undertake a comparison of our COSMOS data for the 128 and 125 ka BP time slices with the 127 ka BP time slice from the PMIP4 model. This will put our work into the context of recent modeling work on the Last Interglacial.

To facilitate a meaningful comparable model-to-model evaluation of our COSMOS data with results from other climate models in the broader paleoclimate modeling community, we assess our model data against all outputs from the CMIP5/PMIP3 and CMIP6/PMIP4 models available through the Earth System Grid Federation (ESGF; accessed via https://esgf-data.dkrz.de). A list of models used in the PMIP simulations, the search criteria employed during data retrieval, and data citations are provided in Supplementary Table S4. All available data are also systemically selected and pertinent to the climate states under investigation in our study. They include: 1) PMIP3 and PMIP4 simulations *piControl* for a comparison with our PI climate state – here we focus on those models that provide at least one paleoclimate simulation, and other PI climate states are discarded from our analysis; 2) PMIP3 and PMIP4 simulations *mid-Holocene* for a comparison with our 6 ka BP climate state; 3) PMIP3 and PMIP4 simulations *lgm* for comparison with our 21 ka BP climate state; 4) PMIP4 simulation *lig127k* for a comparison with our 128 ka and 125 ka climate states. Our analyses were based on the last 100 model years of simulations, where available. Note that for some models or simulations, data for less than 100 model years have been published via ESGF. We downloaded monthly mean SST (tos) from both CMIP5/PMIP3 and CMIP6/PMIP4 ensembles, monthly mean sea-ice cover (sic) from the CMIP5/PMIP3 ensemble, and monthly mean sea-ice cover (siconc) from the CMIP6/PMIP4 ensemble. In general, data is represented as the monthly climatological mean.

Monthly mean data is unavailable for a small number of models. In such cases, we either computed the monthly mean from daily output or utilized climatological means directly provided by ESGF. Note that not all models provide all variables relevant to our study. Furthermore, inaccessibility of specific data nodes limited our utilization of the full PMIP ensemble. Consequently, we considered all data sets accessible, and this means that ensemble means of sea-ice cover and SST from one specific simulation may not necessarily cover the same models. Models providing at least one relevant dataset are highlighted in Supplementary Table S5.

3.4 PMIP3 and PMIP4 models outputs: An evaluation against COSMOS model findings

In this section, we present the simulated spring/summer (NDJFMA) and winter (ASO) sea-ice cover, and summer (DJF) and winter (JJA) SST results from PMIP3 and PMIP4 models, subject to data availability. The modeled time slices cover the PI, 6, 21 ka BP for PMIP3 and PI, 6, 21 and 127 ka BP for PMIP4. All PMIP ensemble data has been remapped to match the grid used in the COSMOS. For each specific time slice, and CMIP generation, we computed ensemble means and standard deviation of the population (σ_n; for brevity, referred to as σ from here on). Agreement between COSMOS and PMIP3/PMIP4 models results is evaluated based on a 2σ threshold criterion. Results derived from COSMOS are considered as agreeing with the PMIP data if they are within the 2σ range of the ensemble.

3.4.1 Simulated sea-ice cover from PMIP3 and PMIP4 models

Supplementary Fig. S4 and S5 provide simulated spring/summer and winter sea-ice cover plots, considering ensemble means, σ and agreement within 2σ threshold between COSMOS and PMIP3 for three time slices (21, 6 ka BP and PI). Corresponding PMIP4 ensemble means, σ, and comparison with COSMOS are shown for the same time slices in Supplementary Fig. S6.2-4 and S7.2-4. Likewise, panels a and b of Supplementary Fig. S6.1 and S7.1 display the ensemble means and σ simulated by PMIP4 model for 127 ka BP. Supplementary Fig. S6.1c and S7.1c compare PMIP4 127 ka BP simulation results to COSMOS outputs from 128 ka BP, while Supplementary Fig. S6.1d and S7.1d show the level of agreement with COSMOS simulation at 125 ka BP. We observe that the PMIP3/PMIP4 ensemble σ for both the spring/summer and winter seasons are appreciable. The ensemble σ of sea-ice cover during spring/summer is notably higher close to the Antarctic Peninsula and along coastal areas (Supplementary Fig. S4b and S6b). Whilst, for winter sea-ice cover, the PMIP3/PMIP4 models exhibit more pronounced ensemble uncertainty farther away from the continent, increasing towards the edges of the sea-ice extent (Supplementary Fig. S5b and S7b). Comparison of sea-ice data, COSMOS vs. PMIP3, shows agreement within the 2σ threshold criterion at our study sites (Supplementary Fig. S4c and S5c). However, larger regions of disagreement (>2σ threshold) are observed when comparing sea-ice cover in COSMOS to results from PMIP4 (Supplementary Fig. S6c and S7c). For both PMIP3

and PMIP4, there is wider distribution of disagreement along the 50ºS latitude for the 21 ka BP time slice, while smaller disagreements for PI and 6 ka BP are observed near to the edge of the sea-ice extent. Note that simulated winter sea-ice conditions at Site PS118_63-1 agree between COSMOS and PMIP4 across PI, 6 and 21 ka BP. For 21 ka BP, agreement regarding winter sea ice is given for locations of both sites. Only in the case of PMIP4, the winter sea ice for PI and 6 ka BP time slices, as well as the spring/summer sea ice of PI, 6 and 21 ka BP time slices, study sites are outside (but in several cases close to) regions where the 2σ threshold criterion is fulfilled. From these findings, we infer that the COSMOS model generally produces a denser, and in many regions more extensive sea-ice cover compared to PMIP3 and (PMIP4) ensemble models. While at core sites, agreement with PMIP model ensembles is more frequent. Disagreements, when they occur, are biased towards the PMIP4 model, the winter season, and the 21 ka BP. In general, we observe a higher degree of disagreement for simulated sea-ice cover at core site PS67/219-1, which is often closer to the sea ice margin than core site PS118_63-1.

3.4.2 Simulated sea surface temperature from PMIP3 and PMIP4 models

Similarly, the ensemble means, σ and COSMOS-PMIP3 models agreement (within 2σ threshold) for the simulated summer and winter SST plots for the three same time slices are presented in Supplementary Fig. S8 and S9, while those obtained using the PMIP4 model (PI, 6, 21 and 127 ka BP time slices) are provided in Supplementary Fig. S10 and S11. Both PMIP3- and PMIP4-derived SST plots show considerable ensemble σ around the 40-50ºS latitude, especially off the coast of the eastern South American continent (refer to panel b of Supplementary Fig. S8 to S11). Furthermore, a distinctly lower ensemble σ is observed in the Weddell Sea for the winter SST data (Supplementary Fig. S9b and S11b). On the model-to-model agreement between COSMOS and PMIP, as with our sea ice simulations, we note higher alignment of our SST results with PMIP3 than with PMIP4, particularly at our study sites. For the comparison with PMIP3, the SST at our study sites is well outside the regions of model discord. In the case of PMIP4, agreement is larger for the winter season, with no overlap of regions of disagreement at study site PS118_63-1 and either no or mild overlap with study site PS67/219-1. Beyond the study site, similar to sea-ice cover, we notice greater model-to-model disagreement for the 21 ka BP time slice compared to the PI and 6 ka BP time slices. It is also worth noting that the SST model-to-model discord is greater in regions not covered by sea ice. For example, in Supplementary Fig. S9, areas with particularly low PMIP3 ensemble σ, such as the Weddell Sea, tend to exhibit higher simulated winter sea-ice cover as seen in Supplementary Fig. S5. Similarly, in Supplementary Fig. S8, regions with greater uncertainty in summer SST in the Weddell Sea correspond to smaller sea-ice cover (Supplementary Fig. S4).

3.4.3 Evaluation of COSMOS in comparison to PMIP models

In our assessment of the degree of agreement between COSMOS and PMIP3 simulations based on a 2σ threshold criterion, we observe generally good model-to-model agreement for both sea-ice cover and SST. The most significant discordance occurs close to, or north of, the sea ice border (15% isoline; see panel c in Supplementary Fig. S4 and S5, S8 and S9). Some slight disparity can be observed near our study locations: core PS118_63-1 for spring/summer sea-ice cover at PI (Supplementary Fig. S4.3c), core PS67/219-1 for both winter sea-ice cover at PI (Supplementary Fig. S5.3c) and for summer SST at 21 ka BP (Supplementary Fig. S8.1c). However, the study sites remain spatially distinct from regions where the model-to-model agreement falls outside the 2σ threshold criterion. The significantly large model-to-model disparity illustrated in the sea-ice cover and SST plots for 21 ka BP can be linked to a denser and more extensive seasonal sea-ice cover simulated by COSMOS compared to the PMIP3 ensemble (Fig. 5.4, Supplementary Fig. S4.1 and S5.1). This expansiveness of sea ice simulated by COSMOS is consistently observed across simulations for the PI and 6 ka BP time slices. We note that Lunt et al. (2013) have demonstrated that COSMOS exhibits a milder warm bias in the Southern Ocean compared to several other PMIP3-grade models. This suggests that the larger sea-ice cover in COSMOS, relative to PMIP3, may indeed reflect a strength of the COSMOS simulation rather than a weakness.

While a comparison of model biases of PMIP4/CMIP6 and of COSMOS with respect to observations has not been explicitly made, CMIP6 models, on which PMIP4 is built, tend to show a warm bias in the Southern Ocean (Luo et al., 2023). Our comparison of COSMOS and PMIP4 sea-ice cover and SST simulation ensembles reveals a model-to-model disagreement that surpasses the discord with PMIP3 (Supplementary Fig. S6c and S7c, S10c and S11c). Just as for PMIP3, COSMOS generally predicts a more expansive and denser sea-ice cover compared to PMIP4. Most significant differences between COSMOS and PMIP4 are found between 50-60ºS, and north of the sea ice border,

with some variations observed along coastal regions. Additionally, higher levels of model-to-model discordance are observed at our study sites for PMIP4 than for PMIP3. Nevertheless, some level of agreement can still be observed for specific study locations. For instance, there is agreement in core site PS118_63-1 for winter sea-ice cover and winter SST (Supplementary Fig. S7c and S11c), as well as at core site PS67/219-1 for winter sea-ice cover and winter SST at 21 ka BP (Supplementary S7.3c and S11.3c). In several cases of model-discord at core sites, the latter are in spatial proximity to regions where COSMOS and PMIP4 agree well with each other. We have shown that this COSMOS-to-PMIP4 contradictory outcome does not necessarily indicate a deficiency in the COSMOS model. Beyond different stages of model development, comparability of PMIP4 modeling protocols and boundary conditions to the PMIP3 framework, in which COSMOS has been employed for this study, is rather limited.

Despite different time slices being referenced for the Last Interglacial by COSMOS and PMIP4 ensemble, we still undertake a model-to-model comparison of PMIP4's 127 ka BP simulation against those of COSMOS's 128 and 125 ka BP simulations. The PMIP4 127 ka BP sea-ice cover shows better agreement with the 125 ka BP time slice of COSMOS. While larger disagreement is observed for the sea-ice cover simulated by COSMOS for 128 ka BP and for SST simulated by COSMOS at both 128 and 125 ka BP. COSMOS simulations for 125 and 128 ka BP are comparable to the PMIP4 127 ka BP time slice only to a very limited extent, owing to different forcings, boundary conditions, and modeling methodologies. Consequently, analysis of discrepancy between COSMOS and PMIP4 for the Last Interglacial should be viewed as an attempt to align our findings with the lig127k simulations available to the community, but not as an endorsement of any conclusion regarding COSMOS's skill in simulating the Last Interglacial climate.

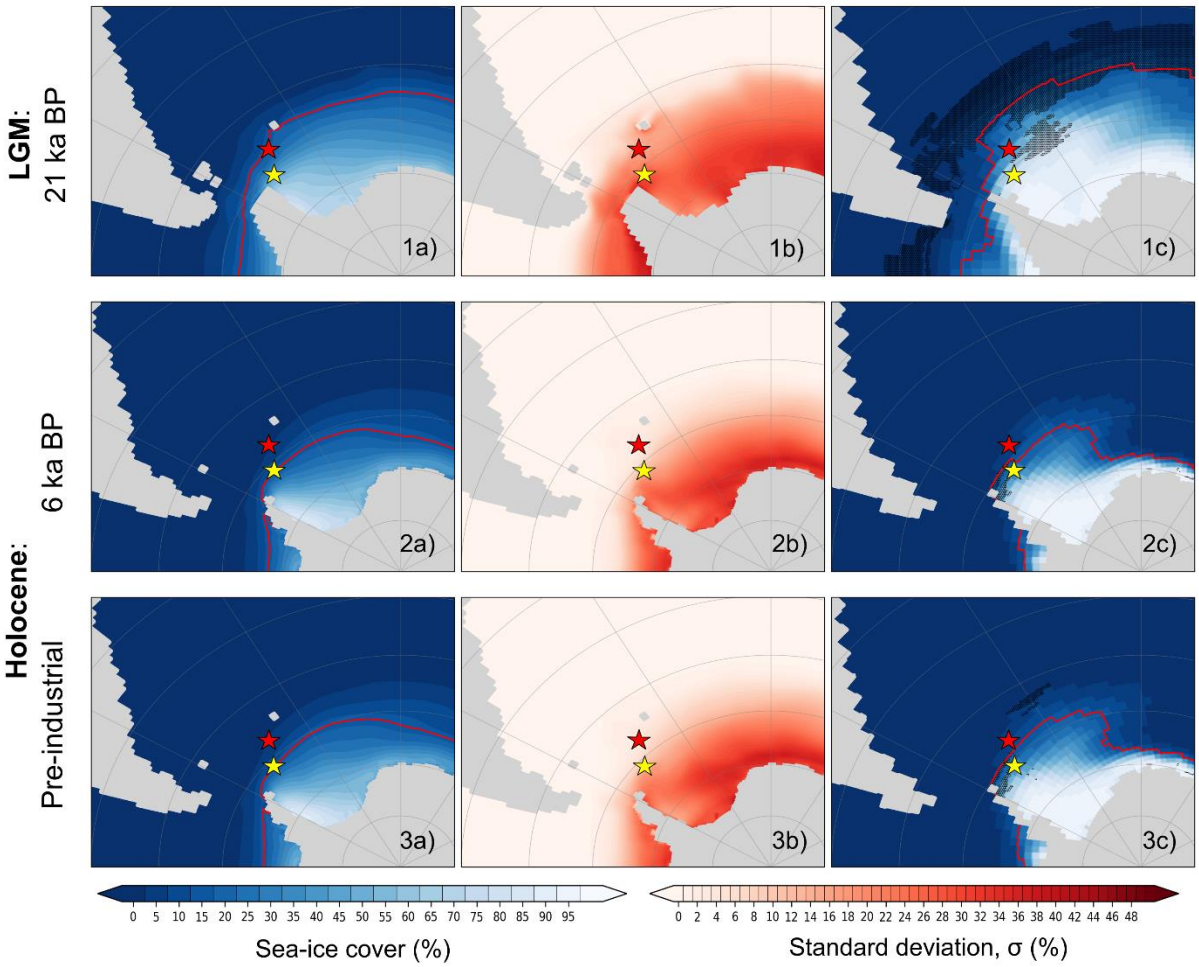

Supplementary Figure S4. The spring/summer (NDJFMA) sea-ice cover data simulated by PMIP3 models for three distinct time slices: 1) 21 ka BP, 2) 6 ka BP and 3) Pre-industrial. The visuals include a) the PMIP3 ensemble mean, b) standard deviation, σ, and c) agreement (within 2σ threshold) of the COSMOS and PMIP3 simulation results. Results that deviate from the PMIP3 ensemble by more than 2σ are highlighted by stippling. The red line in panels a and c depicts the sea-ice extent – defined by the 15% isoline for sea ice coverage. Locations of marine sediment cores are indicated with stars: PS118_63-1 (yellow) and PS67/219-1 (red).

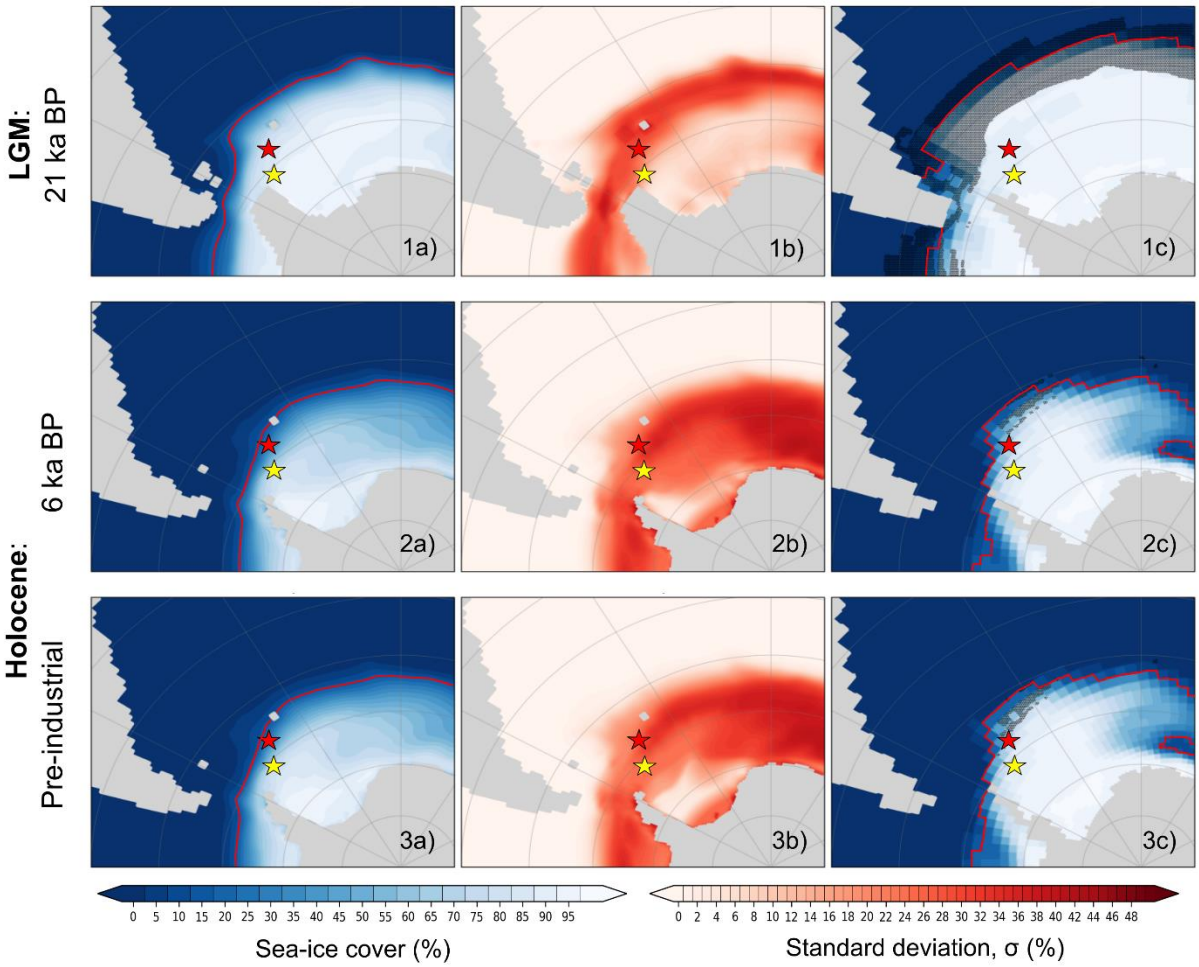

Supplementary Figure S5. The winter (ASO) sea-ice cover data simulated by PMIP3 models for three distinct time slices: 1) 21 ka BP, 2) 6 ka BP and 3) Pre-industrial. The visuals include a) the PMIP3 ensemble mean, b) standard deviation, σ, and c) agreement (within 2σ threshold) of the COSMOS and PMIP3 simulation results. Results that deviate from the PMIP3 ensemble by more than 2σ are highlighted by stippling. The red line in panels a and c depicts the sea-ice extent – defined by the 15% isoline for sea ice coverage. Locations of marine sediment cores are indicated with stars: PS118_63-1 (yellow) and PS67/219-1 (red).

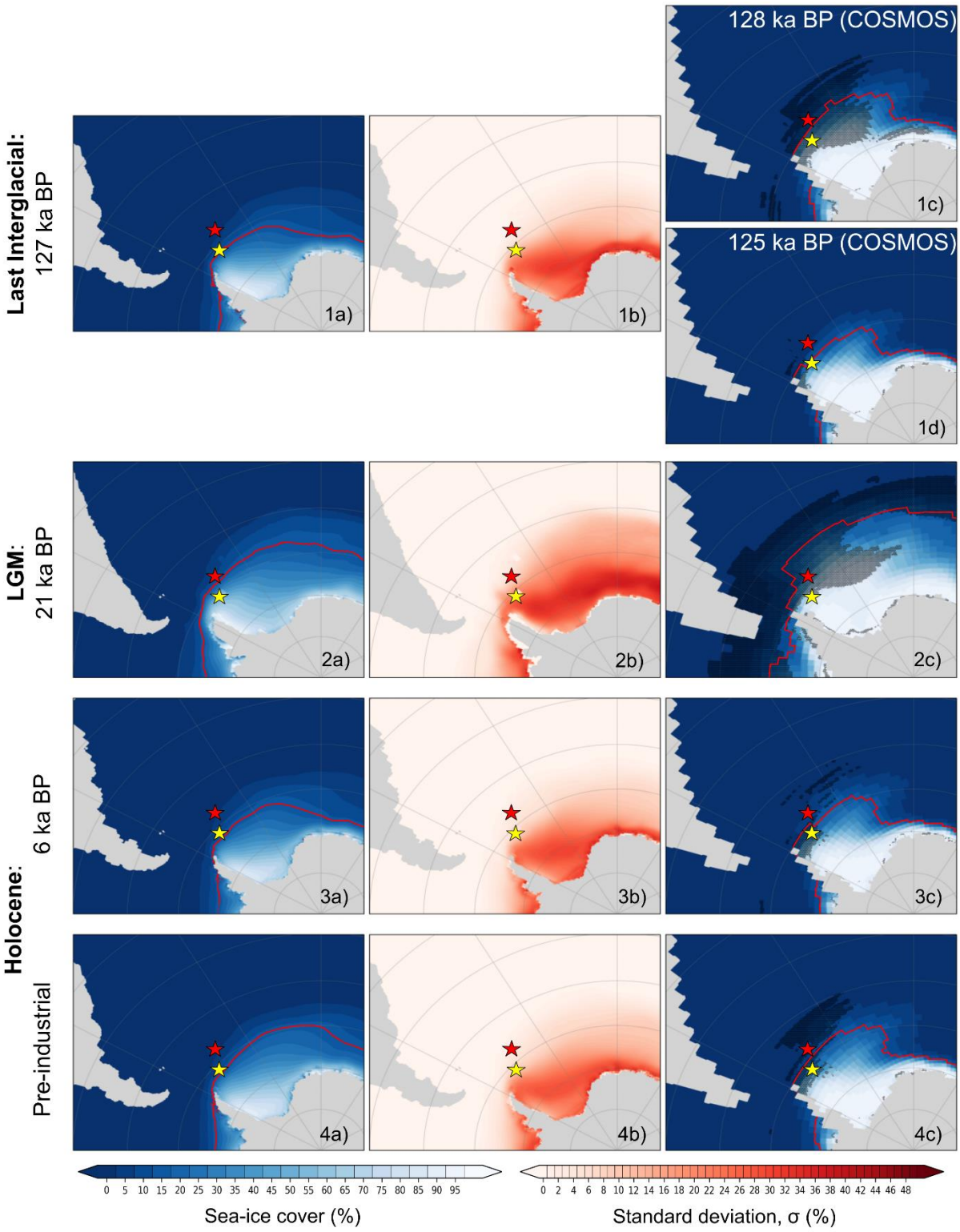

Supplementary Figure S6. The spring/summer (NDJFMA) sea-ice cover simulation from PMIP4 models for various time slices, mainly 1) 127 ka BP, 2) 21 ka BP, 3) 6 ka BP and 4) Pre-industrial. The visuals include a) the PMIP4 ensemble mean, b) standard deviation, σ, and c) agreement (within 2σ threshold) of the COSMOS and PMIP3 simulation results. Results that deviate from the PMIP3 ensemble by more than 2σ are highlighted by stippling. Red line in panels a and c indicates the sea-ice extent – defined by the 15% isoline for sea ice coverage. Locations of marine sediment cores are indicated with stars: PS118_63-1 (yellow) and PS67/219-1 (red).

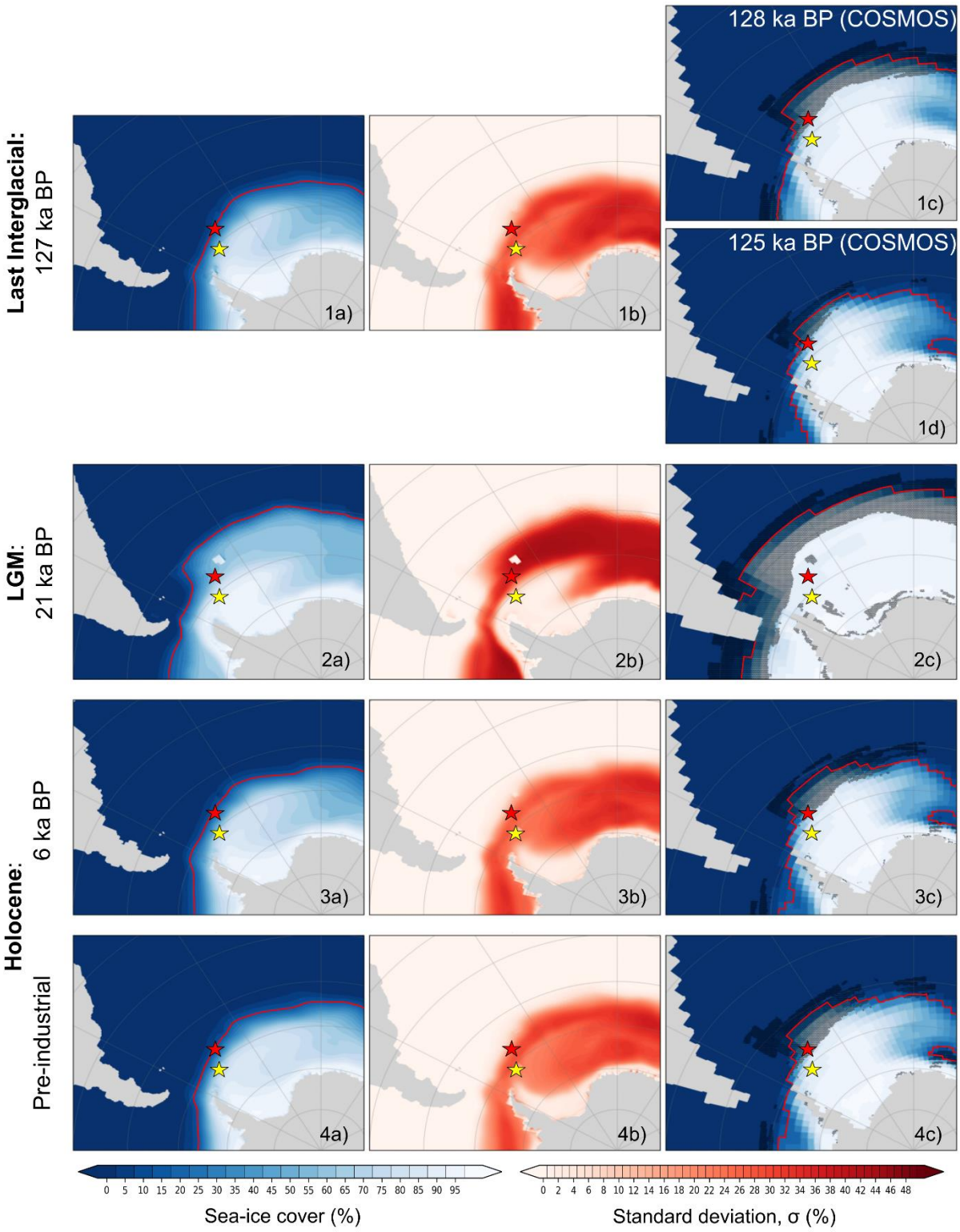

Supplementary Figure S7. The winter (ASO) sea-ice cover simulation from PMIP4 models for various time slices, mainly 1) 127 ka BP, 2) 21 ka BP, 3) 6 ka BP and 4) Pre-industrial. The visuals include a) the PMIP4 ensemble mean, b) standard deviation, σ, and c) agreement (within 2σ threshold) of the COSMOS and PMIP3 simulation results. Results that deviate from the PMIP3 ensemble by more than 2σ are highlighted by stippling. Red line in panels a and c indicates the sea-ice extent – defined by the 15% isoline for sea ice coverage. Locations of marine sediment cores are indicated with stars: PS118_63-1 (yellow) and PS67/219-1 (red).

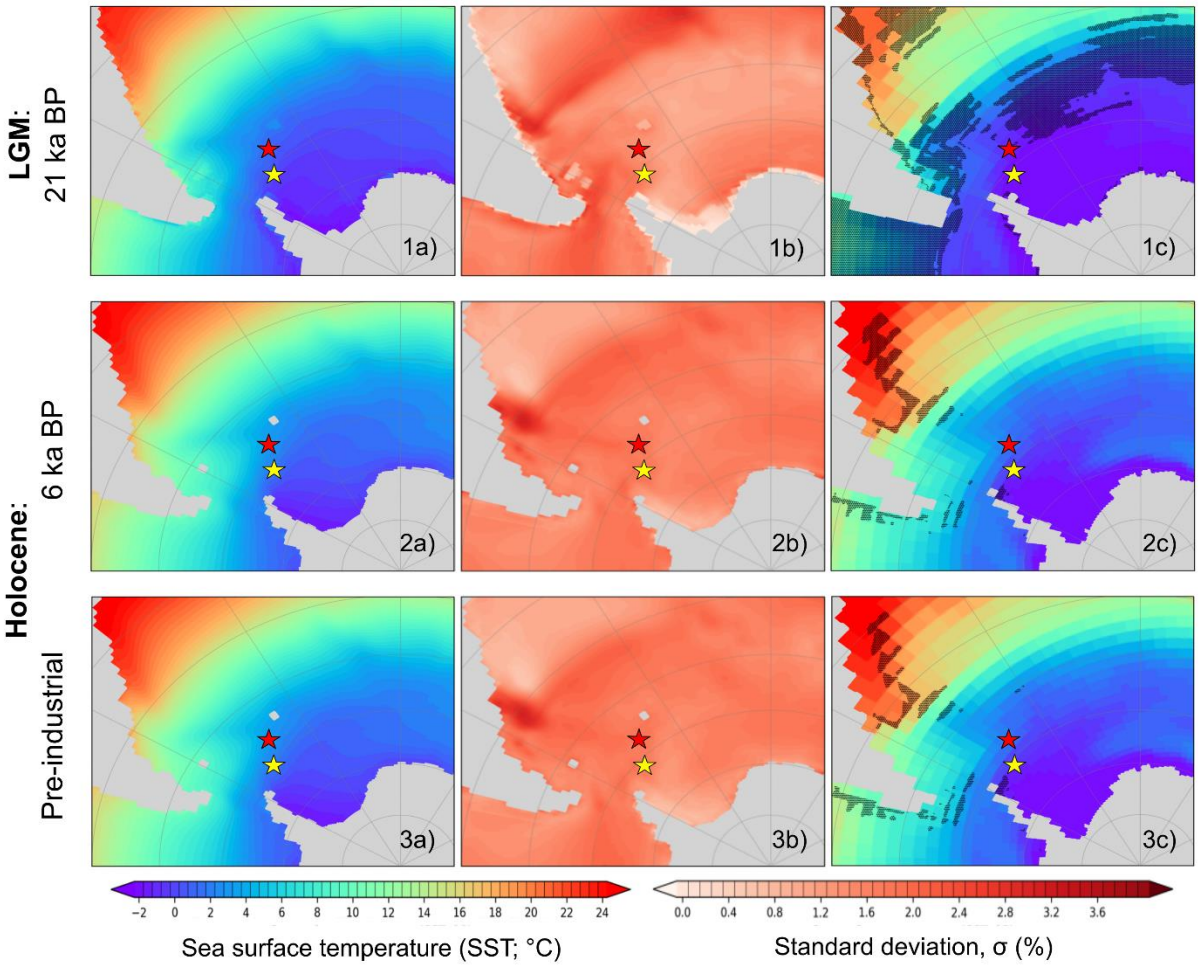

Supplementary Figure S8. The summer (DJF) sea surface temperature simulated by PMIP3 models for three distinct time slices: 1) 21 ka BP, 2) 6 ka BP and 3) Pre-industrial. The visuals include a) the PMIP3 ensemble mean, b) standard deviation, σ, and c) agreement (within 2σ threshold) of the COSMOS and PMIP3 simulation results. Results that deviate from the PMIP3 ensemble by more than 2σ are highlighted by stippling. Locations of marine sediment cores are indicated with stars: PS118_63-1 (yellow) and PS67/219-1 (red).

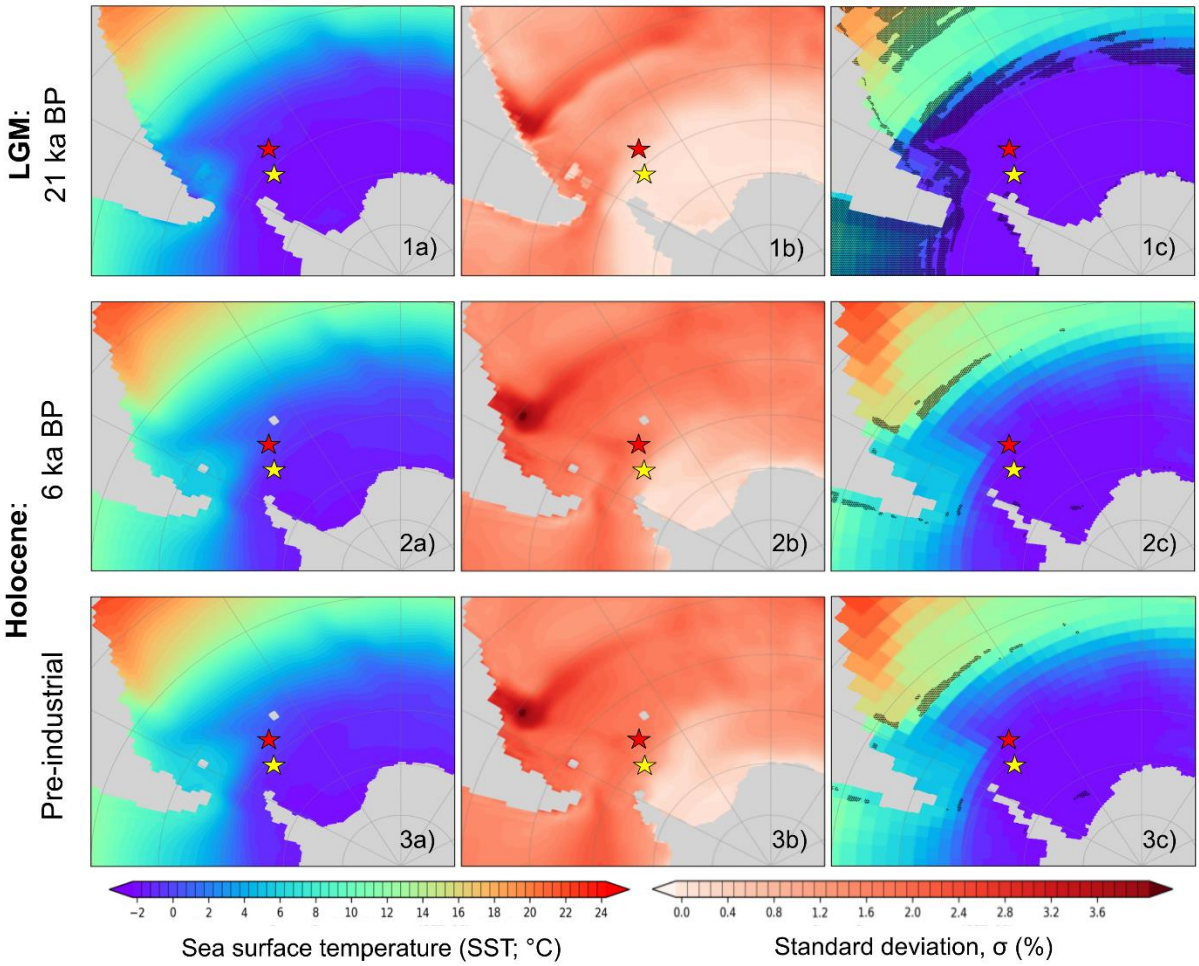

Supplementary Figure S9. The winter (JJA) sea surface temperature simulated by PMIP3 models for three distinct time slices: 1) 21 ka BP, 2) 6 ka BP and 3) Pre-industrial. The visuals include a) the PMIP3 ensemble mean, b) standard deviation, σ, and c) agreement (within 2σ threshold) of the COSMOS and PMIP3 simulation results. Results that deviate from the PMIP3 ensemble by more than 2σ are highlighted by stippling. Locations of marine sediment cores are indicated with stars: PS118_63-1 (yellow) and PS67/219-1 (red).

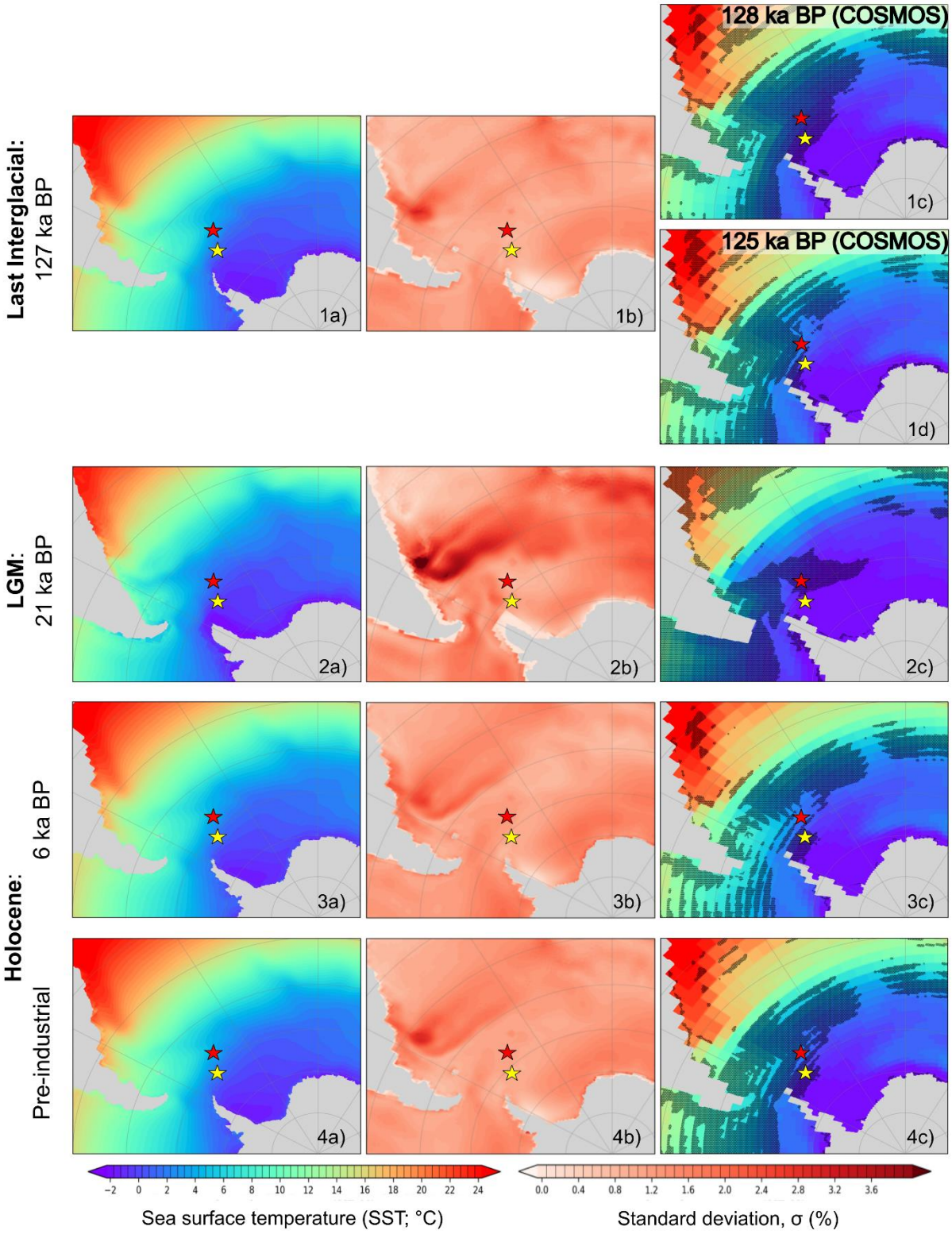

Supplementary Figure S10. The summer (DJF) sea surface temperature simulation from PMIP4 models for various time slices, mainly 1) 127 ka BP, 2) 21 ka BP, 3) 6 ka BP and 4) Pre-industrial. The visuals include a) the PMIP4 ensemble mean, b) standard deviation, σ, and c) agreement (within 2σ threshold) of the COSMOS and PMIP3 simulation results. Results that deviate from the PMIP3 ensemble by more than 2σ are highlighted by stippling. Locations of marine sediment cores are indicated with stars: PS118_63-1 (yellow) and PS67/219-1 (red).

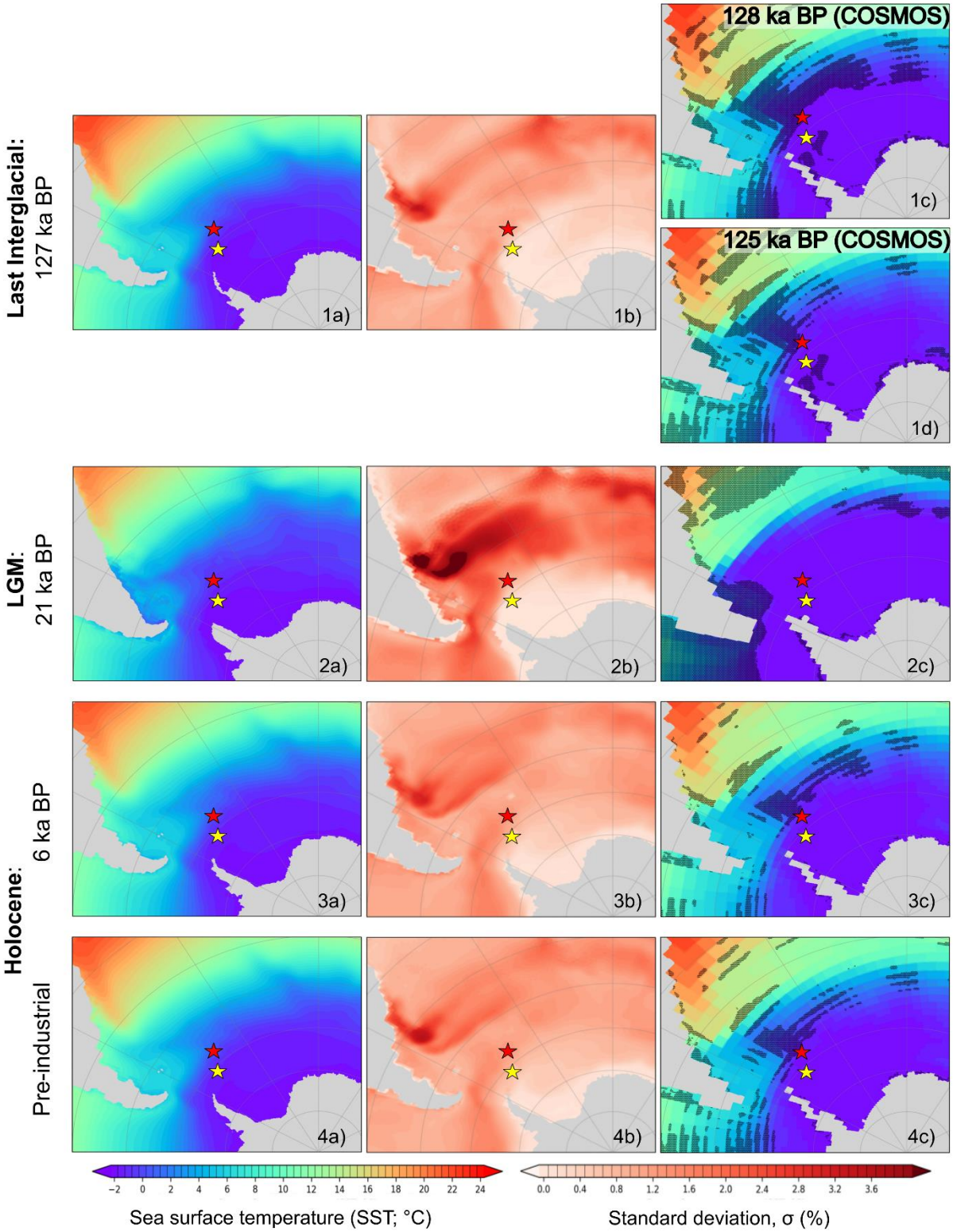

Supplementary Figure S11. The winter (JJA) sea surface temperature simulation from PMIP4 models for various time slices, mainly 1) 127 ka BP, 2) 21 ka BP, 3) 6 ka BP and 4) Pre-industrial. The visuals include a) the PMIP4 ensemble mean, b) standard deviation, σ, and c) agreement (within 2σ threshold) of the COSMOS and PMIP3 simulation results. Results that deviate from the PMIP3 ensemble by more than 2σ are highlighted by stippling. Locations of marine sediment cores are indicated with stars: PS118_63-1 (yellow) and PS67/219-1 (red).

Supplementary Table S3~~1~~. Boundary conditions and model forcings for COSMOS~~climate~~ simulations. We present: forcing values of eccentricity of the Earth's orbit (ecc), obliquity of the Earth's rotation axis (obld), longitude of the perihelion of the Earth's orbit (lonp); atmospheric concentrations of greenhouse gas species carbon dioxide (CO_2), methane, (CH_4), nitr~~u~~ous oxide (N_2O); where applicable, we provide references (ref) to employed paleogeography, orbital forcing, atmospheric greenhouse gas forcing, and to a previous study that provides additional details and description for each specific simulation~~previously described the simulation are provided~~.

Simulation	Orbital forcing				Greenhouse gas forcing				Paleography		Previously published by	
	ecc	obld (°)	Lonp (°)	ref	CO_2 (ppm)	CH_4 (ppb)	N_2O (ppb)	ref	reconstruction	ref	ref	name in ref
piControl	0.016724	23.4468	282.157	Berger (1978)	280	760	270	Crucifix et al. (2005)	—	—	Wei and Lohmann (2012)	CTL
mh6k	0.018682	24.1048	180.918	Berger (1978)	280	650	270	Crucifix et al. (2005) (as PMIP3 6ka)	—	—	Wei and Lohmann (2012)	H6K
lgm21k	0.018994	22.949	114.42	Braconnot and Kageyama (2015) and references therein	185	350	200	PMIP3 21ka Braconnot and Kageyama (2015) and references therein	PMIP3 21ka	Braconnot and Kageyama (2015) and references therein	Zhang et al. (2013)	LGMW
lig125k	0.040013	23.798	127.14	PMIP3 125ka Lunt et al. (2013)	275.938	640.417	263.084	PMIP3 125ka Lunt et al. (2013)	as *piControl*	—	this study	—
lig128k	0.039017	24.131	79.65	PMIP3 128ka Lunt et al. (2013)	275	709	512	128ka Lunt et al. (2013)	as *piControl*	—	this study	—
pgm140k	0.032796	23.4138	253.244	Berger et al. (1978)	185	350	200	as *lgm21k*	as *lgm21k*	as *lgm21k*	this study	—

Supplementary Table S4. Summary of the specific models (and their references; see remarks), variables, and data types utilize in the COSMOS to PMIP comparison in this study. Unless otherwise noted, we employ realization r1i1p1 for CMIP5/PMIP3 and r1i1p1f1 for CMIP6/PMIP4.

Simulations	Variables	Climate models	Type of data
CMIP5/PMIP3 ensemble models			
piControl	sic & tos	BCC-CSM1-1[1], CCSM4[2], CNRM-CM5[3], CSIRO-Mk3-6-0[4], CSIRO-Mk3L-1-2[5], EC-EARTH-2-2[6], GISS-E2-R[7], HadGEM2-CC[8], HadGEM2-ES[8], IPSL-CM5A-LR[9], MIROC-ESM[10], MPI-ESM-P[11], MRI-CGCM3[12]	monthly mean
	sic only	FGOALS-s2[13]	
	tos only	KCM1-2-2[14]	
mid-Holocene	sic & tos	BCC-CSM1-1[1], CCSM4[2], CNRM-CM5[3], CSIRO-Mk3-6-0[4], CSIRO-Mk3L-1-2[5], EC-EARTH-2-2[6], FGOALS-s2[13], GISS-E2-R[7], HadGEM2-CC[8], HadGEM2-ES[8], IPSL-CM5A-LR[9], MPI-ESM-P[11,15]	monthly mean
		MIROC-ESM[10], MRI-CGCM3[12]	climatological monthly mean
	tos only	KCM1-2-2[14]	monthly mean
lgm	sic & tos	CNRM-CM5[3], IPSL-CM5A-LR[9]	monthly mean
		CCSM4[2], GISS-E2-R[16], MIROC-ESM[10], MPI-ESM-P[11], MRI-CGCM3[12]	climatological monthly mean
CMIP6/PMIP4 ensemble models			
piControl	siconc & tos	ACCESS-ESM1-5[17], AWI-ESM-1-1-LR[18], CESM2[19], CESM2-FV2[20], CESM2-WACCM-FV2[21], CNRM-CM6-1[22], EC-Earth3-LR[23], FGOALS-g3[24], HadGEM3-GC31-LL[25], INM-CM4-8[26], IPSL-CM6A-LR[27], MIROC-ES2L[28], MPI-ESM1-2-LR[29], MRI-ESM2-0[30], NESM3[31], NorESM1-F[32], NorESM2-LM[33]	monthly mean
	tos only	FGOALS-f3-L[34] and GISS-E2-1-G[35]	
mid-Holocene	siconc & tos	ACCESS-ESM1-5[36], CESM2[37], EC-Earth3-LR[38], FGOALS-f3-L[39], FGOALS-g3[40], INM-CM4-8[41], IPSL-CM6A-LR[42], MIROC-ES2L[43], MPI-ESM1-2-LR[44], MRI-ESM2-0[45], NESM3[46], NorESM1-F[47], NorESM2-LM[48]	monthly mean
	tos only	GISS-E2-1-G[49] and HadGEM3-GC31-LL[50]	
lgm	siconc & tos	AWI-ESM-1-1-LR[51], MIROC-ES2L[52], MPI-ESM1-2-LR[53]	monthly mean
	tos only	INM-CM4-8[54]	
lig127k	siconc & tos	ACCESS-ESM1-5[55], AWI-ESM-1-1-LR[56], CESM2[57], CNRM-CM6-1[58], EC-Earth3-LR[59], FGOALS-g3[60], IPSL-CM6A-LR[61], NESM3[62], NorESM1-F[63], NorESM2-LM[64]	monthly mean
	siconc only	FGOALS-f3-L[65], MIROC-ES2L[66]	
	tos only	HadGEM3-GC31-LL[67]	

Remarks:
[1]Beijing Climate Center (BCC), China Meteorological Administration, China
[2]National Center for Atmospheric Research (NCAR), United States of America
[3]Centre National de Recherches Météorologiques/Centre Européen de Recherche et Formation Avancées en Calcul Scientifique (CNRM/CERFACS), France
[4]Commonwealth Scientific and Industrial Research Organization (CSIRO), Queensland Climate Change Centre of Excellence (QCCCE), Australia
[5]University of New South Wales (UNSW), Australia
[6]EC-EARTH consortium
[7]NASA Goddard Institute for Space Studies, United States of America
[8]Met Office Hadley Centre, United Kingdom
[9]Institut Pierre-Simon Laplace, France

[10]Japan Agency for Marine-Earth Science and Technology (JAMSTEC), Atmosphere and Ocean Research Institute (AORI, The University of Tokyo), National Institute for Environmental Studies (NIES), Japan
[11]Max Planck Institute for Meteorology (MPI-M), Germany
[12]Meteorological Research Institute (MRI), Japan
[13]Institute of Atmospheric Physics (IAP), Chinese Academy of Sciences (CAS), China
[14]GEOMAR Helmholtz Center for Ocean Research (GEOMAR), Christian-Albrechts University of Kiel (CAU), Germany
[15]For the CMIP5/PMIP3 *midHolocene* simulation, MPI-ESM-P provides only the variable tos as monthly mean model output, while the variable sic has been derived from monthly climatological mean available through ESGF.
[16]NASA Goddard Institute for Space Studies, United States of America; r1i1p150 used
[17]Ziehn et al. (2019)
[18]Danek et al. (2020)
[19]Danabasoglu et al. (2019)
[20]Danabasoglu (2019a)
[21]Danabasoglu (2019b)
[22]Voldoire (2018)
[23]EC-Earth Consortium (2019)
[24]Li (2019)
[25]Ridley et al. (2018)
[26]Volodin et al. (2019a)
[27]Boucher et al. (2018a)
[28]Hajima et al. (2019); r1i1p1f2 used
[29]Wieners et al. (2019)
[30]Yukimoto et al. (2019a)
[31]Cao and Wang (2019)
[32]Guo et al. (2019a)
[33]Seland et al. (2019)
[34]Yu (2019)
[35]Nasa Goddard Institute for Space Studies (2018)
[36]Brown et al. (2021)
[37]Danabasoglu (2019c)
[38]EC-Earth Consortium (2020a)
[39]Zheng and He (2019a)
[40]Zheng and Dong (2019a)
[41]Volodin et al. (2019b)
[42]Boucher et al. (2018b); r1i2p1f1 used
[43]Ohgaito et al. (2019a); r1i1p1f2 used
[44]Jungclaus et al. (2019a)
[45]Yukimoto et al. (2019b)
[46]Cao (2019a)
[47]Guo et al. (2019b)
[48]Zhang et al. (2019a)
[49]Nasa Goddard Institute for Space Studies (2019)
[50]Williams et al. (2021a)
[51]Shi et al. (2020a)
[52]Ohgaito et al. (2019b); r1i1p1f2 used
[53]Jungclaus et al. (2019b)
[54]Volodin et al. (2019c)
[55]Yeung et al. (2019)
[56]Shi et al. (2020b)
[57]Danabasoglu (2019d)
[58]Voldoire (2020); r1i1p1f2 used
[59]Earth Consortium (2020b)
[60]Zheng and Dong (2019b)
[61]Boucher et al. (2018c)
[62]Cao (2019b)
[63]Guo et al. (2019c)
[64]Zhang et al. (2019b)
[65]Zheng and He (2019b)
[66]O'ishi et al. (2019); r1i1p1f2 used
[67]Williams et al. (2021b)

Supplementary Table S5. This table summarizes the simulated data from (a) CMIP5 and (b) CMIP6 frameworks available on the ESGF. Simulations are grouped, in columns, by the studied time slices used in this work, with the CMIP and PMIP simulation names given in brackets where such simulations are available. This table illustrates sparseness of coverage relevant to our study by ensembles from the community. Models with at least one relevant dataset are highlighted in green. In our analysis we only considered models that provide data for at least one additional time slice beyond PI. Note that relevant simulations and variables may not necessarily overlap, and that lengths of available time series differ between models. In cases where only one specific variable (i.e., sea surface temperature or sea-ice cover only) is available, this is indicated in the table (e.g., "sic only" for availability of variable sic and unavailability of variable tos). Data from models that were unavailable due to prolonged server downtime are marked in orange. Please refer to the remarks for further information on data availability. Data accessed from ESGF (https://esgf-data.dkrz.de/search/cmip6-dkrz/; https://esgf-data.dkrz.de/search/esgf-dkrz/; accessed 3rd of April, 2024).

a) Simulations related to CMIP5 and PMIP3

	PI (*piControl*)	6 ka BP (*midHolocene*)	21 ka BP (*lgm*)	125 ka BP	127 ka BP	128 ka BP	140 ka BP
ACCESS1.0							
ACCESS1.3							
BCC-CSM1.1							
CCSM4							
CMCC-CESM							
CMCC-CM							
CMCC-CMS							
CNRM-CM5							
CNRM-CM5-2							
CSIRO-Mk3.6.0							
CSIRO-Mk3L-1-2							
CanESM2							
EC-EARTH							
EC-EARTH-2-2							
FGOALS-g2							
FGOALS-s2	sic only[1]						
GISS-E2-H							
GISS-E2-H-CC							
GISS-E2-R							
GISS-E2-R-CC							
HadCM3							
HadGEM2-AO							
HadGEM2-CC							
HadGEM2-ES							
INM-CM4							
IPSL-CM5A-LR							
IPSL-CM5A-MR							
IPSL-CM5B-LR							
KCM1-2-2	tos only[2]	tos only[2]					
MIROC-ESM							
MIROC-ESM-CHEM							
MIROC4h							
MIROC5							
MPI-ESM-LR							
MPI-ESM-MR							
MPI-ESM-P							
MRI-CGCM3							
NorESM1-M							
NorESM1-ME							
bccr bcm2 0							
cccma cgcm3 1							
cccma cgcm3 1 t63							

a) Simulations related to CMIP5 and PMIP3 (cont.)							
	PI (*piControl*)	6 ka BP (*midHolocene*)	21 ka BP (*lgm*)	125 ka BP	127 ka BP (*lig127k*)	128 ka BP	140 ka BP
cnrm cm3							
csiro mk3 0							
csiro mk3 5							
gfdl cm2 0							
gfdl cm2 1							
giss aom							
giss model e h							
giss model e r							
iap fgoals1 0 g							
ingv echam4							
inmcm3 0							
ipsl cm4							
miroc3 2 hires							
miroc3 2 medres							
miub echo g							
mri cgcm2 3 2a							
ncar ccsm3 0							
ncar pcm1							
ukmo hadcm3							
ukmo hadgem1							

b) Simulations related to CMIP6 and PMIP4

	PI (*piControl*)	6 ka BP (*midHolocene*)	21 ka BP (*lgm*)	125 ka BP	127 ka BP (*lig127k*)	128 ka BP	140 ka BP
ACCESS-CM2							
ACCESS-ESM1-5							
AWI-CM-1-1-MR							
AWI-ESM-1-1-LR							
BCC-CSM2-MR							
BCC-ESM1							
CAMS-CSM1-0							
CAS-ESM2-0							
CESM2							
CESM2-FV2			offline[4]				
CESM2-WACCM							
CESM2-WACCM-FV2			offline[5]				
CIESM							
CMCC-CM2-SR5							
CMCC-ESM2							
CNRM-CM6-1							
CNRM-CM6-1-HR							
CNRM-ESM2-1							
CanESM5							
CanESM5-1							
CanESM5-CanOE							
E3SM-1-0							
E3SM-1-1							
E3SM-1-1-ECA							
E3SM-2-0							
E3SM-2-0-NARRM							
EC-Earth3							
EC-Earth3-AerChem							
EC-Earth3-CC							
EC-Earth3-LR							
EC-Earth3-Veg							
EC-Earth3-Veg-LR							

b) Simulations related to CMIP6 and PMIP4 (cont.)							
	PI (*piControl*)	6 ka BP (*midHolocene*)	21 ka BP (*lgm*)	125 ka BP	127 ka BP (*lig127k*)	128 ka BP	140 ka BP
FGOALS-f3-L	tos only[6]				siconc only[7]		
FGOALS-g3							
FIO-ESM-2-0							
GFDL-ESM4							
GISS-E2-1-G	tos only[8]	tos only[9]			offline[10]		
GISS-E2-1-H							
GISS-E2-2-G							
GISS-E2-2-H							
HadGEM3-GC31-LL		tos only[11]			tos only[12]		
HadGEM3-GC31-MM							
ICON-ESM-LR							
IITM-ESM							
INM-CM4-8			tos only[13]				
INM-CM5-0							
IPSL-CM5A2-INCA							
IPSL-CM6A-LR							
IPSL-CM6A-MR1							
KIOST-ESM							
MCM-UA-1-0							
MIROC-ES2H							
MIROC-ES2L					siconc only[14]		
MIROC6							
MPI-ESM-1-2-HAM							
MPI-ESM1-2-HR							
MPI-ESM1-2-LR							
MRI-ESM2-0							
NESM3							
NorCPM1							
NorESM1-F							
NorESM2-LM							
NorESM2-MM							
SAM0-UNICON							
TaiESM1							
UKESM1-0-LL							
UKESM1-1-LL							

Remarks:

[1] For simulation *piControl*, model FGOALS-s2 provides both variables tos and sic; yet, data for variable tos has not been accessible via ESGF due to unavailability of data node esg.lasg.ac.cn that, at the time of data access, provides the only copy of that data.

[2] For simulation *piControl*, model KCM1-2-2 only provides via ESGF data for variable tos, but not for variable sic.

[3] For simulation *midHolocene*, model KCM1-2-2 only provides via ESGF data for variable tos, but not for variable sic.

[4] For simulation *lgm*, model CESM-FV2 provides both variables tos and sic; yet, for both variables data has not been accessible via ESGF due to unavailability of data nodes esgf-data.ucar.edu and esgf-data1.llnl.gov that, at the time of data access, provide the only copy of that data.

[5] For simulation *lgm*, model CESM-WACCM-FV2 provides both variables tos and sic; yet, for both variables data has not been accessible via ESGF due to unavailability of data nodes esgf-data.ucar.edu and esgf-data1.llnl.gov that, at the time of data access, provide the only copy of that data.

[6] For simulation *piControl*, model FGOALS-f3-L only provides via ESGF data for variable tos, but not for variable siconc.

[7] For simulation *lig127k*, model FGOALS-f3-L provides both variables tos and siconc; yet, data for variable tos has not been accessible via ESGF due to unavailability of data nodes esg.lasg.ac.cn and esgf-data1.llnl.gov that, at the time of data access, provide the only copy of that data.

[8] For simulation *piControl*, model GISS-E2-1-G only provides via ESGF data for variable tos, but not for variable siconc.

[9] For simulation *midHolocene*, model GISS-E2-1-G only provides via ESGF data for variable tos, but not for variable siconc.

[10] For simulation *lig127k*, model GISS-E2-1-G provides both variables tos and siconc; yet, for both variables data has not been accessible via ESGF due to unavailability of data nodes esgf-data1.llnl.gov, dpesgf03.nccs.nasa.gov, and esgf-data04.diasjp.net that, at the time of data access, provide the only copy of that data.

[11] For simulation *midHolocene*, model HadGEM3-GC31-LL only provides via ESGF data for variable tos, but not for variable siconc.

[12] For simulation *lig127k*, model HadGEM3-GC31-LL only provides via ESGF data for variable tos, but not for variable siconc.

[13] For simulation *lgm*, model INM-CM4-8 only provides via ESGF data for variable tos, but not for variable siconc.

[14] For simulation *lig127k*, model MIROC-ES2L provides both variables tos and siconc; yet, data for variable tos has not been accessible via ESGF due to unavailability of data nodes esgf-data02.diasjp.net and esgf-data1.llnl.gov that, at the time of data access, provide the only copy of that data.

S4: Productivity signals

The concentration of total isoprenoid glycerol dialkyl glycerol tetraether lipids (isoGDGTs) and hydroxylated (OH)-GDGTs, synthetized from marine archaea (Schouten et al., 2013), varies between 1.36-358.32 µg/g OC and 0.01-105.71 µg/g OC, respectively (Supplementary Fig. S4d). The concentration of total branched GDGTs (brGDGTs), mainly derived from terrestrial bacteria or eukaryotes in soils and peats (Hopmans et al., 2004), ranges between 0.11 and 7.34 µg/g OC (Supplementary Fig. S4e). Lastly, the concentration of phytosterols fluctuates between 0-54.28 µg/g OC (Brassicasterol) and 0-8.51 µg/g OC (Dinosterol; Supplementary Fig. S4f). The opal ($bSiO_2$) and brassicasterol profiles (Supplementary Fig. S4b and f), often used as diatom productivity indicators, exhibit contrasting trends, especially between 140-110 ka BP. This discrepancy likely arises from the limited presence of brassicasterol-producing diatoms in the area, further affected by preferential growth conditions and preservation effects. As a result, the brassicasterol-producing diatoms signal is consistently attenuated within the overall opal signal (Badejo et al., 2017; Cavagna et al., 2013).

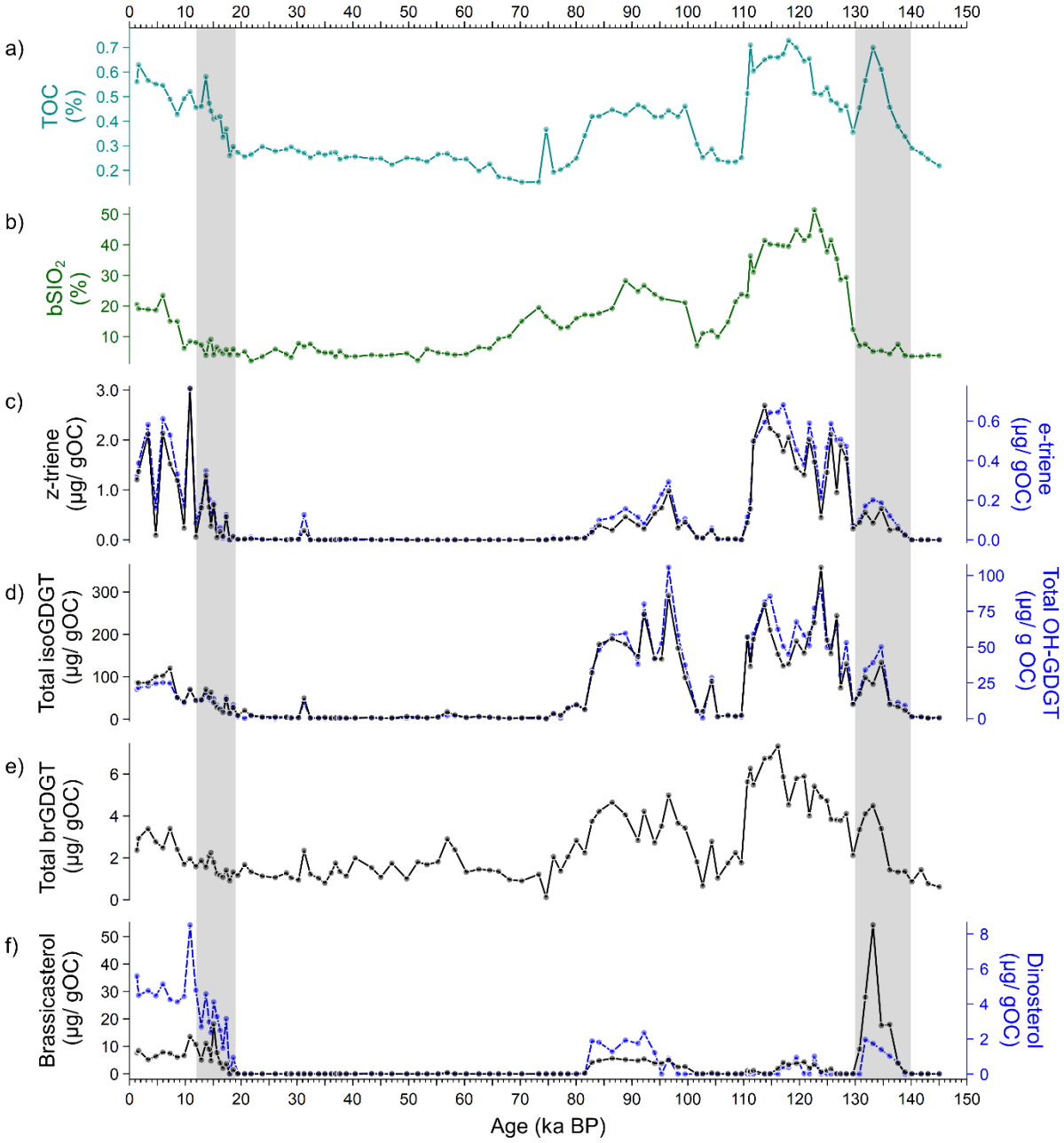

Supplementary Figure S12. Plots of organic matter signals from core PS118_63-1: a) TOC, b) biogenic opal, c) HBI-based phytoplankton, d) total isoprenoid-GDGT and total hydroxylated-GDGT, e) total branched-GDGT and f) phytosterols. Shaded intervals indicate Termination 1 and Termination II, respectively.

S5: TEX_{86}^{L}-derived subsurface ocean temperature and GDGT-related indices

The TEX_{86}^{L}-derived subsurface ocean temperature (OT; Supplementary Fig. S5a) shows a temperature range between -2.6 and 1.0°C at the core site. However, a review of the GDGT-related indices (Supplementary Fig. S5b-e) provide strong evidence of factors that result in biasness in our TEX_{86}^{L}-based temperature reconstruction, especially during MIS 2-4, 5d and 6. For example, an isoGDGT-[2]/[3] ratio greater than five indicates contribution from deep-dwelling archaea (>1000 m water depth), which are regulated by processes different than that of their surface water counterparts (Kim et al., 2015; Taylor et al., 2013). A higher abundance of isoGDGT-0 relative to crenarchaeol (%isoGDGT-0 value > 67%) also suggests a methanogenic source for the isoGDGT-0 (Inglis et al., 2015). Lastly, values of ΔRI and BIT indices that are higher than 0.3, imply inputs from potential nonthermal influences and/or terrestrial origin, respectively (Fietz et al., 2016; Park, 2019; Weijers et al., 2006; Zhang et al., 2016).

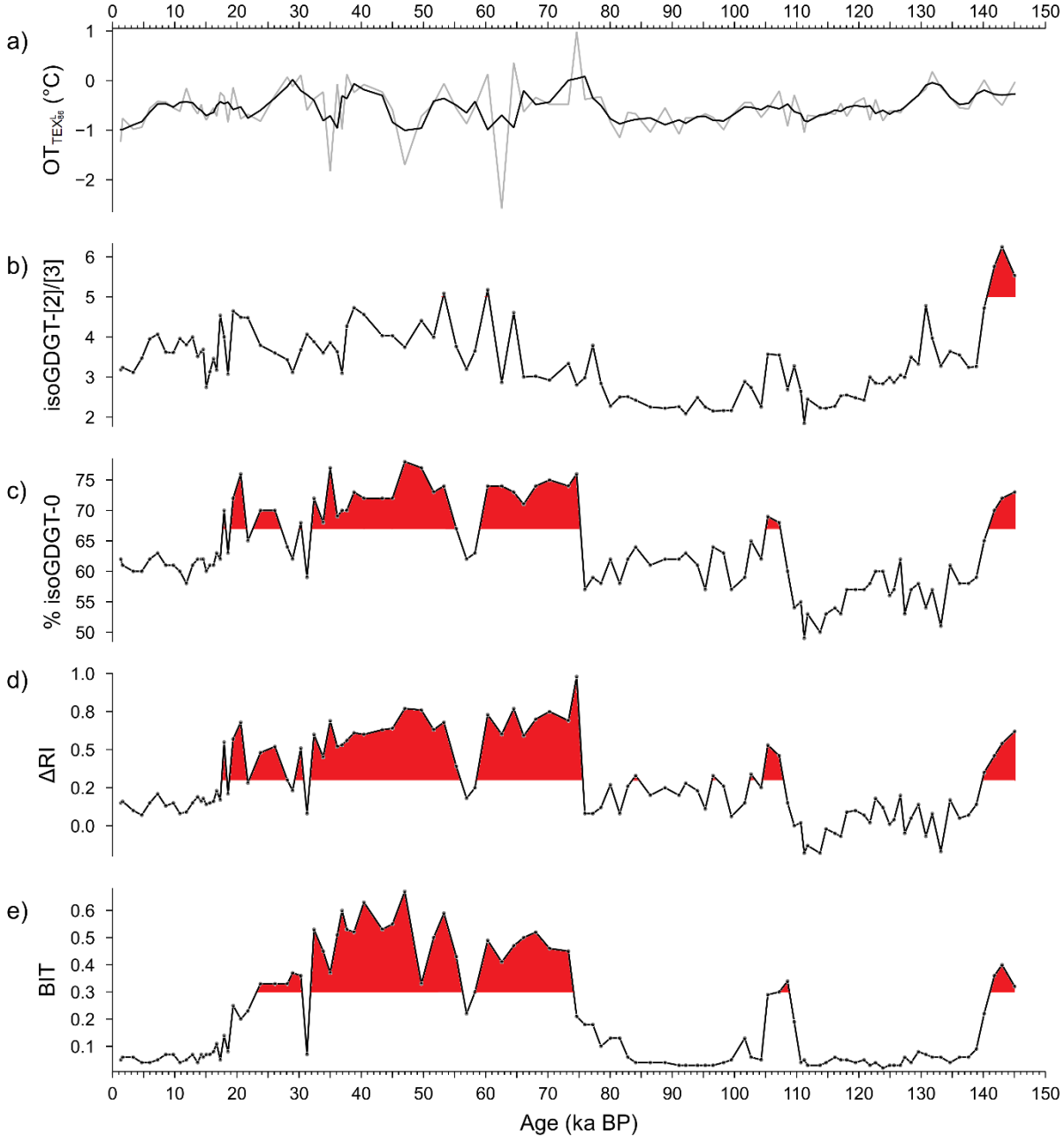

Supplementary Figure S13. Records of a) TEX_{86}^{L}-derived ocean temperature and respective isoGDGT-related indices: b) isoGDGT [2]/[3], c) %isoGDGT-0, d) delta ring index and e) BIT for core PS118_63-1. Intervals with strong non-thermal influences are highlighted in red on the various index curves: isoGDGT [2]/[3] > 5.0, %isoGDGT-0 > 67%, ΔRI and BIT > 0.3.

References

Appleby, P. G. and Oldfield, F.: The calculation of lead-210 dates assuming a constant rate of supply of unsupported 210Pb to the sediment, Catena, 5, 1-8, https://doi.org/10.1016/S0341-8162(78)80002-2, 1978.

Badejo, A. O., Seo, I., Kim, W., Hyeong, K., and Ju, S.-J.: Effect of eolian Fe-supply change on the phytoplankton productivity and community in central equatorial Pacific Ocean during the Pleistocene: A lipid biomarker approach, Organic Geochemistry, 112, 170-176, https://doi.org/10.1016/j.orggeochem.2017.07.010, 2017.

Bakker, P., Masson-Delmotte, V., Martrat, B., Charbit, S., Renssen, H., Gröger, M., Krebs-Kanzow, U., Lohmann, G., Lunt, D. J., Pfeiffer, M., Phipps, S. J., Prange, M., Ritz, S. P., Schulz, M., Stenni, B., Stone, E. J., and Varma, V.: Temperature trends during the Present and Last Interglacial periods – a multi-model-data comparison, Quaternary Science Reviews, 99, 224-243, https://doi.org/10.1016/j.quascirev.2014.06.031, 2014.

Berger, A.: Long-Term Variations of Daily Insolation and Quaternary Climatic Changes, Journal of Atmospheric Sciences, 35, 2362-2367, https://doi.org/10.1175/1520-0469(1978)035<2362:LTVODI>2.0.CO;2, 1978.

Bianchi, C. and Gersonde, R.: The Southern Ocean surface between Marine Isotope Stages 6 and 5d: Shape and timing of climate changes, Palaeogeography, Palaeoclimatology, Palaeoecology, 187, 151-177, https://doi.org/10.1016/S0031-0182(02)00516-3, 2002.

Blaauw, M. and Christen, J. A.: Flexible paleoclimate age-depth models using an autoregressive gamma process, Bayesian Analysis, 6, 457-474, 418, https://doi.org/10.1214/11-BA618, 2011.

Boucher, O., Denvil, S., Levavasseur, G., Cozic, A., Caubel, A., Foujols, M.-A., Meurdesoif, Y., Braconnot, P., Contoux, C., Kageyama, M., and Khodri, M.: IPSL IPSL-CM6A-LR model output prepared for CMIP6 PMIP midHolocene, Version 20180926, Earth System Grid Federation, https://doi.org/10.22033/ESGF/CMIP6.5229, 2018b.

Boucher, O., Denvil, S., Levavasseur, G., Cozic, A., Caubel, A., Foujols, M.-A., Meurdesoif, Y., Braconnot, P., Contoux, C., Kageyama, M., and Khodri, M.: IPSL IPSL-CM6A-LR model output prepared for CMIP6 PMIP lig127k, Version 20180926, Earth System Grid Federation, https://doi.org/10.22033/ESGF/CMIP6.5228, 2018c.

Boucher, O., Denvil, S., Levavasseur, G., Cozic, A., Caubel, A., Foujols, M.-A., Meurdesoif, Y., Cadule, P., Devilliers, M., Ghattas, J., Lebas, N., Lurton, T., Mellul, L., Musat, I., Mignot, J., and Cheruy, F.: IPSL IPSL-CM6A-LR model output prepared for CMIP6 CMIP piControl, Earth System Grid Federation, Version 20200326, Earth System Grid Federation, https://doi.org/10.22033/ESGF/CMIP6.5251, 2018a.

Braconnot, P. and Kageyama, M.: Shortwave forcing and feedbacks in Last Glacial Maximum and Mid-Holocene PMIP3 simulations, Philosophical Transactions of the Royal Society A: Mathematical, Physical and Engineering Sciences, 373, 20140424, https://doi.org/10.1098/rsta.2014.0424, 2015.

Braconnot, P., Harrison, S. P., Kageyama, M., Bartlein, P. J., Masson-Delmotte, V., Abe-Ouchi, A., Otto-Bliesner, B., and Zhao, Y.: Evaluation of climate models using palaeoclimatic data, Nature Climate Change, 2, 417-424, https://doi.org/10.1038/nclimate1456, 2012.

Brown, J., Yeung, N., Menviel, L., Meissner, K., Ziehn, T., Chamberlain, M., Mackallah, C., Druken, K., and Ridzwan, S. M.: CSIRO ACCESS-ESM1.5 model output prepared for CMIP6 PMIP midHolocene, Version 20210422, Earth System Grid Federation, https://doi.org/10.22033/ESGF/CMIP6.13704, 2021.

Burls, N. J., Bradshaw, C. D., De Boer, A. M., Herold, N., Huber, M., Pound, M., Donnadieu, Y., Farnsworth, A., Frigola, A., Gasson, E., von der Heydt, A. S., Hutchinson, D. K., Knorr, G., Lawrence, K. T., Lear, C. H., Li, X., Lohmann, G., Lunt, D. J., Marzocchi, A., Prange, M., Riihimaki, C. A., Sarr,

A.-C., Siler, N., and Zhang, Z.: Simulating Miocene Warmth: Insights From an Opportunistic Multi-Model Ensemble (MioMIP1), Paleoceanography and Paleoclimatology, 36, e2020PA004054, https://doi.org/10.1029/2020PA004054, 2021.

Butzin, M., Köhler, P., and Lohmann, G.: Marine radiocarbon reservoir age simulations for the past 50,000 years, Geophysical Research Letters, 44, 8473-8480, https://doi.org/10.1002/2017GL074688, 2017.

Cao, J.: NUIST NESMv3 model output prepared for CMIP6 PMIP midHolocene, Version 20190926, Earth System Grid Federation, https://doi.org/10.22033/ESGF/CMIP6.8773, 2019a.

Cao, J.: NUIST NESMv3 model output prepared for CMIP6 PMIP lig127k, Version 20190927, Earth System Grid Federation, https://doi.org/10.22033/ESGF/CMIP6.8772, 2019b.

Cao, J. and Wang, B.: NUIST NESMv3 model output prepared for CMIP6 CMIP piControl, Version 20190704, Earth System Grid Federation, https://doi.org/10.22033/ESGF/CMIP6.8776, 2019.

Cavagna, A. J., Dehairs, F., Bouillon, S., Woule-Ebongué, V., Planchon, F., Delille, B., and Bouloubassi, I.: Water column distribution and carbon isotopic signal of cholesterol, brassicasterol and particulate organic carbon in the Atlantic sector of the Southern Ocean, Biogeosciences, 10, 2787-2801, https://doi.org/10.5194/bg-10-2787-2013, 2013.

Crucifix, M., Braconnot, P., Harrison, S. P., and Otto-Bliesner, B.: Second phase of paleoclimate modelling intercomparison project, Eos, Transactions American Geophysical Union, 86, 264-264, https://doi.org/10.1029/2005EO280003, 2005.

Dallmeyer, A., Claussen, M., Wang, Y., and Herzschuh, U.: Spatial variability of Holocene changes in the annual precipitation pattern: a model-data synthesis for the Asian monsoon region, Climate Dynamics, 40, 2919-2936, https://doi.org/10.1007/s00382-012-1550-6, 2013.

Dallmeyer, A., Claussen, M., Fischer, N., Haberkorn, K., Wagner, S., Pfeiffer, M., Jin, L., Khon, V., Wang, Y., and Herzschuh, U.: The evolution of sub-monsoon systems in the Afro-Asian monsoon region during the Holocene– comparison of different transient climate model simulations, Clim. Past, 11, 305-326, https://doi.org/10.5194/cp-11-305-2015, 2015.

Danabasoglu, G.: NCAR CESM2-FV2 model output prepared for CMIP6 CMIP piControl, Version 20191120, Earth System Grid Federation, https://doi.org/10.22033/ESGF/CMIP6.11301, 2019a.

Danabasoglu, G.: NCAR CESM2-WACCM-FV2 model output prepared for CMIP6 CMIP piControl, Version 20191120, Earth System Grid Federation, https://doi.org/10.22033/ESGF/CMIP6.11302, 2019b.

Danabasoglu, G.: NCAR CESM2 model output prepared for CMIP6 PMIP midHolocene, Version 20190923, Earth System Grid Federation, https://doi.org/10.22033/ESGF/CMIP6.7674, 2019c.

Danabasoglu, G.: NCAR CESM2 model output prepared for CMIP6 PMIP lig127k, Version 20190923, Earth System Grid Federation, https://doi.org/10.22033/ESGF/CMIP6.7673, 2019d.

Danabasoglu, G., Lawrence, D., Lindsay, K., Lipscomb, W., and Strand, G.: NCAR CESM2 model output prepared for CMIP6 CMIP piControl. Version 20190320, Earth System Grid Federation, https://doi.org/10.22033/ESGF/CMIP6.7733, 2019.

Danek, C., Shi, X., Stepanek, C., Yang, H., Barbi, D., Hegewald, J., and Lohmann, G.: AWI AWI-ESM1.1LR model output prepared for CMIP6 CMIP piControl, Version 20200212, Earth System Grid Federation, https://doi.org/10.22033/ESGF/CMIP6.9335, 2020.

Earth Consortium: EC-Earth-Consortium EC-Earth3-LR model output prepared for CMIP6 CMIP piControl, Version 20200919, Earth System Grid Federation, https://doi.org/10.22033/ESGF/CMIP6.4847, 2019.

575 Earth Consortium: EC-Earth-Consortium EC-Earth3-LR model output prepared for CMIP6 PMIP
576 midHolocene, Version 20200919, Earth System Grid Federation,
577 https://doi.org/10.22033/ESGF/CMIP6.4801, 2020a.

578 Earth Consortium: EC-Earth-Consortium EC-Earth3-LR model output prepared for CMIP6 PMIP
579 lig127k, Version 20200919, Earth System Grid Federation,
580 https://doi.org/10.22033/ESGF/CMIP6.4798, 2020b.

581 Eyring, V., Bony, S., Meehl, G. A., Senior, C. A., Stevens, B., Stouffer, R. J., and Taylor, K. E.:
582 Overview of the Coupled Model Intercomparison Project Phase 6 (CMIP6) experimental design and
583 organization, Geosci. Model Dev., 9, 1937-1958, https://doi.org/10.5194/gmd-9-1937-2016, 2016.

584 Fietz, S., Ho, S. L., Huguet, C., Rosell-Melé, A., and Martínez-García, A.: Appraising GDGT-based
585 seawater temperature indices in the Southern Ocean, Organic Geochemistry, 102, 93-105,
586 https://doi.org/10.1016/j.orggeochem.2016.10.003, 2016.

587 Geibert, W., Stimac, I., Rutgers Van Der Loeff, M., and Kuhn, G.: Dating Deep-Sea Sediments With
588 230Th Excess Using a Constant Rate of Supply Model, Paleoceanography and Paleoclimatology, 34,
589 1895-1912, https://doi.org/10.1029/2019PA003663, 2019.

590 Gierz, P., Werner, M., and Lohmann, G.: Simulating climate and stable water isotopes during the Last
591 Interglacial using a coupled climate-isotope model, Journal of Advances in Modeling Earth Systems,
592 9, 2027-2045, https://doi.org/10.1002/2017MS001056, 2017.

593 Guagnin, M., Jennings, R., Eager, H., Parton, A., Stimpson, C., Stepanek, C., Pfeiffer, M., Groucutt,
594 H. S., Drake, N. A., Alsharekh, A., and Petraglia, M. D.: Rock art imagery as a proxy for Holocene
595 environmental change: A view from Shuwaymis, NW Saudi Arabia, The Holocene, 26, 1822-1834,
596 https://doi.org/10.1177/0959683616645949, 2016.

597 Guo, C., Bentsen, M., Bethke, I., Ilicak, M., Tjiputra, J., Toniazzo, T., Schwinger, J., and Otterå, O. H.:
598 NCC NorESM1-F model output prepared for CMIP6 CMIP piControl, Version 20190920, Earth
599 System Grid Federation, https://doi.org/10.22033/ESGF/CMIP6.11595, 2019a.

600 Guo, C., Bentsen, M., Bethke, I., Ilicak, M., Tjiputra, J., Toniazzo, T., Schwinger, J., and Otterå, O. H.:
601 NCC NorESM1-F model output prepared for CMIP6 PMIP midHolocene, Version 20190920, Earth
602 System Grid Federation, https://doi.org/10.22033/ESGF/CMIP6.11591, 2019b.

603 Guo, C., Bentsen, M., Bethke, I., Ilicak, M., Tjiputra, J., Toniazzo, T., Schwinger, J., and Otterå, O. H.:
604 NCC NorESM1-F model output prepared for CMIP6 PMIP lig127k, Version 20190920, Earth System
605 Grid Federation, https://doi.org/10.22033/ESGF/CMIP6.11590, 2019c.

606 Hajima, T., Abe, M., Arakawa, O., Suzuki, T., Komuro, Y., Ogura, T., Ogochi, K., Watanabe, M.,
607 Yamamoto, A., Tatebe, H., Noguchi, M. A., Ohgaito, R., Ito, A., Yamazaki, D., Ito, A., Takata, K.,
608 Watanabe, S., Kawamiya, M., and Tachiiri, K.: MIROC MIROC-ES2L model output prepared for
609 CMIP6 CMIP piControl, Version 20190823, Earth System Grid Federation,
610 https://doi.org/10.22033/ESGF/CMIP6.5710, 2019.

611 Haywood, A. M., Hill, D. J., Dolan, A. M., Otto-Bliesner, B. L., Bragg, F., Chan, W. L., Chandler, M. A.,
612 Contoux, C., Dowsett, H. J., Jost, A., Kamae, Y., Lohmann, G., Lunt, D. J., Abe-Ouchi, A., Pickering,
613 S. J., Ramstein, G., Rosenbloom, N. A., Salzmann, U., Sohl, L., Stepanek, C., Ueda, H., Yan, Q., and
614 Zhang, Z.: Large-scale features of Pliocene climate: results from the Pliocene Model Intercomparison
615 Project, Clim. Past, 9, 191-209, https://doi.org/10.5194/cp-9-191-2013, 2013.

616 Haywood, A. M., Tindall, J. C., Dowsett, H. J., Dolan, A. M., Foley, K. M., Hunter, S. J., Hill, D. J.,
617 Chan, W. L., Abe-Ouchi, A., Stepanek, C., Lohmann, G., Chandan, D., Peltier, W. R., Tan, N.,
618 Contoux, C., Ramstein, G., Li, X., Zhang, Z., Guo, C., Nisancioglu, K. H., Zhang, Q., Li, Q., Kamae,
619 Y., Chandler, M. A., Sohl, L. E., Otto-Bliesner, B. L., Feng, R., Brady, E. C., von der Heydt, A. S.,
620 Baatsen, M. L. J., and Lunt, D. J.: The Pliocene Model Intercomparison Project Phase 2: large-scale
621 climate features and climate sensitivity, Clim. Past, 16, 2095-2123, https://doi.org/10.5194/cp-16-
622 2095-2020, 2020.

623 Heaton, T. J., Köhler, P., Butzin, M., Bard, E., Reimer, R. W., Austin, W. E. N., Bronk Ramsey, C.,
624 Grootes, P. M., Hughen, K. A., Kromer, B., Reimer, P. J., Adkins, J., Burke, A., Cook, M. S., Olsen, J.,
625 and Skinner, L. C.: Marine20—The Marine Radiocarbon Age Calibration Curve (0–55,000 cal BP),
626 Radiocarbon, 62, 779-820, https://doi.org/10.1017/RDC.2020.68, 2020.

627 Hopmans, E. C., Weijers, J. W. H., Schefuß, E., Herfort, L., Sinninghe Damsté, J. S., and Schouten,
628 S.: A novel proxy for terrestrial organic matter in sediments based on branched and isoprenoid
629 tetraether lipids, Earth and Planetary Science Letters, 224, 107-116,
630 https://doi.org/10.1016/j.epsl.2004.05.012, 2004.

631 Hossain, A., Knorr, G., Jokat, W., and Lohmann, G.: Opening of the Fram Strait led to the
632 establishment of a modern-like three-layer stratification in the Arctic Ocean during the Miocene,
633 arktos, 7, 1-12, https://doi.org/10.1007/s41063-020-00079-8, 2021.

634 Hossain, A., Knorr, G., Lohmann, G., Stärz, M., and Jokat, W.: Simulated Thermohaline Fingerprints
635 in Response to Different Greenland-Scotland Ridge and Fram Strait Subsidence Histories,
636 Paleoceanography and Paleoclimatology, 35, e2019PA003842,
637 https://doi.org/10.1029/2019PA003842, 2020.

638 Inglis, G. N., Farnsworth, A., Lunt, D., Foster, G. L., Hollis, C. J., Pagani, M., Jardine, P. E., Pearson,
639 P. N., Markwick, P., Galsworthy, A. M. J., Raynham, L., Taylor, K. W. R., and Pancost, R. D.: Descent
640 toward the Icehouse: Eocene sea surface cooling inferred from GDGT distributions,
641 Paleoceanography, 30, 1000-1020, https://doi.org/10.1002/2014PA002723, 2015.

642 Jennings, R. P., Singarayer, J., Stone, E. J., Krebs-Kanzow, U., Khon, V., Nisancioglu, K. H., Pfeiffer,
643 M., Zhang, X., Parker, A., Parton, A., Groucutt, H. S., White, T. S., Drake, N. A., and Petraglia, M. D.:
644 The greening of Arabia: Multiple opportunities for human occupation of the Arabian Peninsula during
645 the Late Pleistocene inferred from an ensemble of climate model simulations, Quaternary
646 International, 382, 181-199, https://doi.org/10.1016/j.quaint.2015.01.006, 2015.

647 Jungclaus, J., Mikolajewicz, U., Kapsch, M.-L., D'Agostino, R., Wieners, K.-H., Giorgetta, M., Reick,
648 C., Esch, M., Bittner, M., Legutke, S., Schupfner, M., Wachsmann, F., Gayler, V., Haak, H., de Vrese,
649 P., Raddatz, T., Mauritsen, T., von Storch, J.-S., Behrens, J., Brovkin, V., Claussen, M., Crueger, T.,
650 Fast, I., Fiedler, S., Hagemann, S., Hohenegger, C., Jahns, T., Kloster, S., Kinne, S., Lasslop, G.,
651 Kornblueh, L., Marotzke, J., Matei, D., Meraner, K., Modali, K., Müller, W., Nabel, J., Notz, D., Peters-
652 von Gehlen, K., Pincus, R., Pohlmann, H., Pongratz, J., Rast, S., Schmidt, H., Schnur, R.,
653 Schulzweida, U., Six, K., Stevens, B., Voigt, A., and Roeckner, E.: MPI-M MPI-ESM1.2-LR model
654 output prepared for CMIP6 PMIP midHolocene, Version 20190710, Earth System Grid Federation,
655 https://doi.org/10.22033/ESGF/CMIP6.6644, 2019a.

656 Jungclaus, J., Mikolajewicz, U., Kapsch, M.-L., D'Agostino, R., Wieners, K.-H., Giorgetta, M., Reick,
657 C., Esch, M., Bittner, M., Legutke, S., Schupfner, M., Wachsmann, F., Gayler, V., Haak, H., de Vrese,
658 P., Raddatz, T., Mauritsen, T., von Storch, J.-S., Behrens, J., Brovkin, V., Claussen, M., Crueger, T.,
659 Fast, I., Fiedler, S., Hagemann, S., Hohenegger, C., Jahns, T., Kloster, S., Kinne, S., Lasslop, G.,
660 Kornblueh, L., Marotzke, J., Matei, D., Meraner, K., Modali, K., Müller, W., Nabel, J., Notz, D., Peters-
661 von Gehlen, K., Pincus, R., Pohlmann, H., Pongratz, J., Rast, S., Schmidt, H., Schnur, R.,
662 Schulzweida, U., Six, K., Stevens, B., Voigt, A., and Roeckner, E.: MPI-M MPI-ESM1.2-LR model
663 output prepared for CMIP6 PMIP lgm, Version 20190710, Earth System Grid Federation,
664 https://doi.org/10.22033/ESGF/CMIP6.6642, 2019b.

665 Kaboth-Bahr, S., Bahr, A., Stepanek, C., Catunda, M. C. A., Karas, C., Ziegler, M., García-Gallardo,
666 Á., and Grunert, P.: Mediterranean heat injection to the North Atlantic delayed the intensification of
667 Northern Hemisphere glaciations, Communications Earth & Environment, 2, 158,
668 https://doi.org/10.1038/s43247-021-00232-5, 2021.

669 Kageyama, M., Albani, S., Braconnot, P., Harrison, S. P., Hopcroft, P. O., Ivanovic, R. F., Lambert, F.,
670 Marti, O., Peltier, W. R., Peterschmitt, J. Y., Roche, D. M., Tarasov, L., Zhang, X., Brady, E. C.,
671 Haywood, A. M., LeGrande, A. N., Lunt, D. J., Mahowald, N. M., Mikolajewicz, U., Nisancioglu, K. H.,
672 Otto-Bliesner, B. L., Renssen, H., Tomas, R. A., Zhang, Q., Abe-Ouchi, A., Bartlein, P. J., Cao, J., Li,
673 Q., Lohmann, G., Ohgaito, R., Shi, X., Volodin, E., Yoshida, K., Zhang, X., and Zheng, W.: The

PMIP4 contribution to CMIP6 – Part 4: Scientific objectives and experimental design of the PMIP4-CMIP6 Last Glacial Maximum experiments and PMIP4 sensitivity experiments, Geosci. Model Dev., 10, 4035-4055, https://doi.org/10.5194/gmd-10-4035-2017, 2017.

Kim, J.-H., Schouten, S., Rodrigo-Gámiz, M., Rampen, S., Marino, G., Huguet, C., Helmke, P., Buscail, R., Hopmans, E. C., Pross, J., Sangiorgi, F., Middelburg, J. B. M., and Sinninghe Damsté, J. S.: Influence of deep-water derived isoprenoid tetraether lipids on the TEX86H paleothermometer in the Mediterranean Sea, Geochimica et Cosmochimica Acta, 150, 125-141, https://doi.org/10.1016/j.gca.2014.11.017, 2015.

Klages, J. P., Salzmann, U., Bickert, T., Hillenbrand, C.-D., Gohl, K., Kuhn, G., Bohaty, S. M., Titschack, J., Müller, J., Frederichs, T., Bauersachs, T., Ehrmann, W., van de Flierdt, T., Pereira, P. S., Larter, R. D., Lohmann, G., Niezgodzki, I., Uenzelmann-Neben, G., Zundel, M., Spiegel, C., Mark, C., Chew, D., Francis, J. E., Nehrke, G., Schwarz, F., Smith, J. A., Freudenthal, T., Esper, O., Pälike, H., Ronge, T. A., Dziadek, R., Afanasyeva, V., Arndt, J. E., Ebermann, B., Gebhardt, C., Hochmuth, K., Küssner, K., Najman, Y., Riefstahl, F., Scheinert, M., and the Science Team of Expedition, P. S.: Temperate rainforests near the South Pole during peak Cretaceous warmth, Nature, 580, 81-86, https://doi.org/10.1038/s41586-020-2148-5, 2020.

Knorr, G. and Lohmann, G.: Climate warming during Antarctic ice sheet expansion at the Middle Miocene transition, Nature Geoscience, 7, 376-381, https://doi.org/10.1038/ngeo2119, 2014.

Knorr, G., Butzin, M., Micheels, A., and Lohmann, G.: A warm Miocene climate at low atmospheric CO2 levels, Geophysical Research Letters, 38, https://doi.org/10.1029/2011GL048873, 2011.

Knorr, G., Barker, S., Zhang, X., Lohmann, G., Gong, X., Gierz, P., Stepanek, C., and Stap, L. B.: A salty deep ocean as a prerequisite for glacial termination, Nature Geoscience, 14, 930-936, https://doi.org/10.1038/s41561-021-00857-3, 2021.

Kotov, S. and Pälike, H.: QAnalySeries-a cross-platform time series tuning and analysis tool, AGU Fall Meeting Abstracts, PP53D-1230,

Langner, M. and Mulitza, S.: Technical note: PaleoDataView – a software toolbox for the collection, homogenization and visualization of marine proxy data, Clim. Past, 15, 2067-2072, https://doi.org/10.5194/cp-15-2067-2019, 2019.

Li, L.: CAS FGOALS-g3 model output prepared for CMIP6 CMIP piControl, Version 20191126, Earth System Grid Federation, https://doi.org/10.22033/ESGF/CMIP6.3448, 2019.

Lisiecki, L. E. and Raymo, M. E.: A Pliocene-Pleistocene stack of 57 globally distributed benthic δ18O records, Paleoceanography, 20, https://doi.org/10.1029/2004PA001071, 2005.

Lohmann, G., Knorr, G., Hossain, A., and Stepanek, C.: Effects of CO2 and Ocean Mixing on Miocene and Pliocene Temperature Gradients, Paleoceanography and Paleoclimatology, 37, e2020PA003953, https://doi.org/10.1029/2020PA003953, 2022.

Lunt, D. J., Abe-Ouchi, A., Bakker, P., Berger, A., Braconnot, P., Charbit, S., Fischer, N., Herold, N., Jungclaus, J. H., Khon, V. C., Krebs-Kanzow, U., Langebroek, P. M., Lohmann, G., Nisancioglu, K. H., Otto-Bliesner, B. L., Park, W., Pfeiffer, M., Phipps, S. J., Prange, M., Rachmayani, R., Renssen, H., Rosenbloom, N., Schneider, B., Stone, E. J., Takahashi, K., Wei, W., Yin, Q., and Zhang, Z. S.: A multi-model assessment of last interglacial temperatures, Clim. Past, 9, 699-717, https://doi.org/10.5194/cp-9-699-2013, 2013.

Lunt, D. J., Bragg, F., Chan, W. L., Hutchinson, D. K., Ladant, J. B., Morozova, P., Niezgodzki, I., Steinig, S., Zhang, Z., Zhu, J., Abe-Ouchi, A., Anagnostou, E., de Boer, A. M., Coxall, H. K., Donnadieu, Y., Foster, G., Inglis, G. N., Knorr, G., Langebroek, P. M., Lear, C. H., Lohmann, G., Poulsen, C. J., Sepulchre, P., Tierney, J. E., Valdes, P. J., Volodin, E. M., Dunkley Jones, T., Hollis, C. J., Huber, M., and Otto-Bliesner, B. L.: DeepMIP: model intercomparison of early Eocene climatic optimum (EECO) large-scale climate features and comparison with proxy data, Clim. Past, 17, 203-227, https://doi.org/10.5194/cp-17-203-2021, 2021.

Luo, F., Ying, J., Liu, T., and Chen, D.: Origins of Southern Ocean warm sea surface temperature bias in CMIP6 models, npj Climate and Atmospheric Science, 6, 127, https://doi.org/10.1038/s41612-023-00456-6, 2023.

Mollenhauer, G., Grotheer, H., Gentz, T., Bonk, E., and Hefter, J.: Standard operation procedures and performance of the MICADAS radiocarbon laboratory at Alfred Wegener Institute (AWI), Germany, Nuclear Instruments and Methods in Physics Research Section B: Beam Interactions with Materials and Atoms, 496, 45-51, https://doi.org/10.1016/j.nimb.2021.03.016, 2021.

NASA Goddard Institute for Space Studies: NASA-GISS GISS-E2.1G model output prepared for CMIP6 CMIP piControl, Version 20180824, Earth System Grid Federation, https://doi.org/10.22033/ESGF/CMIP6.7380, 2018.

NASA Goddard Institute for Space Studies: NASA-GISS GISS-E2.1G model output prepared for CMIP6 PMIP midHolocene, Version 20190916, Earth System Grid Federation, https://doi.org/10.22033/ESGF/CMIP6.7225, 2019.

Niezgodzki, I., Tyszka, J., Knorr, G., and Lohmann, G.: Was the Arctic Ocean ice free during the latest Cretaceous? The role of CO2 and gateway configurations, Global and Planetary Change, 177, 201-212, https://doi.org/10.1016/j.gloplacha.2019.03.011, 2019.

O'ishi, R., Abe-Ouchi, A., Ohgaito, R., Abe, M., Arakawa, O., Ogochi, K., Hajima, T., Watanabe, M., Yamamoto, A., Tatebe, H., Noguchi, M. A., Ito, A., Yamazaki, D., Ito, A., Takata, K., Watanabe, S., Kawamiya, M., and Tachiiri, K.: MIROC MIROC-ES2L model output prepared for CMIP6 PMIP lig127k, Version 20191118, Earth System Grid Federation, https://doi.org/10.22033/ESGF/CMIP6.5645, 2019.

Ohgaito, R., Abe-Ouchi, A., Abe, M., Arakawa, O., Ogochi, K., Hajima, T., Watanabe, M., Yamamoto, A., Tatebe, H., Noguchi, M. A., Ito, A., Yamazaki, D., Ito, A., Takata, K., Watanabe, S., Kawamiya, M., and Tachiiri, K.: MIROC MIROC-ES2L model output prepared for CMIP6 PMIP midHolocene, Version 20191002, Earth System Grid Federation, https://doi.org/10.22033/ESGF/CMIP6.5646., 2019a.

Ohgaito, R., Abe-Ouchi, A., Abe, M., Arakawa, O., Ogochi, K., Hajima, T., Watanabe, M., Yamamoto, A., Tatebe, H., Noguchi, M. A., Ito, A., Yamazaki, D., Ito, A., Takata, K., Watanabe, S., Kawamiya, M., and Tachiiri, K.: MIROC MIROC-ES2L model output prepared for CMIP6 PMIP lgm, Version 20191002, Earth System Grid Federation, https://doi.org/10.22033/ESGF/CMIP6.5644, 2019b.

Otto-Bliesner, B. L., Braconnot, P., Harrison, S. P., Lunt, D. J., Abe-Ouchi, A., Albani, S., Bartlein, P. J., Capron, E., Carlson, A. E., Dutton, A., Fischer, H., Goelzer, H., Govin, A., Haywood, A., Joos, F., LeGrande, A. N., Lipscomb, W. H., Lohmann, G., Mahowald, N., Nehrbass-Ahles, C., Pausata, F. S. R., Peterschmitt, J. Y., Phipps, S. J., Renssen, H., and Zhang, Q.: The PMIP4 contribution to CMIP6 – Part 2: Two interglacials, scientific objective and experimental design for Holocene and Last Interglacial simulations, Geosci. Model Dev., 10, 3979-4003, https://doi.org/10.5194/gmd-10-3979-2017, 2017.

Park, E.: Variations in GDGT flux and TEX86 thermometry in three distinct oceanic regimes of the Atlantic Ocean: a sediment trap study, University of Bremen, 2019.

Pfeiffer, M. and Lohmann, G.: Greenland Ice Sheet influence on Last Interglacial climate: global sensitivity studies performed with an atmosphere–ocean general circulation model, Clim. Past, 12, 1313-1338, https://doi.org/10.5194/cp-12-1313-2016, 2016.

Ridley, J., Menary, M., Kuhlbrodt, T., Andrews, M., and Andrews, T.: MOHC HadGEM3-GC31-LL model output prepared for CMIP6 CMIP piControl. Version 20211103, Earth System Grid Federation, https://doi.org/10.22033/ESGF/CMIP6.6294, 2018.

Schouten, S., Hopmans, E. C., and Damsté, J. S. S.: The organic geochemistry of glycerol dialkyl glycerol tetraether lipids: A review, Organic geochemistry, 54, 19-61, http://dx.doi.org/10.1016/j.orggeochem.2012.09.006, 2013.

769 Seland, Ø., Bentsen, M., Oliviè, D. J. L., Toniazzo, T., Gjermundsen, A., Graff, L. S., Debernard, J. B.,
770 Gupta, A. K., He, Y., Kirkevåg, A., Schwinger, J., Tjiputra, J., Aas, K. S., Bethke, I., Fan, Y.,
771 Griesfeller, J., Grini, A., Guo, C., Ilicak, M., Karset, I. H. H., Landgren, O. A., Liakka, J., Moseid, K. O.,
772 Nummelin, A., Spensberger, C., Tang, H., Zhang, Z., Heinze, C., Iversen, T., and Schulz, M.: NCC
773 NorESM2-LM model output prepared for CMIP6 CMIP piControl, Version 20210118,, Earth System
774 Grid Federation, https://doi.org/10.22033/ESGF/CMIP6.8217, 2019.

775 Shi, X., Yang, H., Danek, C., and Lohmann, G.: AWI AWI-ESM1.1LR model output prepared for
776 CMIP6 PMIP lgm, Version 20200212, Earth System Grid Federation,
777 https://doi.org/10.22033/ESGF/CMIP6.9330, 2020a.

778 Shi, X., Yang, H., Danek, C., and Lohmann, G.: AWI AWI-ESM1.1LR model output prepared for
779 CMIP6 PMIP lig127k, Version 20200212, Earth System Grid Federation,
780 https://doi.org/10.22033/ESGF/CMIP6.9331, 2020b.

781 Stein, R., Fahl, K., Gierz, P., Niessen, F., and Lohmann, G.: Arctic Ocean sea ice cover during the
782 penultimate glacial and the last interglacial, Nature Communications, 8, 373,
783 https://doi.org/10.1038/s41467-017-00552-1, 2017.

784 Stein, R., Fahl, K., Schreck, M., Knorr, G., Niessen, F., Forwick, M., Gebhardt, C., Jensen, L.,
785 Kaminski, M., Kopf, A., Matthiessen, J., Jokat, W., and Lohmann, G.: Evidence for ice-free summers
786 in the late Miocene central Arctic Ocean, Nature Communications, 7, 11148,
787 https://doi.org/10.1038/ncomms11148, 2016.

788 Stepanek, C. and Lohmann, G.: Modelling mid-Pliocene climate with COSMOS, Geosci. Model Dev.,
789 5, 1221-1243, https://doi.org/10.5194/gmd-5-1221-2012, 2012.

790 Stepanek, C., Samakinwa, E., Knorr, G., and Lohmann, G.: Contribution of the coupled atmosphere–
791 ocean–sea ice–vegetation model COSMOS to the PlioMIP2, Clim. Past, 16, 2275-2323,
792 https://doi.org/10.5194/cp-16-2275-2020, 2020.

793 Taylor, K. W. R., Huber, M., Hollis, C. J., Hernandez-Sanchez, M. T., and Pancost, R. D.: Re-
794 evaluating modern and Palaeogene GDGT distributions: Implications for SST reconstructions, Global
795 and Planetary Change, 108, 158-174, https://doi.org/10.1016/j.gloplacha.2013.06.011, 2013.

796 Varma, V., Prange, M., Merkel, U., Kleinen, T., Lohmann, G., Pfeiffer, M., Renssen, H., Wagner, A.,
797 Wagner, S., and Schulz, M.: Holocene evolution of the Southern Hemisphere westerly winds in
798 transient simulations with global climate models, Clim. Past, 8, 391-402, https://doi.org/10.5194/cp-8-
799 391-2012, 2012.

800 Voldoire, A.: CMIP6 simulations of the CNRM-CERFACS based on CNRM-CM6-1 model for CMIP
801 experiment piControl, Version 20180814, Earth System Grid Federation,
802 https://doi.org/10.22033/ESGF/CMIP6.4163, 2018.

803 Voldoire, A.: CNRM-CERFACS CNRM-CM6-1 model output prepared for CMIP6 PMIP lig127k,
804 Version 20200212, Earth System Grid Federation, https://doi.org/10.22033/ESGF/CMIP6.4118, 2020.

805 Volodin, E., Mortikov, E., Gritsun, A., Lykossov, V., Galin, V., Diansky, N., Gusev, A., Kostrykin, S.,
806 Iakovlev, N., Shestakova, A., and Emelina, S.: INM INM-CM4-8 model output prepared for CMIP6
807 CMIP piControl. Version 20190605, Earth System Grid Federation,
808 https://doi.org/10.22033/ESGF/CMIP6.5080, 2019a.

809 Volodin, E., Mortikov, E., Gritsun, A., Lykossov, V., Galin, V., Diansky, N., Gusev, A., Kostrykin, S.,
810 Iakovlev, N., Shestakova, A., and Emelina, S.: INM INM-CM4-8 model output prepared for CMIP6
811 PMIP midHolocene. Version 20190802, Earth System Grid Federation,
812 https://doi.org/10.22033/ESGF/CMIP6.5077, 2019b.

813 Volodin, E., Mortikov, E., Gritsun, A., Lykossov, V., Galin, V., Diansky, N., Gusev, A., Kostrykin, S.,
814 Iakovlev, N., Shestakova, A., and Emelina, S.: INM INM-CM4-8 model output prepared for CMIP6

PMIP lgm, Version 20201112, Earth System Grid Federation, https://doi.org/10.22033/ESGF/CMIP6.5075, 2019c.

Weber, M. E., Bailey, I., Hemming, S. R., Martos, Y. M., Reilly, B. T., Ronge, T. A., Brachfeld, S., Williams, T., Raymo, M., Belt, S. T., Smik, L., Vogel, H., Peck, V. L., Armbrecht, L., Cage, A., Cardillo, F. G., Du, Z., Fauth, G., Fogwill, C. J., Garcia, M., Garnsworthy, M., Glüder, A., Guitard, M., Gutjahr, M., Hernández-Almeida, I., Hoem, F. S., Hwang, J.-H., Iizuka, M., Kato, Y., Kenlee, B., Oconnell, S., Pérez, L. F., Seki, O., Stevens, L., Tauxe, L., Tripathi, S., Warnock, J., and Zheng, X.: Antiphased dust deposition and productivity in the Antarctic Zone over 1.5 million years, Nature Communications, 13, 2044, https://doi.org/10.1038/s41467-022-29642-5, 2022.

Wei, W. and Lohmann, G.: Simulated Atlantic Multidecadal Oscillation during the Holocene, Journal of Climate, 25, 6989-7002, https://doi.org/10.1175/JCLI-D-11-00667.1, 2012.

Weijers, J. W. H., Schouten, S., Spaargaren, O. C., and Sinninghe Damsté, J. S.: Occurrence and distribution of tetraether membrane lipids in soils: Implications for the use of the TEX86 proxy and the BIT index, Organic Geochemistry, 37, 1680-1693, https://doi.org/10.1016/j.orggeochem.2006.07.018, 2006.

Wieners, K.-H., Giorgetta, M., Jungclaus, J., Reick, C., Esch, M., Bittner, M., Legutke, S., Schupfner, M., Wachsmann, F., Gayler, V., Haak, H., de Vrese, P., Raddatz, T., Mauritsen, T., von Storch, J.-S., Behrens, J., Brovkin, V., Claussen, M., Crueger, T., Fast, I., Fiedler, S., Hagemann, S., Hohenegger, C., Jahns, T., Kloster, S., Kinne, S., Lasslop, G., Kornblueh, L., Marotzke, J., Matei, D., Meraner, K., Mikolajewicz, U., Modali, K., Müller, W., Nabel, J., Notz, D., Peters-von Gehlen, K., Pincus, R., Pohlmann, H., Pongratz, J., Rast, S., Schmidt, H., Schnur, R., Schulzweida, U., Six, K., Stevens, B., Voigt, A., and Roeckner, E.: MPI-M MPI-ESM1.2-LR model output prepared for CMIP6 CMIP piControl, Version 20190710, Earth System Grid Federation, https://doi.org/10.22033/ESGF/CMIP6.6675, 2019.

Williams, C., Lunt, D., Singarayer, J., and Guarino, M. V.: NERC HadGEM3-GC31-LL model output prepared for CMIP6 PMIP midHolocene, Version 20210111, Earth System Grid Federation, https://doi.org/10.22033/ESGF/CMIP6.12129, 2021a.

Williams, C., Lunt, D., Singarayer, J., and Guarino, M. V.: NERC HadGEM3-GC31-LL model output prepared for CMIP6 PMIP lig127k, Version 20210114, Earth System Grid Federation, https://doi.org/10.22033/ESGF/CMIP6.12128, 2021b.

Yeung, N., Menviel, L., Meissner, K., Ziehn, T., Chamberlain, M., Mackallah, C., Druken, K., and Ridzwan, S., M.: CSIRO ACCESS-ESM1.5 model output prepared for CMIP6 PMIP lig127k, Version 20200817, Earth System Grid Federation, https://doi.org/10.22033/ESGF/CMIP6.13703, 2019.

Yu, Y.: CAS FGOALS-f3-L model output prepared for CMIP6 CMIP piControl, Version 20191028, Earth System Grid Federation, https://doi.org/10.22033/ESGF/CMIP6.3447, 2019.

Yukimoto, S., Koshiro, T., Kawai, H., Oshima, N., Yoshida, K., Urakawa, S., Tsujino, H., Deushi, M., Tanaka, T., Hosaka, M., Yoshimura, H., Shindo, E., Mizuta, R., Ishii, M., Obata, A., and Adachi, Y.: MRI MRI-ESM2.0 model output prepared for CMIP6 CMIP piControl, Version 20190904, Earth System Grid Federation, https://doi.org/10.22033/ESGF/CMIP6.6900, 2019a.

Yukimoto, S., Koshiro, T., Kawai, H., Oshima, N., Yoshida, K., Urakawa, S., Tsujino, H., Deushi, M., Tanaka, T., Hosaka, M., Yoshimura, H., Shindo, E., Mizuta, R., Ishii, M., Obata, A., and Adachi, Y.: MRI MRI-ESM2.0 model output prepared for CMIP6 PMIP midHolocene, Version 20190919, Earth System Grid Federation, https://doi.org/10.22033/ESGF/CMIP6.6860, 2019b.

Zhang, X., Lohmann, G., Knorr, G., and Xu, X.: Different ocean states and transient characteristics in Last Glacial Maximum simulations and implications for deglaciation, Clim. Past, 9, 2319-2333, https://doi.org/10.5194/cp-9-2319-2013, 2013.

Zhang, X., Barker, S., Knorr, G., Lohmann, G., Drysdale, R., Sun, Y., Hodell, D., and Chen, F.: Direct astronomical influence on abrupt climate variability, Nature Geoscience, 14, 819-826, https://doi.org/10.1038/s41561-021-00846-6, 2021.

Zhang, Y. G., Pagani, M., and Wang, Z.: Ring Index: A new strategy to evaluate the integrity of TEX86 paleothermometry, Paleoceanography, 31, 220-232, https://doi.org/10.1002/2015PA002848, 2016.

Zhang, Z., Bentsen, M., Oliviè, D. J. L., Seland, Ø., Toniazzo, T., Gjermundsen, A., Graff, L. S., Debernard, J. B., Gupta, A. K., He, Y., Kirkevåg, A., Schwinger, J., Tjiputra, J., Aas, K. S., Bethke, I., Fan, Y., Griesfeller, J., Grini, A., Guo, C., Ilicak, M., Karset, I. H. H., Landgren, O. A., Liakka, J., Moseid, K. O., Nummelin, A., Spensberger, C., Tang, H., Heinze, C., Iversen, T., and Schulz, M.: NCC NorESM2-LM model output prepared for CMIP6 PMIP midHolocene, Version 20191108, Earth System Grid Federation, https://doi.org/10.22033/ESGF/CMIP6.8079, 2019a.

Zhang, Z., Bentsen, M., Oliviè, D. J. L., Seland, Ø., Toniazzo, T., Gjermundsen, A., Graff, L. S., Debernard, J. B., Gupta, A. K., He, Y., Kirkevåg, A., Schwinger, J., Tjiputra, J., Aas, K. S., Bethke, I., Fan, Y., Griesfeller, J., Grini, A., Guo, C., Ilicak, M., Karset, I. H. H., Landgren, O. A., Liakka, J., Moseid, K. O., Nummelin, A., Spensberger, C., Tang, H., Heinze, C., Iversen, T., and Schulz, M.: NCC NorESM2-LM model output prepared for CMIP6 PMIP lig127k, Version 20191108, Earth System Grid Federation, https://doi.org/10.22033/ESGF/CMIP6.8078, 2019b.

Zheng, W. and Dong, L.: CAS FGOALS-g3 model output prepared for CMIP6 PMIP midHolocene, Version 20191026, Earth System Grid Federation, https://doi.org/10.22033/ESGF/CMIP6.3409, 2019a.

Zheng, W. and Dong, L.: CAS FGOALS-g3 model output prepared for CMIP6 PMIP lig127k, Version 20191030, Earth System Grid Federation, https://doi.org/10.22033/ESGF/CMIP6.3407, 2019b.

Zheng, W. and He, B.: CAS FGOALS-f3-L model output prepared for CMIP6 PMIP midHolocene, Version 20191101, Earth System Grid Federation, https://doi.org/10.22033/ESGF/CMIP6.12014, 2019a.

Zheng, W. and He, B.: CAS FGOALS-f3-L model output prepared for CMIP6 PMIP lig127k, Version 20191101, Earth System Grid Federation, https://doi.org/10.22033/ESGF/CMIP6.12013, 2019b.

Ziehn, T., Chamberlain, M., Lenton, A., Law, R., Bodman, R., Dix, M., Wang, Y., Dobrohotoff, P., Srbinovsky, J., Stevens, L., Vohralik, P., Mackallah, C., Sullivan, A., O'Farrell, S., and Druken, K.: CSIRO ACCESS-ESM1.5 model output prepared for CMIP6 CMIP piControl, Version 20210316, Earth System Grid Federation, https://doi.org/10.22033/ESGF/CMIP6.4312, 2019.

Zielinski, U., Bianchi, C., Gersonde, R., and Kunz-Pirrung, M.: Last occurrence datums of the diatoms Rouxia leventerae and Rouxia constricta: indicators for marine isotope stages 6 and 8 in Southern Ocean sediments, Marine Micropaleontology, 46, 127-137, https://doi.org/10.1016/S0377-8398(02)00042-7, 2002.